Investigation of novel Cr^{6+}-free anodising pre-treatments for enhanced corrosion protection of aluminium alloy 2024-T3

MSc thesis

S. L. Nierijnck

TU Delft

Investigation of novel Cr^{6+}-free anodising pre-treatments for enhanced corrosion protection of aluminium alloy 2024-T3

MSc thesis

in partial fulfilment of the requirements for the degree of

Master of Science

in Materials Science and Engineering

at Delft University of Technology
to be defended publicly on 28 February 2020, at 13:00

By

S. L. Nierijnck

Bachelor of Engineering in Mechanical Engineering
HZ University of Applied Sciences, Vlissingen, The Netherlands
Born on 1 March 1991 in Vlissingen, The Netherlands

Composition of thesis committee

Prof. dr. ir. J.M.C. Mol	Chairman	Delft University of Technology Department of Materials Science and Engineering Corrosion Technology and Electrochemistry section
Dr. J.G. Buijnsters	Member	Delft University of Technology Department of Precision and Microsystems Engineering Micro and Nano Engineering section
Dr. U. Tiringer	Member	Delft University of Technology Department of Materials Science and Engineering Corrosion Technology and Electrochemistry section

Additional information

An electronic version of this thesis is available at http://repository.tudelft.nl/.

Acknowledgements

Turning a graduation project into a successful one is not an easy job and therefore proper supervision and guidance are very important. During my research project I got help from many people, too many to thank individually in this section of my thesis. A few people however I should mention since they made quite a significant contribution to this work.

First and foremost I would like to thank my supervisors Arjan Mol and Marta Michalska-Domańska for their supervision and for offering me the opportunity to do my thesis work within the Corrosion Technology and Electrochemistry group at TU Delft. Secondly I would like to thank Joost van Dam and Urša Tiringer for the countless amount of hours they spent helping me out on both a practical and a theoretical level during Marta's maternity leave and end of contract period. I also would like to thank Mats Meeusen for his efforts, especially in the beginning of this project both in and outside the lab. Due to the experimental character of this project I needed to spent a lot of time in the lab and this would not been possible without the help of our lab technician Agnieszka Kooijman-Banaszak. Her help on the practical side of things and all the nice social conversations made it a very enjoyable time. For all the tips, tricks and advise about the anodising process in general and the nice social conversations I would like to thank Shoshan Abrahami. Besides I would like to thank everyone whom I spent countless amounts of coffeetimes, lunch hours and social moments with. This really made a significant contribution to making my graduation period a very enjoyable period and it helped keeping my mind at bay during the more challenging moments.

Last but definitely not least I would like to thank my girlfriend and my family for always being there for me and always offering me a listening ear in both difficult and happy times.

<div align="right">

Sven Nierijnck
Delft, February 2020

</div>

Abstract

Hexavalent chromium has been the industry standard for corrosion protection for many years. Its unsurpassed active corrosion inhibiting capabilities, its incredible versatility and its economic benefits made it a popular all-rounder. Nowadays the widely known toxic and carcinogenic nature have restricted its use within the European Union. More and more research in the field of corrosion science has been focussing on finding safer alternatives, since hexavalent chromium was officially added the US annual report on carcinogens in the 1980s. Before it was used in almost every step of corrosion protective schemes consisting of a pre-treatment, a primer and a topcoat.

In this work a novel approach to two industrial anodising pre-treatments (sulfuric acid anodising and tartaric sulfuric acid anodising) was investigated in order to improve the corrosion performance of the corrosion sensitive aluminium alloy 2024-T3. Both are currently used as alternatives to the historically often applied chromic acid anodising procedure, which contains hexavalent chromium compounds. In this work the effect of the anodising electrolyte viscosity, the anodising interelectrode distance and the addition of ceric sulphate to the anodising bath were investigated. Different fractions of ethylene glycol were used to vary the electrolyte viscosity. All anodising procedures used a fixed anodising voltage, temperature, acid concentration and agitation speed. These parameters were not changed. All samples were cleaned before anodising. In order to assess the corrosion performance linear sweep voltammetry, electrochemical impedance spectroscopy and immersion tests were deployed. Furthermore scanning electron microscopy with energy dispersive X-ray spectroscopy was used to evaluate the chemical composition of the anodised substrates.

It was found that an increase of the electrolyte viscosity results in a decrease of the anodising current density, which was related to a decrease in the overall thickness of the oxide layer created by the anodising process. The addition of 25 vol% ethylene glycol did not show any significant changes in corrosion performance although some indications of a slight improvement were found. Slightly smaller pores and a tighter barrier layer were proposed to be a possible explanation. A fraction of 75 vol% on the other hand dramatically deteriorated the corrosion performance, due to much slower oxide growth kinetics resulting in a much thinner oxide. The addition of ceric sulphate did not lead to any significant improvements in the corrosion performance for any of the tested procedures with one exception. The tartaric acid based procedure without ethylene glycol addition did show a significant improvement. Negatively charged complexes of cerium and tartaric acid compounds, which are supposed to be drawn towards the substrate during anodising, were proposed to be a possible explanation. The interelectrode distance did not show any significant differences except for the tartaric acid based procedure with ceric sulphate but without ethylene glycol addition. A higher electric field strength as a results of the smaller interelectrode distance was held responsible. The electric field strength should directly affect the amount of cerium complexes attracted towards the substrate, increasing the chance of cerium ending up as residues in the pores of the anodic oxide layer.

Keywords: Anodising; Corrosion; Aluminium; AA2024-T3; Chromium-6; Chromic acid; Sulfuric acid; Tartaric acid; Ethylene glycol; Interelectrode distance; Inhibitor; Cerium; Linear sweep voltammetry; Electrochemical impedance spectroscopy, Scanning electron microscopy, Energy dispersive X-ray spectroscopy, Immersion tests

Contents

1. Introduction

Aluminium, a lightweight post-transition metal, is the third most abundant element found in the earth's crust right after oxygen and silicon. [1] Its low density and its high strength to weight ratio for some of its alloys, make it a very attractive material for the aerospace sector. [2] Moreover, aluminium tends to form a thin uniform layer of aluminium oxide on its outer surface, a process called passivation, protecting itself against corrosion. As long as the environmental conditions are not too acidic or too alkaline aluminium protects itself rather well with this so called passive layer of alumina. Despite all benefits pure aluminium has one major drawback, which is the fact that it is very soft and lacks strength to be used in useful structural applications. Therefore a lot of aluminium alloys have been developed over the years in order to improve the mechanical properties of aluminium. Adding alloying elements however, is typically not beneficial in terms of corrosion protection. [2,3] This work investigates some novel approaches to hexavalent chromium free anodising processes in order to improve the corrosion performance of aluminium alloy 2024-T3, i.e. AA2024-T3.

1.1. Hexavalent chromium

Unlike iron, aluminium does not have any allotropes. This means that in solid state it always has a face-centred cubic crystal structure and therefore it is intrinsically impossible to benefit from allotropic phase transformations when designing novel alloys with improved (mechanical) properties. [4] Aluminium alloys rely on precipitation reactions with their alloying elements, which as a result introduce localised differences in electrochemical potential. This increases their susceptibility to localised corrosion. [3,4] In order to protect these alloys against corrosion many different strategies have been investigated over the years. In industry multi-layered coating systems are deployed against corrosion which consisting of a cleaning routine, a pre-treatment, a primer and a topcoat. [5,6] For many years hexavalent chromium (Cr^{6+}) compounds have been used in basically every step of the coating application process, from cleaning and pre-treating to loading the primer with Cr^{6+} containing pigments. Its unsurpassed active corrosion inhibiting capabilities in case of coating damage, its incredible versatility in both coating and material compatibility and its economic benefits made it a really popular all-rounder in corrosion protection. [7] Ever since the 1920s there have been reports on an increase of the incidence of different forms of cancer amongst industrial workers working with chromium compounds in general. [8] However it was not until the 1980s that the toxicity and carcinogenicity of the specific Cr^{6+} compounds was added to the US annual report on carcinogens by the Department of Health and Human Service. [8] From the 1980s onwards more and more research has been focussed on finding less toxic alternatives in all kinds of fields. [8] Since September 2017 the use of Cr^{6+} compounds is restricted within the European Union which means that industrial users are now forced to find substitutes or apply for authorization to continue using it. [8,9]

1.2. Anodising

Anodising is an electrochemical pre-treatment carried out right after a cleaning procedure. Typically pre-treatments are used to improve a materials corrosion performance and its adherent

properties towards either a coating or an adhesive applied right after. [7] Anodising capitalises a materials' natural tendency to form a protective layer. During the anodising process the material is immersed in generally an acidic electrolyte and anodically polarised. This forces the electrochemical reaction which forms an artificial but stable oxide layer, also called anodic oxide. Anodising in acidic electrolytes creates an anodic oxide with a distinct duplex structure consisting of a dense barrier layer and a porous layer consisting of vertical standing pores, see Figure 1.1. The morphology (e.g. the thickness of the barrier layer and diameter of the pores) is affected by the anodising parameters, i.e. anodising voltage, electrolyte, temperature etc. [10,11]
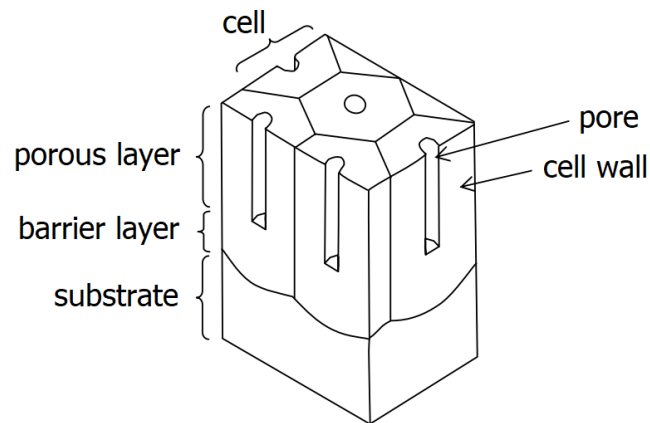
Figure 1.1: Typical morphology of anodic aluminium oxide. [11]

1.3. Origin of this project

Research in the field of nanomanufacturing by Chen et al. [12] in 2008 has pointed out the effects of the anodising electrolyte viscosity on some of the morphological parameters of highly ordered anodic aluminium oxide formed on high purity aluminium in phosphoric acid. The viscosity of the electrolyte was modulated by using different concentrations of polyethylene glycol (PEG). It was shown that a higher electrolyte viscosity leads to a decreased thickness of the anodic oxide, a decreased pore diameter and an increased complex impedance. The latter was explained as the result of the decrease in pore diameter and the probable formation of a tighter barrier layer (i.e. less defects and closer packing) since its thickness remained constant. [12] An increased interpore distance was also assumed to be a third reason due to the lower relative permittivity (i.e. dielectric constant) of PEG compared to water [12,13]. This gives rise to an increase of the electric field strength involved resulting in a larger interpore distance. [12] As a results less pores per unit area will develop. Later, in 2014, research by Stępniowski et al. [14] showed similar correlations between the morphological parameters of anodic aluminium oxides formed on high purity aluminium in oxalic acid with different concentrations of glycerol. The assumption by Chen et al. [12] on the increase of the interpore distance as a results of an increase of the concentration of PEG was confirmed and quantified in the work of Stępniowski et al. [14] using different concentration of glycerol. Furthermore, research by Michalska-Domańska et al. [15] showed, in 2018, that the interelectrode distance during the anodising process did not have any significant effect on the typical morphological parameters of anodic aluminium oxide formed on high purity aluminium in oxalic acid. However, increasing the interelectrode distance did either negatively or positively alter the regularity ratio of the pore arrangement depending on the anodising temperature and voltage. [15]

2

To date there is no knowledge on the effect of the anodising electrolyte viscosity or the interelectrode distance on the corrosion performance of aluminium alloys. Only one work, on titanium, by Dumitriu et al. [16] is worth mentioning. This work describes a positive change in corrosion behaviour of anodised titanium exposed to a Hank solution, when anodised in a more viscous electrolyte.

1.4. Aim of the current work

The aim of this work is to provide a new insight into the effect of the anodising electrolyte viscosity and the interelectrode distance on the corrosion performance of AA2024-T3. Sulfuric acid anodising (SAA) and tartaric sulfuric acid anodising (TSA) procedures were used to study this independently. Both of them are currently used as alternatives to the historically used chromic acid anodising (CAA) procedures, which contain the toxic Cr^{6+}. Finally, the effect of the addition of ceric sulphate ($Ce(SO_4)_2$) corrosion inhibitor to the anodising bath was investigated too. $Ce(SO_4)_2$ is known for its beneficial effects on the corrosion performance of anodised aluminium alloys when added to either an SAA anodising bath or a TSA anodising bath. [17–20] However, to date is no literature about synergistic effects between anodising electrolyte viscosity, interelectrode distance and the addition of $Ce(SO_4)_2$ to the anodising bath. The research question and hypothesis of this research project are described below.

Research question:
What is the effect of the anodising electrolyte viscosity, the interelectrode distance and the addition of $Ce(SO_4)_2$ to the anodising electrolyte on the corrosion performance of AA2024-T3?

Hypothesis:
Due to the decreased pore diameter [12,14], the increased interpore distance [12,14] and the tighter barrier layer [12], it is expected that an increased viscosity of the anodising electrolyte has a positive influence on the corrosion behaviour of anodised AA2024-T3. The observed improvement of the corrosion performance of titanium in similar circumstances is strengthening the expectation. [16] The expected effect of the interelectrode distance remains unclear because according to literature only the regularity ratio is affected, however depending on the anodising voltage and temperature it could either improve or deteriorate. [15] Last but not least the addition of $Ce(SO_4)_2$ to the anodising bath is expected to have a positive influence on the corrosion performance of AA2024-T3 due to its proven positive effect upon addition to different anodising electrolytes. This includes sulfuric, tartaric and mixed acid electrolytes. [17–20]

1.5. Thesis outline

This thesis consists of five chapters of which chapter one is the introduction. The second chapter is providing the reader with the current literature and necessary background on the topic. The third chapter includes the experimental procedures used in this work. The fourth chapter interprets and discusses the results of this project and last but not least the fifth chapter accommodates the conclusions and recommendations of this work.

2. Literature review

This chapter reviews important literature in order to provide the reader with the necessary background information related to the topic of this work. The chapter is divided into four sections. The first section discusses the properties of aluminium alloys, the second section discusses the basics of corrosion, the third section the basics of anodising and the last section explains corrosion inhibitors.

2.1. Aluminium alloys

Aluminium alloys are classified as either cast or wrought and both are divided in heat-treatable and non-heat-treatable alloys. Cast alloys distinguish themselves from the wrought alloys by the fact they are cast into the desired shape in order to minimize further processing. Wrought alloys are cast into large ingots, which are further processed by mechanical processes, like rolling and extrusion. In this work the cast alloys are not taken into consideration.

2.1.1. Alloy designations

There are nine series of wrought aluminium alloys, each with its own variants. They are designated by a four-digit code of which the first digit indicates the series and the remaining digits the variant within the series. Sometimes the four-digit code has the prefix AA to indicate it is an aluminium alloy. The classification of wrought aluminium alloys is listed below. [2,21]

- 1xxx series: Commercially pure aluminium (at least 99 wt%)
- 2xxx series: Copper
- 3xxx series: Manganese
- 4xxx series: Silicon
- 5xxx series: Magnesium
- 6xxx series: Magnesium and Silicon
- 7xxx series: Zinc
- 8xxx series: Other elements (e.g. iron or tin)
- 9xxx series: Unassigned

Furthermore, aluminium alloys have a temper designation added to the four-digit alloy designation with a hyphen in between. It indicates the type of treatment the alloy has undergone. The temper designations are indicated by a capital letter specifying the general treatment class and a subsequent descriptor digit or digits to distinguish the treatment variant of the treatment class. The temper designations are assigned with F for as-fabricated, O for annealed, H for strain hardened, W for solution heat treated and T for thermally treated other than F, O, or H. The latter is a bit vague because the variants of the T tempers are quite different. The temper designation of AA2024-T3 implies it is solution heat treated, cold worked and naturally aged to a substantially stable condition. [21]

2.1.2. Microstructure of AA2024-T3

AA2024-T3 is an aluminium alloy with copper and magnesium as its main alloying elements. The compositional limits of the alloy are shown in Table 2.1. Due to its low density and superior mechanical properties AA2024-T3 is typically used in airplane wings and fuselage. [21] Typical properties are a yield strength of 345 MPa, an ultimate tensile strength of 483 MPa, a Young's modulus of 73 GPa and a fatigue endurance limit of 138 MPa. [21]

	Al	Cu	Mg	Mn	Fe	Si	Zn	Ti	Cr	Other
Min	Rest	3.8	1.2	0.3	0	0	0	0	0	0
Max	Rest	4.9	1.8	0.9	0.50	0.50	0.25	0.15	0.10	0.15

Table 2. 1: Compositional limits of AA2024-T3. All in wt%. [22]

Figure 2.1 shows a micrograph, obtained with a scanning electron microscope, of a typical microstructure of AA2024-T3. [23] As is evident from this image the alloy has many intermetallic particles (IMs). Typically the IMs of AA2024-T3 are divided into two groups based on their overall chemical composition: the Al-Cu-Mg group and the Al-Cu-Mn-Fe group. [23] However, sometimes a third group is identified with the overall chemical composition of Mg-Si and to a lesser extend the other alloying elements. [24] Since the composition of the IMs are often heterogeneous, various smaller regions with a similar composition are identified. Often reoccurring are the S-phase [25] with a stoichiometry according to Al_2CuMg and the θ-phase [26] with a stoichiometry according to Al_2Cu. The black coloured numbers in Figure 2.1a indicate the IMs belonging to the Al-Cu-Mg group, while the blue coloured numbers indicate IMs of the Al-Cu-Mg-Fe group. The non-labelled dark grey area (i.e. the matrix) is a solid solution of aluminium with a small fraction of its alloying elements. [23] The wide variety of IMs give AA2024-T3 its distinct microstructure and sublime mechanical properties in comparison to pure aluminium.
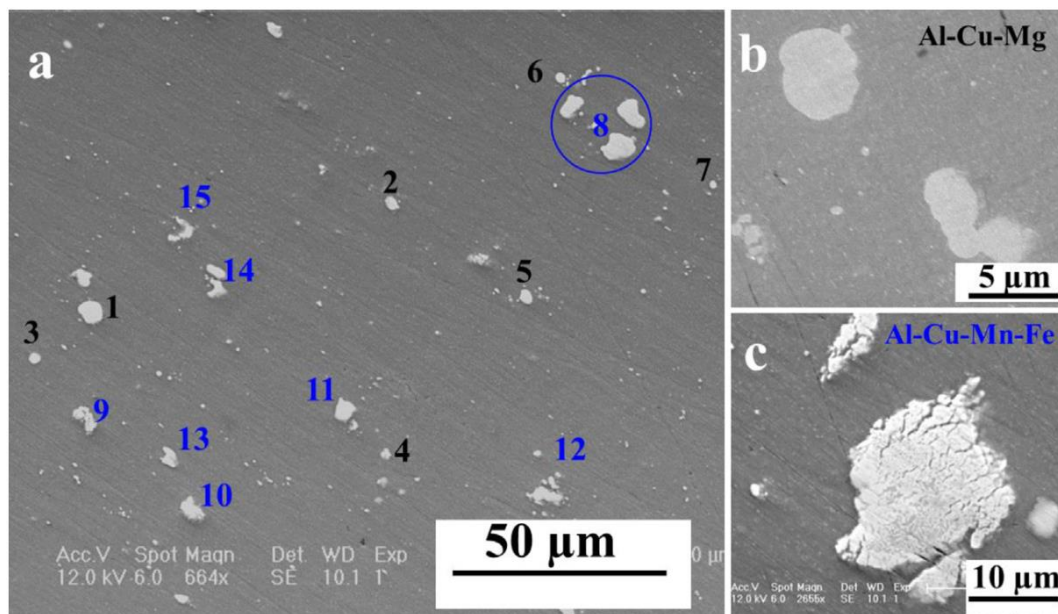
Figure 2. 1: SEM images of a typical microstructures of AA2024-T3. 2.1a overview. 2.1b details of some Al-Cu-Mg IMs 2.1c details of some Al-Cu-Mn-Fe IMs. [23]

6

2.1.3 Passivity of aluminium and its alloys

The fact that aluminium naturally forms a thin (typically 3-6 nm [27]) uniform oxide layer of aluminium oxide (Al_2O_3) is by itself not very special. As long as the environmental conditions are right, other metals show this passive behaviour too. [3,5] However, for aluminium the range in which passive behaviour is occurring is very convenient for most applications, see the Pourbaix diagram in Figure 2.2a. If the pH of the environment is between 4.0 and 8.5 aluminium is passive, meaning a layer of Al_2O_3 is formed. At a pH below 4.0 aluminium is corroding as trivalent aluminium ions (Al^{3+}). If the pH is higher than 8.5 aluminium starts corroding too, but now it dissolves in the form of aluminate ions (AlO_2^-). [3] The Pourbaix diagram however does not take alloying conditions into account. Besides the presence of electrolyte substances such as chlorides, the operating temperature, the mode of corrosion and the reaction rate are neglected. Taking these factors into account should be done on a case by case basis. Figure 2.2b shows the altered Pourbaix diagram of aluminium alloy 5086 (temper unknown) taking into account all of the above. [3]
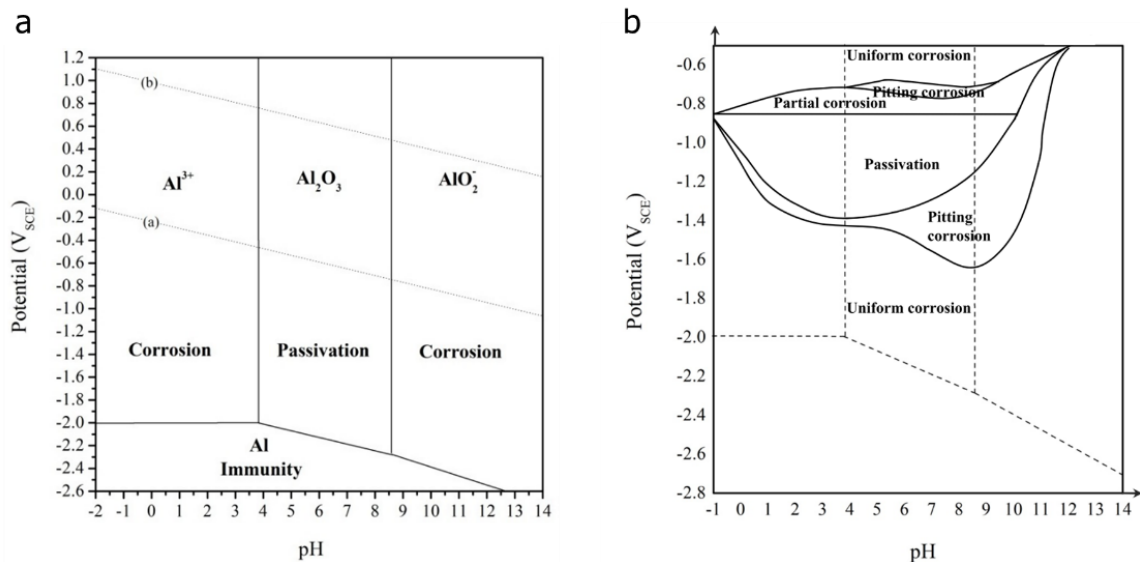
Figure 2. 2: Pourbaix diagrams. 2.2a diagram of aluminium at 25 °C in aqueous solution. 2.2b diagram of aluminium alloy 5086 at 25 °C in 0.5M NaCl aqueous solution. [3]

2.2. Corrosion of aluminium and aluminium alloys

Corrosion is the degradation of a material caused by the interaction with its environment. Three different types of corrosion could be identified and are described below. [5]

1. Wet corrosion: material degradation in an aqueous environment with dissolved species.
2. Dry corrosion: material degradation in a dry gaseous environment. It is often called chemical corrosion and one of the examples is high-temperature corrosion.
3. Non-aqueous corrosion: material degradation in a non-aqueous environment, like molten salts.

Since this work is about wet corrosion, the term corrosion in this work refers to the first definition listed above.

2.2.1. Corrosion of aluminium

Corrosion is an electrochemical process consisting of two so called half-reactions, the anodic and the cathodic half-reaction, both taking place on the same material. During corrosion a metal is transformed into a metal ion by releasing one or more electrons in a reaction called oxidation at an anodic site, see Equation 2.1 for the oxidation of aluminium. Simultaneously at a cathodic site on the same metal the reduction is taking place, using the electrons from the anodic sites to transform certain species from the electrolyte into new ones. A common cathodic reaction is the reduction of oxygen which takes place in alkaline (pH ≥ 7) aerated aqueous environments. It transforms oxygen and water molecules into hydroxide ions, see Equation 2.2. Together, the anodic and cathodic reaction make the total corrosion process, see Equation 2.3 for the general corrosion process of aluminium. The metal ions may recombine with the hydroxide ions in order to form all kinds of metal hydroxides, oxides or oxyhydroxides. Figure 2.3 shows the corrosion process of aluminium in a neutral aerated aqueous environment. [5,28]

Oxidation	$4Al\ (s) \rightarrow 4Al^{3+}(aq) + 12e^-$		(2.1)
Reduction	$3O_2\ (g) + 6H_2O\ (l) + 12e^- \rightarrow 12OH^-(aq)$	$+$	(2.2)
Overall	$4Al\ (s) + 3O_2\ (g) + 6H_2O\ (l) \rightarrow 4Al^{3+}(aq) + 12OH^-\ (aq)$		(2.3)
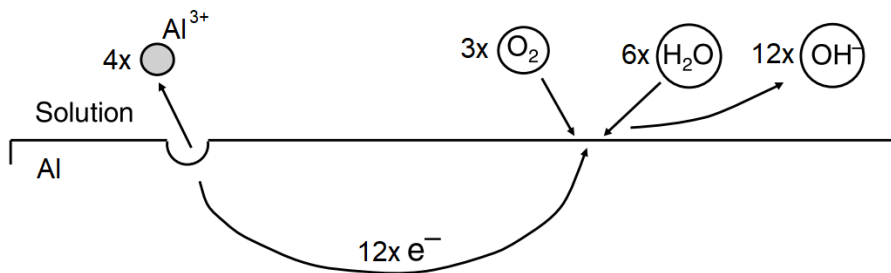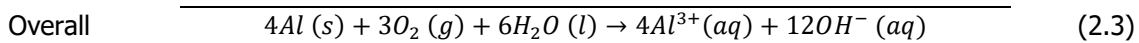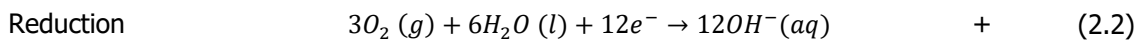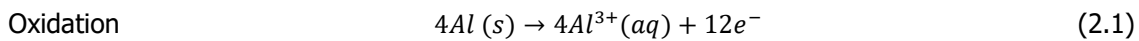
Figure 2. 3: Schematic representation of general corrosion of aluminium. [3,28]

Depending on the environmental conditions, the cathodic half-reaction may differ. There are two main factors influencing the half-reaction at the cathodic sites: the concentration of oxygen and the pH of the corrosive solution. Equations 2.4, 2.5 and 2.6 show the three possible cathodic reactions. In reality often a mixture of different cathodic half-reactions will occur, due to local chemical differences of the electrolyte, especially in near neutral electrolytes (pH ≈ 7). [5,28]

pH ≤ 7, no oxygen	$2H^+\ (aq) + 2e^- \rightarrow H_2\ (g)$	(2.4)
pH ≤ 7, oxygen	$O_2\ (g) + 4H^+\ (aq) + 4e^- \rightarrow 2H_2O(l)$	(2.5)
pH ≥ 7, no oxygen	$2H_2O\ (l) + 2e^- \rightarrow H_2\ (g) + 2OH^-(aq)$	(2.6)
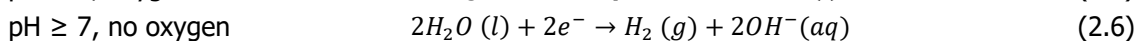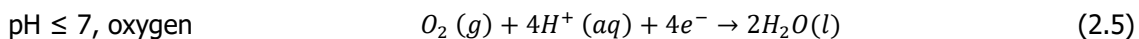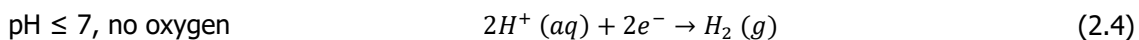
2.2.2. Corrosion of aluminium alloys

For environments with a pH between 4.0 and 8.5 the aluminium ions react with oxygen ions or hydroxide ions (from the reduction reaction or the dissociation of water) to form Al_2O_3 see Equations 2.7. Recombination with oxygen ions originating from the dissociation of hydroxide ions in aqueous solutions in order to form a passive layer of Al_2O_3 may happen too, see Equation 2.8. Often the oxidation and recombination reactions are written as one net half-reaction, see Equation 2.9.

8

Oxide formation 1	$2Al^{3+}(aq) + 3OH^-(aq) \rightarrow Al_2O_3\ (s) + 3H^+\ (aq)$	(2.7)

Oxide formation 2	$2Al^{3+}\ (aq) + 3O^{2-}\ (aq) \rightarrow Al_2O_3\ (s)$	(2.8)

Net reaction	$2Al\ (s) + 3H_2O\ (l) \rightarrow Al_2O_3\ (s) + 6H^+ + 6e^-$	(2.9)
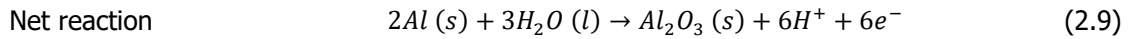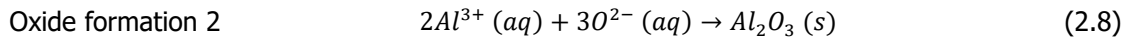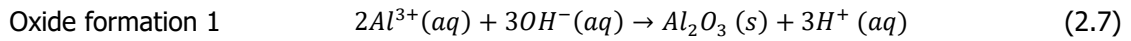
From the theory of electrochemistry it is known that all materials used as electrodes come with their own standard electrode potential when immersed in their standard electrolyte at standard conditions (1 M of native ions at 25 °C). One of the pioneers in the field, Walther Nernst, defined the standard electrode potential as the result of the interplay between an electrode's tendency to go into solution in the form of ions (electrolytic pressure of dissolution, P_e) and the tendency of the ions in solution to be deposited onto the electrode (osmotic pressure of the dissolved ions, P_o). [29] If P_e is bigger than P_o, more ions from the electrode go into solution, leaving an electrode with an excess of electrons giving it a negative charge. On the other hand, if P_o is bigger than P_e ions in solution like to deposit on the electrode causing a shortage of electrons, which gives it a positive charge. [29] The electric charge of the electrode results in the attraction of either cations or anions from the electrolyte, forming so called electric double layer. [5,28] The charge distribution at the electrode-electrolyte interface is responsible for the potential. Moreover, the electrode potential (in contrast to the standard electrode potential) depends on the electrolyte conditions. More specifically it depends on the thermodynamic activity of the product and reactants associated with the electrode half-reaction and the temperature. Equation 2.10, the Nernst Equation, describes the relation between the standard electrode potential and the electrode potential. In this Equation E is the electrode potential, E^0 is the standard electrode potential, R is the gas constant, T is the absolute temperature, n is the number of electrons involved, F is the Faraday's constant, a_P is the thermodynamic activity of the products and a_R is the thermodynamic activity of the reactants. [5,28,29]

Since electrode potentials are not measurable in absolute sense, they are always reported in literature versus another electrode potential. Arbitrarily the standard hydrogen electrode (SHE) is set at 0 V versus SHE. [28]

Nernst Equation	$$E = E^0 - \frac{RT}{nF}\ln\left(\frac{a_P}{a_R}\right)$$	(2.10)

When two different metals are electrically connected, one will start acting as the anode and the other as the cathode depending on their electrode potentials. Thus, the metal with the lowest (more negative) potential will act as the anode and will be dissolved. As already discussed in section 2.1, aluminium alloys (e.g. AA2024-T3) often consist a large amount of IMs. Based on the chemical differences between the matrix and the IMs and between different IMs, some areas are more likely to act as local anodes or local cathodes than others. This is caused by a difference in the electrode potentials. Figure 2.4a and b show the situation when an IM is acting as the cathode because of a higher electrode potential compared to the aluminium matrix. The aluminium matrix starts corroding around the particle, resulting in a detached IM leaving a pit in the matrix. Figure 2.4c and d show the situation when an IM is acting as a local anode because of its lower electrode potential compared to the matrix. In this situation the aluminium matrix remains untouched and

the particle is corroding. After some time the particle is fully dissolved, leaving a pit in the aluminium substrate behind. Both situations results in local pits in material which may act as stress concentrators and therefore lower the structural integrity of the material. [30] Therefore, the IMs in aluminium alloys create weak spots in the passive layer and micro galvanic coupling between the aluminium matrix and the IMs increase the sensitivity to localised corrosion.
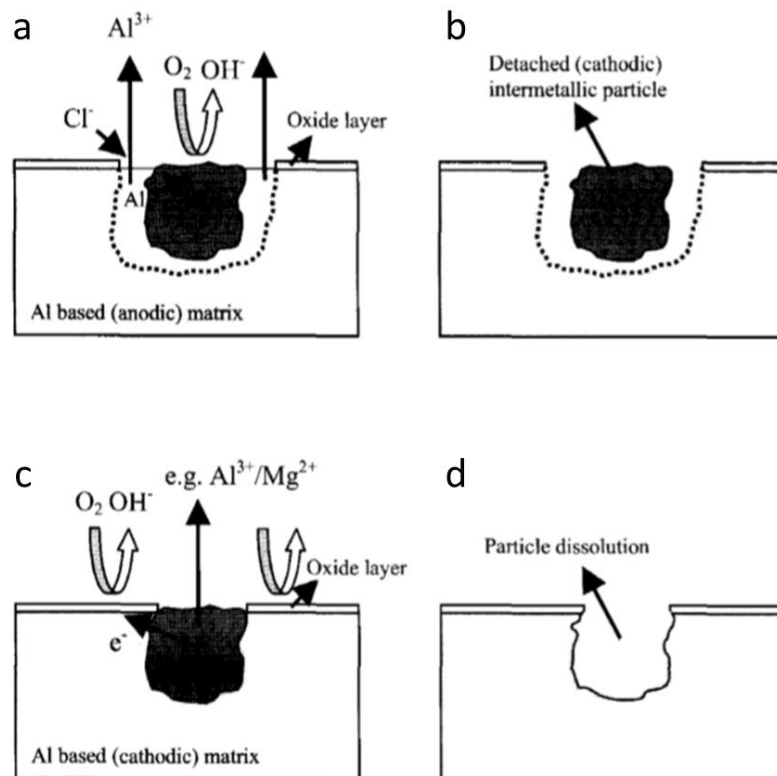
Figure 2. 4: Localised corrosion on aluminium alloys. [31]

2.2.3. Corrosion testing

Corrosion performance could be characterised in many different ways, both quantitatively and qualitatively. Due to the high complexity of the corrosion process two or more techniques are often used in order to adequately characterise the corrosion behaviour. It depends on the material, the environmental conditions and the requested information which techniques are most suitable. [32] In this work two different electrochemical methods were used to assess the corrosion performance of the different anodising pre-treatments in an aqueous saline environment: Linear Sweep Voltammetry (LSV) and Electrochemical Impedance Spectroscopy (EIS). Only these techniques are discussed in more detail.

LSV and EIS are electrochemical techniques in which a three-electrode experimental set-up (also called a three-electrode electrochemical cell) consisting of a working electrode, a reference electrode and an counter electrode is used. [33–35] The substrate to be examined is acting as the working electrode, the reference electrode is an electrode with a stable electrode potential and the counter electrode (also called auxiliary electrode) is typically an inert material, like platinum or graphite. During LSV and EIS measurements all electrodes are immersed in the testing electrolyte and connected to a device called a potentiostat which controls either current or potential, while measuring the other one. During these experiments current may pass between the working

10

electrode and the counter electrode, while the potential of the working electrode is always determined versus the reference electrode. [33–35] Figure 2.5 shows a schematic overview of a three-electrode set-up.
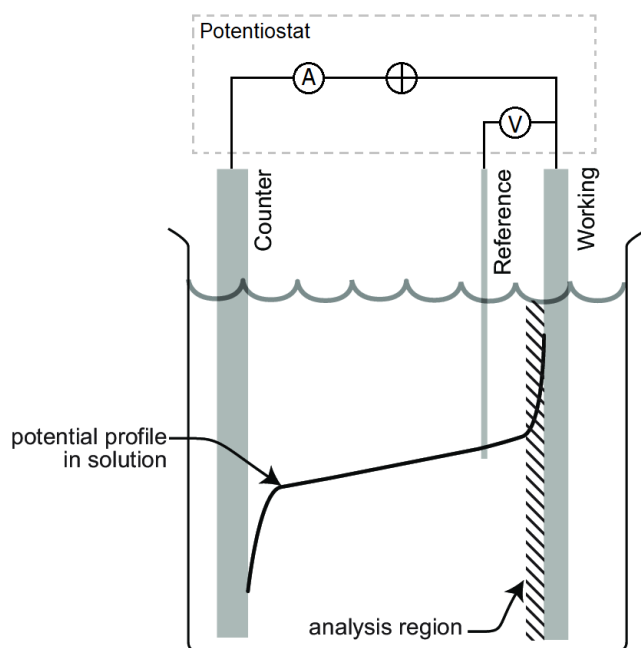
Figure 2. 5: Schematic overview of a three-electrode set-up. [33,35]

Before commencing any electrochemical measurements like LSV or EIS, electrochemical cells need some time (ranging from minutes to hours) to get a stable working electrode potential which is measured as the open-circuit potential (OCP) between the working electrode and the reference electrode. [36] During this stabilisation time no current is passing between the working electrode and the counter electrode. In the beginning of the immersion of a sample into the electrolyte, OCP is changing for some time because the oxidation and reduction reactions happening at the surface of the material in question are not in equilibrium yet. After some time an equilibrium will be established which means that the measured OCP could now be seen as the equilibrium potential (E_{eq}) or in case of corrosion the corrosion potential (E_{corr}).

During the LSV measurement the potential of the working electrode is changing from its equilibrium value with a slow constant scanning rate, resulting in a current flow (to or from the counter electrode), which is recorded. The change of the working electrode potential is called polarisation and depending on the direction, above or below the OCP, it may be called positive or negative polarisation. Due to the slow scanning rate the technique is a (quasi) steady-state technique. The difference between applied potential (E) and the equilibrium potential (E_{eq}) is called overpotential (η). Current (I) is typically normalised to current density (i). A resulting potential-current density curve (E-i curve) is called a polarisation curve. Often, in corrosion studies, the logarithm of the absolute current density values is presented instead of regular current density values due to the large differences. The resulting representation (E-log(|i|) curve) may be called Tafel plot when activation polarisation could be observed at overpotentials higher than 118 mV (at 25 °C). This implies that the back reaction is contributing less than 1% of the current. [33] Depending on the scanning direction the current is increasing or decreasing during a measurement.

Shift of the electrode potential away from the equilibrium value resulting in current flow is called polarisation. [33] Three different kinds of polarisation could be identified: activation polarisation, concentration polarisation and ohmic polarisation. Activation polarisation is related to the actual charge transfer reaction at the electrode surface, concentration polarisation is related to the mass transfer of charged species to or from the electrode surface and ohmic polarisation is related to the presence of oxides or adsorbed species on the electrode surface or the electrical resistance of the electrolyte. [28] In the theory of electrochemistry the relationship between overpotential and current density is well defined in the current density-overpotential Equation (i-η Equation), shown as Equation 2.11. This Equation is simplified by neglecting the mass transfer effects, which results in the Butler-Volmer Equation (Equation 2.12). In these Equations i is the current, i_0 is the exchange current (or corrosion current), $C_O(0,t)$ is the surface concentration of oxidised species, C_O^* is the bulk concentration of oxidised species, α is the transfer coefficient, f is F/RT (which comprises Faraday's constant F, gas constant R and absolute temperature T), η is the overpotential, $C_R(0,t)$ is the surface concentration of reduced species and C_R^* is the bulk concentration of reduced species. [33]

i-η Equation

$$i = i_0 \left(\frac{C_o(0,t)}{C_o^*} e^{-\alpha f \eta} - \frac{C_R(0,t)}{C_R^*} e^{(1-\alpha)f\eta} \right) \quad (2.11)$$

Butler-Volmer

$$i = i_0 \left(e^{-\alpha f \eta} - e^{(1-\alpha)f\eta} \right) \quad (2.12)$$

Negative polarisation forces the working electrode to act as the cathode which results in a cathodic current, while positive polarisation forces it to act as the anode resulting in an anodic current flowing from working electrode to counter electrode. In corrosion research two different ways of scanning are commonly used. The first one polarises the working electrode to the minimum potential of interest in a step like fashion, after which the potentiostat starts scanning towards higher potentials. [28,36] This causes an instant rise of the cathodic current followed by a gradual decrease till zero at the equilibrium potential. As soon as the potential is crossing the equilibrium potential the current direction will flip and change from a decreasing cathodic into an increasing anodic current until the final potential of interest is reached. Another approach is to separately scan the anodic or cathodic regime on two identical samples from the equilibrium potential in positive direction (anodic scan) or negative direction (cathodic scan) and later combine the data into one complete polarisation curve. [28,36] The latter method makes sure that the initial cathodic scanning regime is not altering the sample's surface before commencing into the anodic regime. By polarising the working electrode both anodically and cathodically, information about the reaction kinetics of the anodic and cathodic reactions respectively is obtained. Normally both reactions are taking place simultaneously on the materials' surface in non-polarised circumstances (i.e. at E_{corr}). [28] According to the mixed potential theory (which states that the two half-reactions of an electrochemical process will find a common equilibrium potential in between the equilibrium potentials of the two separate half-reactions [37]) and the assumption that the measured current response is fully caused by the charge transfer kinetics (activation polarisation), the trendlines of both anodic and cathodic reactions could be extrapolated to end up with the corrosion potential (E_{corr}) and the corrosion current (I_{corr}), at the intersection of the extrapolated lines, which is normalised to the corrosion current density (i_{corr}). Figure 2.6 shows how a typical polarisation curve

depicted as a Tafel plot could be extrapolated in order to obtain the corrosion current, which is directly related to the rate of corrosion by Equation 2.13. In this Equation r is the corrosion rate in unit of length per unit of time (e.g. mm/yr), a is the molar mass of the corroding material, n is the number of electrons involved in the anodic half reaction, F is Faraday's constant, i is the recorded current density and D is the density of the corroding material.

Corrosion rate
$$r = \frac{ai}{nFD}$$
(2.13)
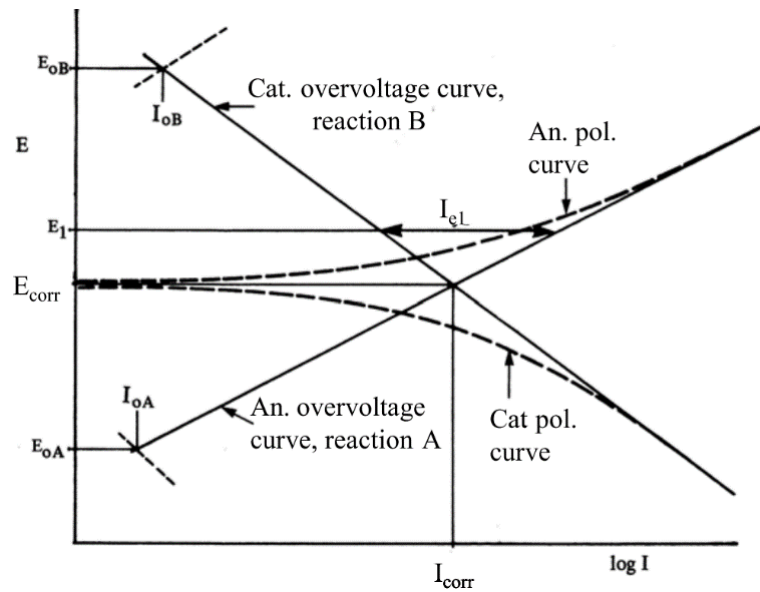
Figure 2. 6: Tafel plot extrapolation. [5]

Another way to quantitatively interpret polarisation curves is to determine the linear polarisation resistance (R_p), using only a small semi-linear portion of the full curves around the corrosion potential (e.g. ± 10 mV vs E$_{corr}$). [36] The slope of the linear portion is equal to the linear polarisation resistance, which depends the corrosion resistance of the material. In order to determine the slope, the polarisation is plotted as a regular E-i plot (both linear scales), see Figure 2.7. The slope is calculated according to Equation 2.14. The linear polarisation resistance value is directly related to the corrosion current (i_{corr}) by Equation 2.15, called the Stern-Geary Equation. [5,28] The terms b_a and b_c are the slopes of the anodic and cathodic extrapolation lines of the full Tafel plots, called the Tafel slopes. Based on this Equation it is evident that linear polarisation is inversely proportional to the corrosion current density.

LPR
$$R_p = \frac{\eta}{i}$$
(2.14)

Stern-Geary
$$i_{corr} = \frac{1}{2.303 R_p \left(\frac{1}{b_a} + \frac{1}{|b_c|} \right)}$$
(2.15)
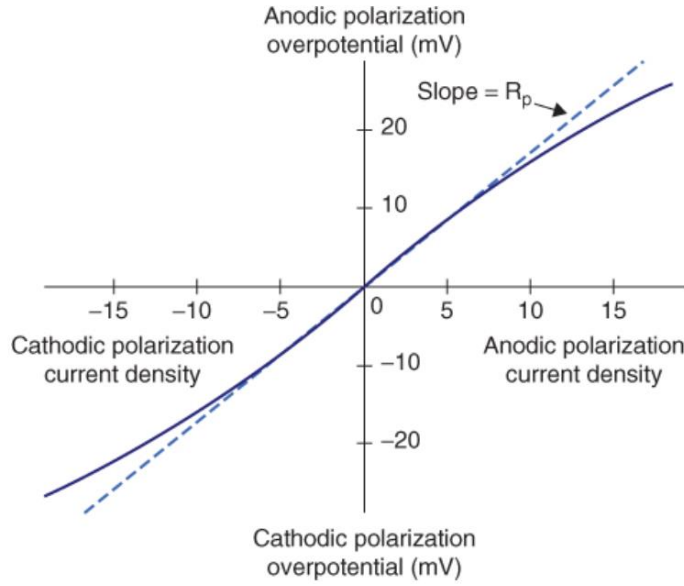
Figure 2. 7: Linear polarization resistance determination. [38]

EIS is a technique which applies small periodic perturbation signals (either current or potential) to an electrochemical system while recording the system response. [36,39] In corrosion research typically a sinusoidal potential with a fixed amplitude between 10 and 50 mV is applied to the material and the current response is recorded. [36,39] EIS records the system response over a wide range of discrete frequencies, resulting in a wide range of different system responses, hence its spectroscopic nature. Since both the periodic potential (V) and the periodic current (I) are of the sinusoidal type they could be described according to Equation 2.16 and 2.17 using cosines, however they could also be represented as the real part of their respective complex exponential expressions due to Euler's relationship. [36,39] This mathematical relationship relates trigonometric functions to complex exponential functions. [40] In these Equations $V(t)$ is the periodic potential at time t, V_0 is the amplitude of the period potential, ω is the angular frequency, $I(t)$ is the periodic current at time t, I_0 is the amplitude of the periodic current, ϕ is the phase angle between potential and current and $Re\{\}$ is indicating the real part of the complex expression in between the curly brackets. Equation 2.19 describes Euler's relationship between trigonometric - and complex exponential functions. The applied periodic potential and recorded periodic current allow the determination of the impedance of the system at every tested frequency according to Equation 2.18. In this Equation $Z(t)$ is the impedance as a function of time t and Z_0 is the ratio between V_0 and I_0.

Potential
$$V(t) = V_0 \cos(\omega t) \to Re\{V_0 e^{i\omega t}\} \tag{2.16}$$

Current
$$I(t) = I_0 \cos(\omega t - \phi) \to Re\{I_0 e^{i(\omega t - \phi)}\} = Re\{I_0^* e^{i\omega t}\} \tag{2.17}$$

Impedance
$$Z(t) = \frac{V(t)}{I(t)} = \frac{V_0 \cos(\omega t)}{I_0 \cos(\omega t - \phi)} \to \frac{Re\{V_0 e^{i\omega t}\}}{Re\{I_0 e^{i(\omega t - \phi)}\}} = Re\{Z_0 e^{i\phi}\} \tag{2.18}$$

Euler's formula
$$e^{ix} = \cos(x) + i \sin(x) \tag{2.19}$$

14

During EIS, a perturbation potential is applied and the current response is recorded. Software analyses the data and calculates all unknowns from the data, like phase angle and impedance, after which the data is presented. Typically the data is presented as complex impedance which includes the imaginary part in the form of either a Nyquist plot (also called a complex plane plot or an Argand diagram [39]) or Bode plots (magnitude and phase angle [39]). Figure 2.8a is showing a typical Nyquist plot of a simple system with the imaginary part of the complex impedance on the y-axis and the real part on the x-axis. Every point on the semicircle represents the complex impedance of the electrochemical system at a specific frequency. Nyquist plots do not clearly indicate the frequency. However, from the theory it is well-known that the right side of the semicircle on the real axis represents the lower frequency region (indicated as $\omega \rightarrow 0$). [39] The left side on the other hand is indicated by $\omega \rightarrow \infty$, which indicates the high frequencies. [39] A line (or arrow) from the origin to any point on the semicircle gives a graphical representation of the complex impedance. Its length is equal to the absolute value $|Z|$ (or Z_0 as it was called before) and the angle between the arrow and the positive x-axis is the argument $arg(Z)$. The argument of Z is the same as the phase angle (or ϕ as it was called before) at that specific frequency. Figure 2.8b and c show the Bode plots of the same simple system. The magnitude plot shows absolute value of the complex impedance as a function of frequency while the phase plot shows the phase angle as a function of frequency.
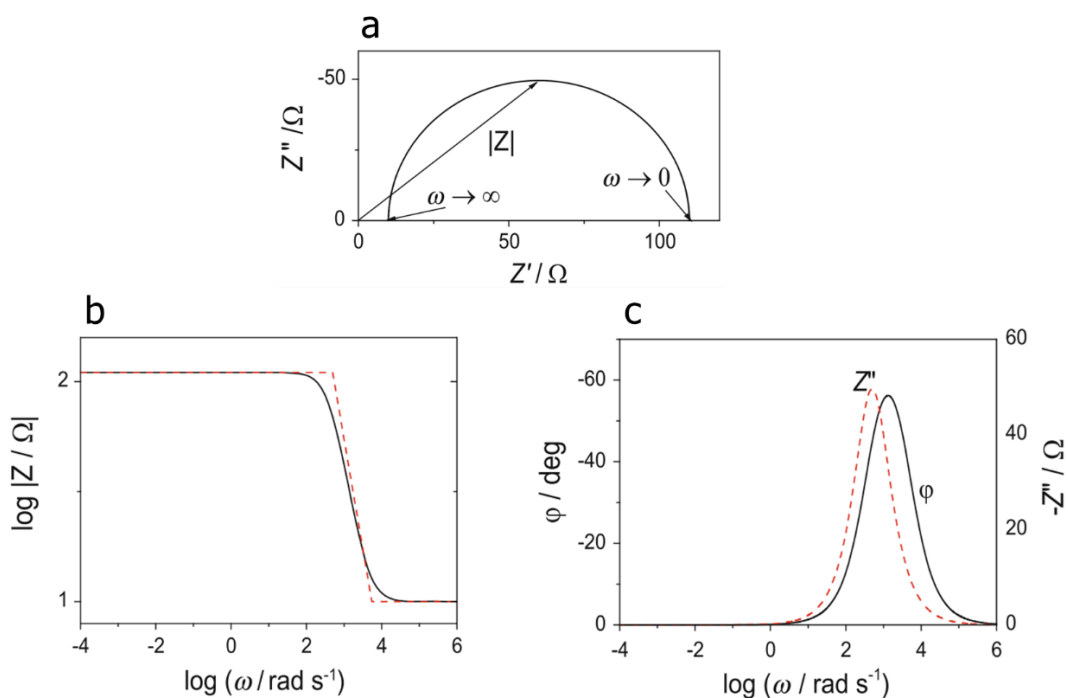
Figure 2. 8: EIS data representation. 2.8a Nyquist plot, 2.8b Bode plot (magnitude) and 2.8c Bode plot (phase angle). [39]

From the theory on AC-circuits it is well-known that out of the three basic electrical elements (resistor, capacitor and inductor) two are responsible for a phase shift between potential and current. Combinations of basic electrical elements and variants of them make it possible to create an electrical circuit which approximates the recorded behaviour of an electrochemical system. For this reason so called equivalent electrical circuit (EEC) models are used to find the values of all

separate parts of the circuit, which are in turn correlated to specific parts and behaviour of the electrochemical system. [36,39]

In this work EIS was not used to find a specific equivalent circuit in order to gain detailed information about the electrochemical system. The non-invasive nature of the small perturbation signals were the reason for using EIS to get deeper insight of the corrosion behaviour of the anodised samples over time. For this purpose mainly the low frequency region of an EIS scan is being studied as the impedances at these frequencies (typically < 1 Hz) offer a good indication of the corrosion performance. [39,41] As the frequency goes to zero the impedance measurement is mimicking the same (quasi) steady-state conditions as is done with LSV, which means that the impedance at the lowest frequencies are a good indication of the polarisation resistance. Figure 2.9 is showing three Bode plots (both magnitude and phase angle) of a steel coated with an alkyd enamel. The curves indicated with the letter *a* represent the EIS results after 43 days of exposure in a 0.5 M NaCl solution. The other curves (*b* and *c*) represent the results after 90 days and 162 days of exposure respectively. When looking at the impedances in the low frequency region a clear decrease in impedance from ~10^7 to ~10^4 is visible indicating a decrease in corrosion performance with increasing time of exposure caused by poorer coating protection. Similar trends were observed for AA2024-T3 anodised in 90 mg/mL sulfuric acid after prolonged salt spray testing (5 wt% NaCl, 40mL/h, 35 °C) as measured in a 3.5 wt% NaCl electrolyte, see figure 2.10. [42] Research by Zheludkevich et al. [41] has shown the usability of this same principle as a routine procedure to check the self-healing properties of active protective coatings. In literature often the impedance values at 0.01 or 0.1 Hz is plotted as a function of immersion time. This offers a way to monitor the corrosion performance over time.
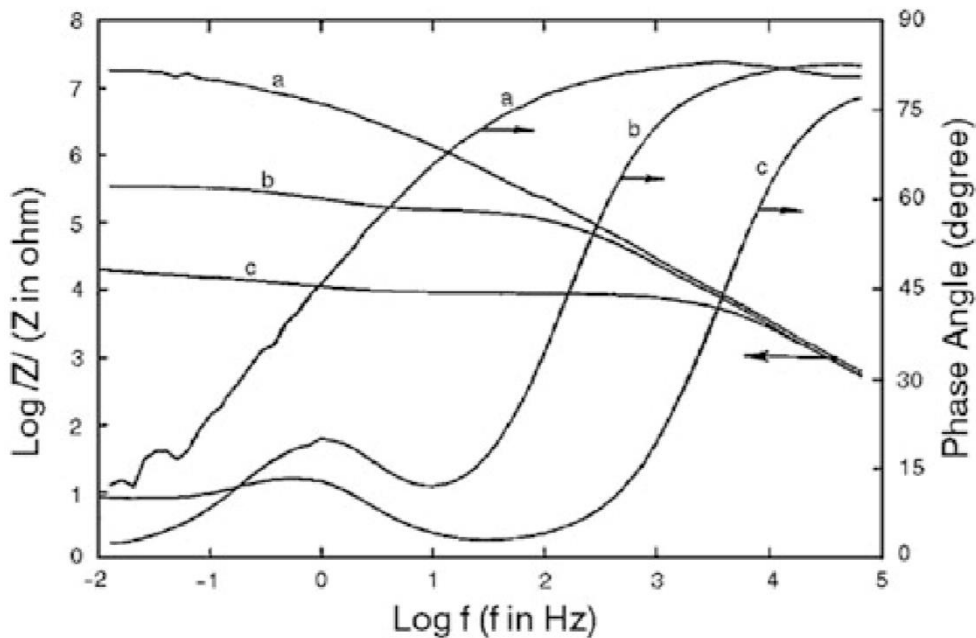
Figure 2. 9: Bode plots of a steel coated with an alkyd enamel. [39]
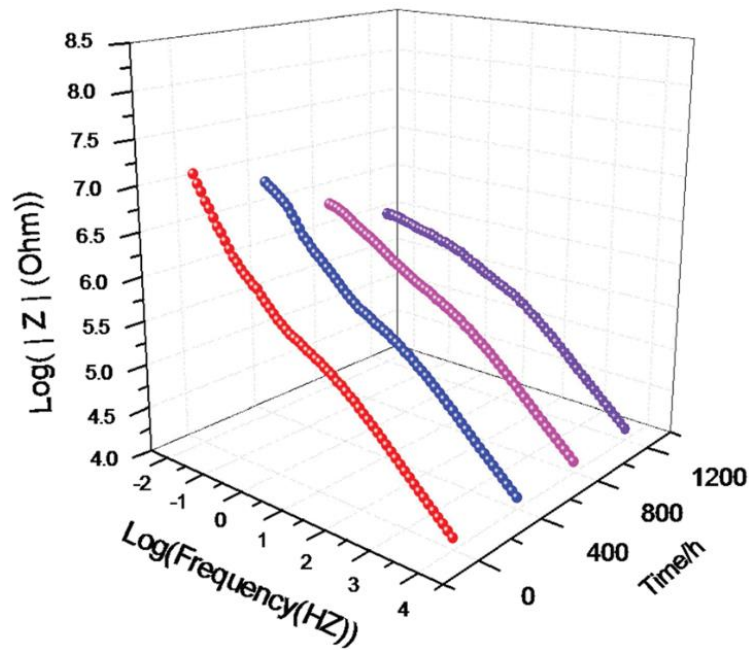
Figure 2. 10: Bode plots (magnitude) of AA2024-T3 anodised in 90 mg/mL sulfuric acid after prolonged salt spray testing (5 wt% NaCl, 40mL/h, 35 °C) as measured in a 3.5 wt% NaCl electrolyte. [42]

2.3. Anodising

Anodising is an electrochemical pre-treatment method. The pre-treatment is the first step in a corrosion protective scheme, right after a thorough cleaning procedure, in order to increase the corrosion performance and to improve the adherent properties of the material towards either a coating or an adhesive. [7] In this section the fundamentals of anodising are introduced.

2.3.1. Fundamentals

Anodising is an electrolytic passivation process that capitalises a materials' capability to form a protective layer. It used to create an anodic oxide layer by anodically polarising the material. [10,11] The material is therefore connected to the positive terminal (+ pole) of a DC power supply and immersed in an electrolyte, see Figure 2.11. The power supply may either apply a fixed potential and record the anodising current (potentiostatic) or apply a fixed current and record the potential (galvanostatic). In industry often the potentiostatic method is used because of the often complex shapes of the products to be anodised. The electrolyte may be acidic, neutral or alkaline. However, for corrosion or adhesion related applications typically an acidic electrolyte is used. An inert material, like platinum, is also immersed in the same electrolyte and connected to the negative terminal (- pole) of the same power supply. Anodic polarisation forces the substrate the act as the anode while the inert material acts as the cathode. Depending on the electrolyte and electrodes different reactions may occur during the anodising process. Just as with the corrosion process of aluminium, during anodising aluminium will transform from its metallic state to its ionic state and recombines with dissociation products of water to Al_2O_3 (section 2.2.1 and 2.2.2). The big difference between the two is the much larger driving force of the reaction for the anodising process which is caused by the anodic polarisation. [10]

The good electrical insulating properties of formed aluminium oxide give rise to a large potential drop over a very short distance at the metal/electrolyte interface. This causes the

17

formation of an electric field strong enough to cause migration of ionic oxygen and hydroxide through the oxide layer. Upon arrival at the metal/oxide interface these ionic species recombine with the metal ions to form an oxide. However, not all metal ions do recombine at the metal/oxide interface. Some will migrate through the oxide layer towards the oxide/electrolyte interface where they might recombine with oxygen or hydroxide ions. A small portion will not form an oxide at all. These aluminium ions will directly go into the electrolyte. [10]
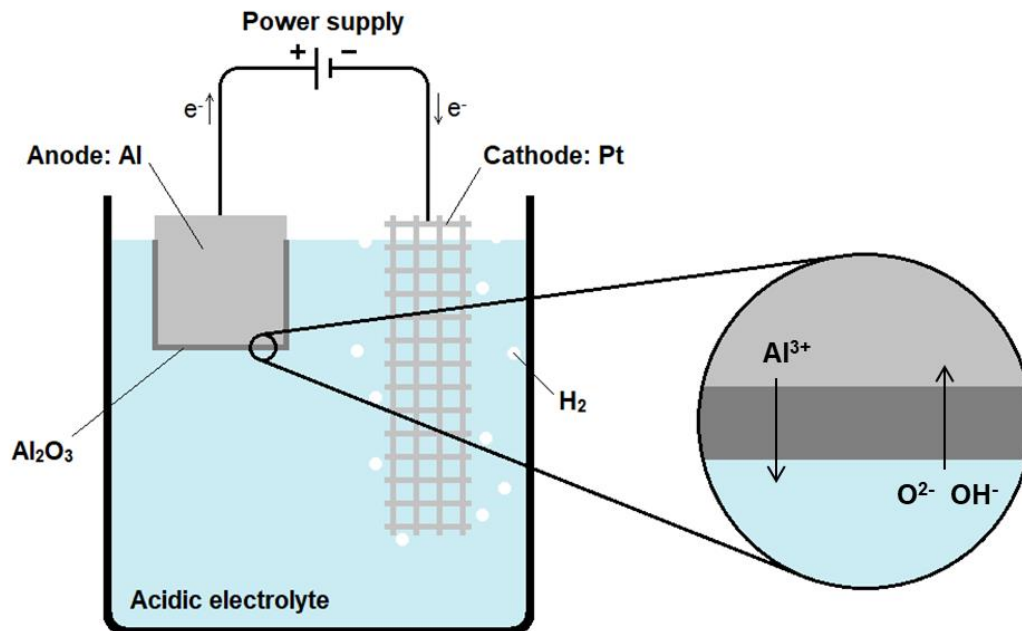
Figure 2. 11: Schematic overview of an anodising cell. Drawing based on information given in [10].

2.3.2. Film types

Depending on the anodising electrolyte different anodic oxide film types may be created, either a barrier type or a porous type. [10] Barrier anodic oxides are oxides which form a nice uniform layer covering the whole surface of the metal, just like its native oxide. They tend to form in electrolytes which are of near neutral pH and therefore not aggressive towards aluminium oxide. Using near neutral electrolytes has a distinct effect on the anodising process. Looking at the potential response (galvanostatic) and the current response (potentiostatic) of a material being anodised in such an electrolyte, see Figure 2.12, different trends are observed. Applying a constant current results in a rising potential (2.12a) because of the increase in thickness of the oxide layer. In order to keep the electric field strength the same the potential is rising. At some point the oxide layer becomes too thick for current to pass, which means that the potential stops rising and remains constant. Sometimes sparking on the surface may be observed which is reflected by the irregular oscillations in the curve. When applying a constant potential at first a very high current is measured which drops with increasing oxide thickness, see Figure 2.12b. Eventually the oxide becomes too thick to sustain significant current flow. A very low and constant current remains due to small defects in the oxide.

18
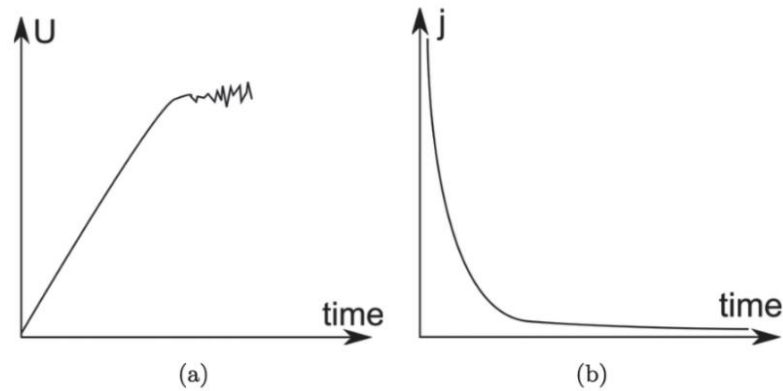
Figure 2. 12: Potential and current characteristics of the formation of a barrier type anodic oxide. 2.12a Galvanostatic anodising. 2.12b Potentiostatic anodising. [10]

More aggressive electrolytes introduce a new counteracting reaction to the anodising process which dissolves the oxide layer. In acidic electrolytes this reaction looks like the one described by Equation 2.20. The interplay between the oxide forming and oxide dissolving reactions give rise to a specific potential or current response depending on the anodising technique used, see Figure 2.13. Potentiostatic anodising gives rise to a high initial current which drops rapidly during typically the first few second because of the formation of a barrier type anodic oxide (often referred to as the barrier layer of a porous type anodic oxide). This is indicated as the first stage (I) in the potentiostatic graph. In stage II the rapid drop of current is slowed down due to the development of some penetration paths created by the aggressive electrolyte. These paths allow easier current flow through the oxide due to lower local resistance. As a consequence the electric field over the film will concentrate over these regions, which causes pores to develop. This is happening in stage III. The formation of pores comes with an increase in current because the regions of lower resistance are increasing in size in this stage. At the beginning of stage IV the initiation of pores stabilizes and they start growing at a constant rate which results in a constant current. The potential behaviour during galvanostatic anodising is similar to the current behaviour during potentiostatic anodising, but inverted. [10,43] The typical morphology of porous anodic oxide layer, already shown in Figure 1.1, depends on a lot of anodising parameters. For potentiostatic anodising the applied anodising voltage, the type of electrolyte and the electrolyte temperature are very important factors having a major influence on the morphology. Typically an increase in the anodising voltage and/or the electrolyte temperature result in an increase in the oxide growth rate, an increase in barrier layer thickness, an increase in pore diameter and an increase in interpore distance. Other less obvious parameters, like anodising electrolyte viscosity, interelectrode distance and incorporation of corrosion inhibitors, will be discussed in the remainder of this chapter.

Oxide dissolution $\qquad Al_2O_3(s) + 6H^+(aq) \rightarrow 2Al^{3+}(aq) + 3H_2O(l)$ $\qquad$ (2.20)
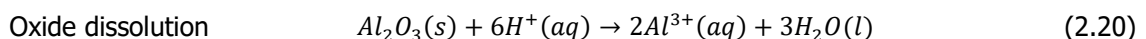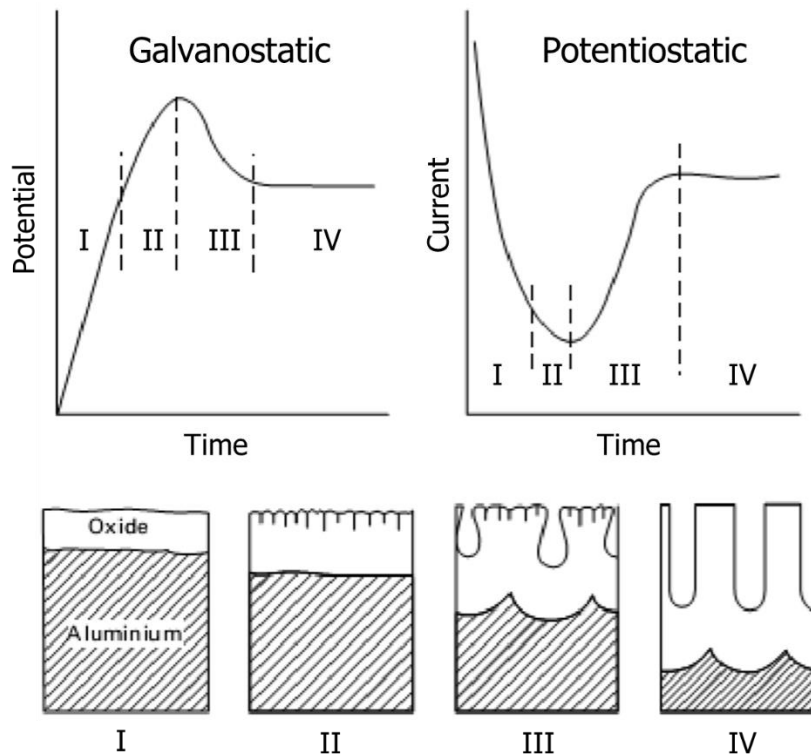
Figure 2. 13: Potential and current characteristics of the formation of a porous type anodic oxide. [43]

2.3.3. Effect of electrolyte viscosity

Figure 2.14a-e show the relations between PEG concentration and relative viscosity, pore diameter, barrier layer thickness and porous layer thickness as reported by Chen et al. [12] The barrier layer and the porous layer together make up a porous type anodic oxide. Apart from that, the same group also assumed an increase of the interpore distance as a result of the addition of a substance, PEG in this case, with a lower relative permittivity than water. The lower relative permittivity gives rise to an increase of the electric field strength involved in the anodising process, which in turn gives rise to an increase of the interpore distance. The decrease of the pore diameter is attributed to the protecting effect of PEG, which impedes the chemical dissolution process of the anodic oxide by the acidic environment. All of the above was confirmed by Stępniowski et al. [14] in 2014 for anodic aluminium oxides formed in oxalic acid containing different concentrations of glycerol. This group however also quantified the increase of the interpore distance as a function of the glycerol concentration. Furthermore Stępniowski et al. [14] give an explanation for the overall decrease in oxide layer thickness. The addition of organic electrolyte modulators, like glycerol, raises both the viscosity of the anodising electrolyte and the hydrodynamic radius of the ions involved. As a consequence the ionic mobility, u, is lowered according to Equation 2.21, which in turn lowers the current density, j, of the anodising process according to Equation 2.22. In these Equations z is the ionic charge, e is the elemental charge, η is the dynamic viscosity of the electrolyte, a is the hydrodynamic radius of the ion, α is the dissociation fraction, c_0 is the concentration, e is the elemental charge, z is the ionic charge coefficient and E is the electric field intensity. Both z and u are related to either the positive or the negative ions depending on the affix $+$ or $-$. [14] A lower current density directly translates into slower reaction kinetics and therefore a slower oxide growth due to the faradaic nature of the anodising process. [20,44–46]

20

Ionic mobility		

$$u = \frac{ze}{6\pi\eta a}$$

(2.21)

Current density

$$j = \alpha c_0 e(z_+ u_+ + z_- u_-)E$$

(2.22)

Another very important finding by Chen et al. [12] was the observed increase of the complex impedances for samples anodised in a polyethylene glycol containing electrolyte compared to the ones anodised in a fully aqueous environment. Besides they also measured a lower average transmembrane current at a constant transmembrane potential of 1V in an aluminium sulphate solution (0.2 M) for anodic oxides created in a polyethylene glycol containing electrolyte. Since the thickness of the barrier layer was found to be independent of the amount of polyethylene glycol used, the increase in complex impedances and the decrease in transmembrane current was attributed to a densification of the barrier layer when formed in a polyethylene glycol containing electrolyte. Besides the decreasing pore diameter was also assumed to be a contributing factor. Figure 2.14e shows the relation between the percentage of PEG and the thicknesses of both the barrier layer (BL) and the porous layer (PL), which are both part of a porous type anodic oxide. Figure 2.15 shows the Nyquist plot of the measured complex impedances (2.15a) and the transmembrane currents as a function of time (2.15b).
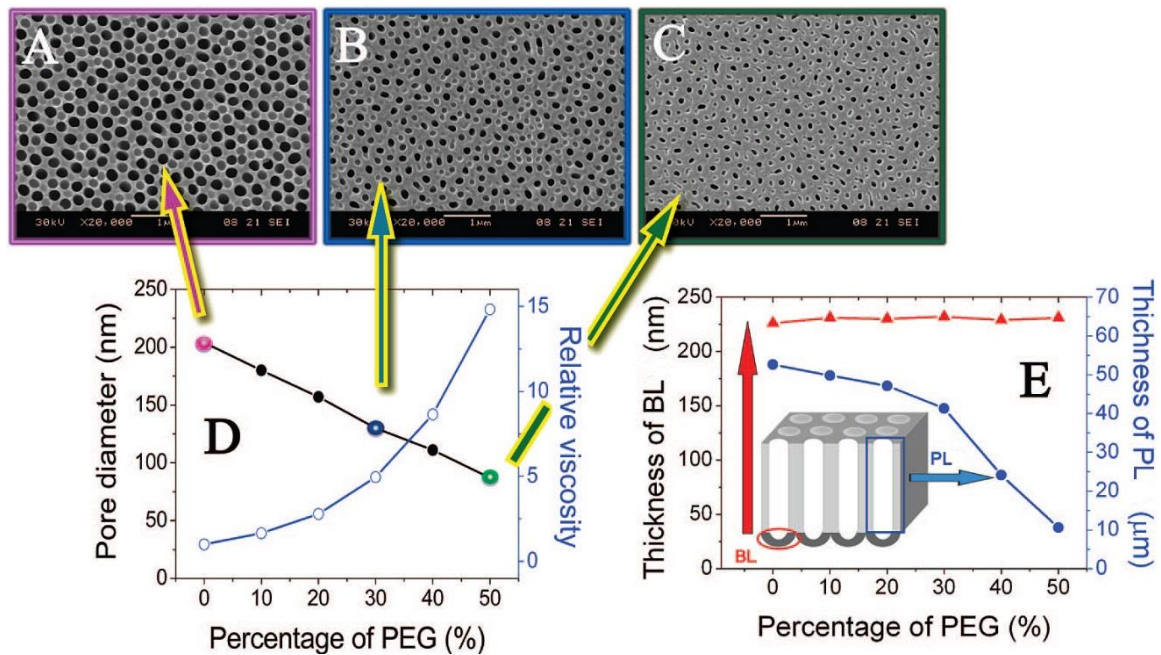
Figure 2. 14: Effect of viscosity on the pore diameter, barrier layer thickness (BL) and porous layer thickness (PL). [12]
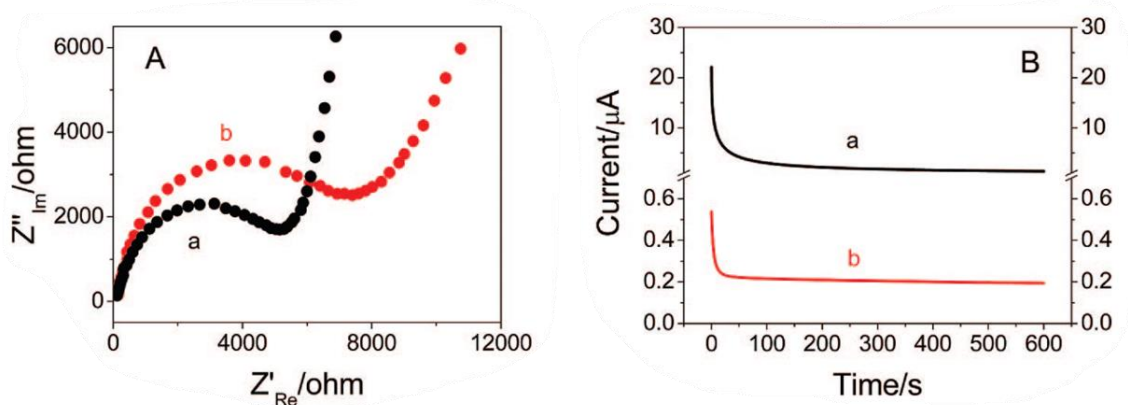
Figure 2. 15: Nyquist plot of complex impedance (A) and transmembrane current vs time (B). Small letter a represents AAO fabricated without PEG and small letter b AAO fabricated with PEG. [12]

Last but not least, as already mentioned in chapter 1, one work by Dumitriu et al. [16] is worth mentioning here as well since they was found a positive change in corrosion behaviour of titanium exposed to a Hank solution (8 g/L NaCl, 0.4 g/L KCl, 0.35 g/L NaHCO$_3$, 0.25 g/L NaH$_2$PO$_4$·H$_2$O, 0.06 g/L Na$_2$HPO$_4$·2H$_2$O, 0.19 g/L CaCl$_2$·2H$_2$O, 0.19 g/L MgCl$_2$, 0.06 g/L MgSO$_4$·7H$_2$O and 1 g/L glucose), if anodised with more viscous electrolyte. Figure 2.16 is showing both the Tafel plots and Nyquist plots of the titanium samples. The Tafel plots show a lower current density and the Nyquist plots higher complex impedances for samples anodised in partly non-aqueous electrolytes.
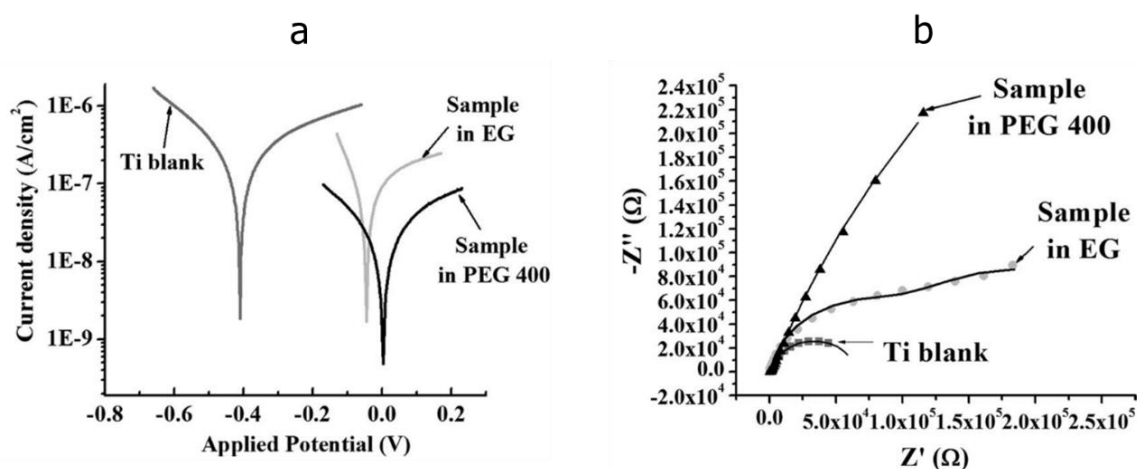
Figure 2. 16: Tafel plots (2.17a) and Nyquist plots (2.17b) of blank and anodised titanium exposed to a Hank solution in a three-electrode set-up. [16]

2.3.4. Effect of interelectrode distance

According to research by Michalska-Domańska et al. [15] in 2018 the interelectrode distance between the cathode and the anode does not have any significant effects on the typical morphological parameters (pore diameter, interpore distance, thickness etc.) of anodic oxides prepared on high purity aluminium in an oxalic acid electrolyte. The so called regularity ratio, which is related to the regularity of the pore arrangement and the uniformity of the pore shapes [47], was found to be changing for different interelectrode distances. Depending on the temperature and the voltage the regularity ratio was either increasing or decreasing with an increasing interelectrode

distance. On the other hand anodic oxides created on a titanium substrate in a fully non-aqueous electrolyte of diethylene glycol and hydrofluoric acid did show large changes in the pore diameter and interpore spacing when changing the interelectrode distance according to work by Yoriya. [48] In this particular case the pore diameters and interpore spacings were found to be increasing with a decreasing interelectrode distance.

2.4. Inhibitors

Inhibitors are either organic- or inorganic substances, which are able to prevent or minimize corrosion in an aggressive environment. [49] This section discusses the classification of inhibitors and the effect of adding inhibitors to the anodising bath.

2.4.1. Classification of inhibitors

The corrosion inhibitors could be divided into organic and inorganic inhibitors, see Figure 2.17. The inorganic ones typically decrease kinetics of either the anodic or the cathodic half-reaction of the corrosion process. [37,49] Anodic (inorganic) inhibitors generally react with the positively charged metal cations released at anodic sites forming an insoluble hydroxide film. This film is typically impermeable for metal cations. Cathodic (inorganic) inhibitors contain metal cations capable of reducing at cathodic sites and as a results forming a insoluble adherent film on top of these sites. This prohibits any further diffusion of reducible species at these sites. The organic inhibitors generally affect both the anodic and cathodic half-reactions by means of adsorption, forming a uniform layer on the surface of the metal isolating it from the aggressive environment. [37,49] Organic inhibitors are a form of mixed inhibitors because they affect both cathodic and anodic reactions. Inorganic mixed inhibitors also exist. For example the ones based on Cr^{6+}. [8,50]
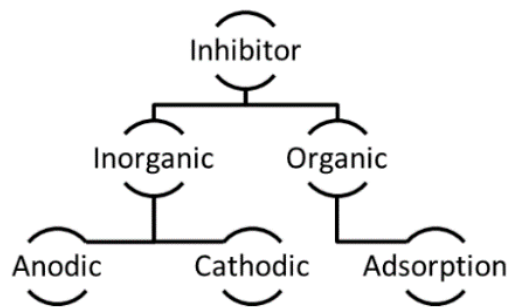
Figure 2. 17: Classification of corrosion inhibitors. [49]

2.4.2. Anodising with inhibitors

The traditional CAA procedure contains the highly toxic Cr^{6+} species in the form of (hydronated) negatively charged (di)chromate ions (CrO_4^{2-}, $Cr_2O_7^{2-}$, $HCrO_4^-$, $HCr_2O_7^-$). [51] Due to their negative charge these species are drawn towards the positively charged anode. Although the chromates are typically not incorporated in the oxide during the anodising process they do remain at the pore bases and walls as residuals. [44] It is believed that these residuals are one of the main reasons for the unsurpassed corrosion performance of CAA produced anodic oxides, since these species are able to form chromium hydroxide deposited on top of cathodic sites. Besides chromates adsorp onto aluminium oxides rather well creating an additional layer of protection against aggressive chloride ions which also slows down both anodic and cathodic reactions. [17,50] As an alternative

for Cr^{6+} based methods, various inhibitors have been tested in conjunction with anodising procedures like SAA and TSA. Inhibitors have been used before and after the anodising process itself in order to either incorporate the inhibitor in the oxide layer during the subsequent anodising process or to load the pores of the oxide layer after the anodising process with the inhibitor. Moreover, inhibitors have been used as an additional alloying element to the aluminium alloy itself to study the behaviour the anodic oxide growth on this new alloy during the anodising process. This resulted into incorporation of inhibitor species in the anodic oxide layer. Inhibitors have also been tested as additions to the anodising bath. [17] Adding inhibitors to the anodising bath does not necessarily result in incorporation of the inhibitor species into the anodic oxide layer, especially when the species are positively charged. The inhibitor species may also improve the corrosion performance of the substrate by changing the morphology of the anodic oxide formed. [17]

Rare earth salts have been tested as corrosion inhibitors in conjunction with sulfuric acid anodising treatments. Cerium-based ones are very promising as they are showing sublime corrosion performance improvements. [17] Other possible inhibitors have been tested as well with varying degrees of success, like for example molybdate and permanganate based species. [52] Research by Moutarlier et al. [18] in 2002 has indicated the promotion of oxide growth in the presence of Ce^{4+} species (in the form of 0.1 M $Ce(SO_4)_2$) and hindrance in the presence of molybdate ions (in the form of 0.1 M Na_2MoO_4), in a sulfuric acid electrolyte. The relatively large size of the molybdate ions was held responsible for the a decrease in ionic conductivity and therefore a decrease in anodic oxide thickness. It was assumed that the charge transfer in the acidic environment containing the cerium species was improved as well as the ionic transport near the anode, promoting the oxidation process. [18] Moreover Ce^{4+} species are known for their oxidising power, which means they are excellent film formers in that they readily oxidise various metals without applying a voltage or current density while reducing from the 4+ to the 3+ state. [18] Last but not least the many IMs present in alloys like AA2024-T3 are known for facilitating all kinds of parasitic reactions during the anodising process, like local dissolution and oxygen evolution. These type of reactions tend to create all kinds of flaws in the anodic oxide. The presence of cerium during the anodising process either from incorporation in the anodising electrolyte or from immersion in a cerium rich solution before anodising tends to attenuate these reactions and therefore improve the quality of the anodic oxide either by competing with the parasitic reaction or by oxidation of the IMs. A systematic study by Smith et al. in 1996 provided a corrosion benchmark of aluminium 2014-T6 anodised in sulfuric acid with different additives. The results were republished in the book chapter of Curioni et al. [17] in 2015, see Table 2.2. Compared to the other tested additives (all tested at 7.5 g/L) $Ce(SO_4)_2$ did improve the tested SAA treatment (150 g/L) the most. The time to pitting increased from 24 hours without $Ce(SO_4)_2$ to 116 hours with $Ce(SO_4)_2$.

When added to a sulfuric acid anodising electrolyte the positively charged cerium species (either in a 4+ or 3+ state) are not likely to be incorporated into the oxide layer or end up in the oxide pores as residuals, since they are not attracted to the positively charged anode (i.e. the substrate). This however is believed to be very different upon addition to a mixed acid electrolyte containing sulfuric acid and a carboxylic acid, like tartaric acid [20] or ethylenediaminetetraacetic acid (EDTA) [17]. It is believed that cerium ions are able to form negatively charged complexes with these type of acids, which allow them to be attracted to the positively charged substrate. [20] Besides that tartaric acid is known for its protective capabilities towards oxide dissolution during the anodising process. [20] The synergistic effect between carboxylic acids, like tartaric acid, and cerium species causes an intensified improvement of the corrosion performance of the anodic oxide.

24

[17,20,53] Last but not least it is important to note that Ce^{3+} does not provide the same film forming and parasitic reaction attenuating capabilities as Ce^{4+} when used as an addition to an anodising electrolyte. This is because it does not have the same oxidising power as reflected by their respective standard electrode potentials (+1.72 V vs SHE for Ce^{4+} against -2.34 V vs SHE for Ce^{3+} [54]). The corrosion inhibition provided by Ce^{3+} species relies on its capability to form cerium rich aluminium hydroxide layers on top of cathodic sites in corrosive conditions. [55] Therefore Ce^{3+} is a useful addition to a coating system.

Inhibitor	Film thickness (μm)	Time to pitting (h)	Assessment of attack at various times (h)			
			24	168	336	504
None	8.2	24	P1	P2,S2	P2,S3	P2,S3
Cerium (III) sulphate	10.6	72	N	P1,S1	P1,S1	P1,S2
Sodium metavanadate	0.6	12	P2	P2,S3	P2,S3	P2,S3
Cerium (IV) sulphate	4.2	>116	N	N	N	P2,S2
Zinc ions + metavanadate	2.5	24	P1	P2,S3	P2,S3	P2,S3
Sodium molybdate	0.8	8	P2,S3			
Molybdic acid	0.6	6	P2,S3			
Potassium permanganate	2.5	72	N	N	P1	P1,S2
Zinc thioglycollate	2.6	3	P2,S3			
Chromic acid anodizing	1.2	48	N,E1	P2,S3	P2,S3	P2,S3

Notes: N = no attack, E1 = slight attack at edges, S1 = some staining (<20% of surface), S2 = staining (20–80% of surface), S3 = staining (81–100% of surface), P1 = small pits (limited), P2 = small pits (extensive).

Table 2. 2: Corrosion performance of aluminium panels anodised in sulfuric acid with added corrosion inhibitor evaluated by neutral salt spray test. [17]

3. Materials and Methods

The substrates of AA2024-T3 (40x40x1.5) used in this work were supplied by Alu-Stock S.A. The chemical composition is shown in Table 3.1, as given by the supplier based on X-ray fluorescence results. This chapter describes the materials and methods used during this project.

	Al	Cu	Mg	Mn	Fe	Si	Zn	Ti	Cr	Other
Min	Rest	3.8	1.2	0.30	0	0	0	0	0	0
Max	Rest	4.9	1.8	0.90	0.50	0.50	0.25	0.15	0.10	0.15
Spec	Rest	4.3	1.4	0.43	0.10	0.06	0.08	0.04	-	-

Table 3. 1: Chemical composition of AA2024-T3 in wt%.

3.1 Experimental approach

In this work three main anodising procedures were studied: chromic acid anodising (CAA), sulfuric acid anodising (SAA) and tartaric sulfuric acid anodising (TSA). CAA, containing the highly toxic Cr^{6+} compounds, was merely used for the sake of comparison and therefore its electrolyte chemistry was kept constant. SAA and TSA were studied as Cr^{6+}-free alternatives. The chemistry of the electrolyte in these procedures was changed systematically, by adding different fractions of ethylene glycol. Besides $Ce(SO_4)_2$ was added to some electrolytes to see the effect of the addition of this inorganic corrosion inhibitor on the corrosion performance of AA2024-T3. Two different interelectrode distances were tested, large and small. In order to study these effects coupons of AA2024-T3 (40 x 40 x 1.5 mm) were chemically cleaned and etched using a three-step commercial cleaning procedure by Henkel AG & Co. KGaA (Henkel). Right after cleaning, the samples were anodised using one of the different procedures and analysed using different characterisation methods. Fresh samples were prepared for each characterisation method. The characterisation methods used in the present work are the following: LSV, EIS, Scanning Electron Microscopy (SEM) with Energy Dispersive X-Ray Spectroscopy (EDS) and Immersion tests. All experiments were conducted at room temperature conditions unless otherwise specified. Purified water from a Millipore Elix UV 10 water purification system was used throughout all experimental steps, including rinsing. Figure 3.1 shows a flow chart of the experimental approach used. Details of each of the building blocks of the flow chart could be found in the next sections.
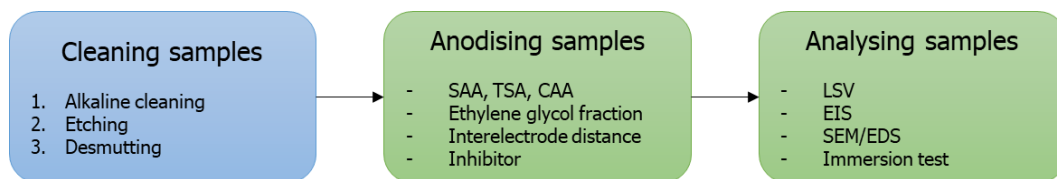
Figure 3. 1: Overview of experimental approach

3.2 Cleaning procedure

All test coupons of AA2024-T3 were cleaned and etched before anodising, according to a standardized procedure by Henkel. The three-step cleaning method consisted of an alkaline cleaning step, followed by an etching step and finished by a desmutting step, see Figure 3.2 for the cleaning set-up. After each step the samples were rinsed with purified water. All cleaning solutions were heated and stirred by IKA RET control-visc C8 heating and magnetic stirring plates. Commercial chemicals supplied by Henkel were used in each of the steps to prepare the appropriate cleaning solution according to the commercial procedure. All cleaning solutions were prepared in batches of 1 L and refreshed after every 30-35 samples. Due to the commercial character of these chemicals it is hard to tell the exact chemical composition since they are protected by a trade secret of Henkel. However the safety data sheet of all corresponding chemicals allow to get an approximate composition of all hazardous compounds found in these chemicals. Tables 3.2, 3.3 and 3.4 give the approximate compositions of the hazardous constituents of all used cleaning chemicals. Besides, the pH of each cleaning solution was measured using a Schott CG 842 Laboratory pH meter with WTW SenTix 81 pH electrode.

BONDERITE C-AK 4215 NC-LT AERO

Hazardous component	Formula	CAS	wt%
Borax	$Na_2B_4O_7$	1330-43-4	30 - 40
Pentasodium triphosphate	$Na_5P_3O_{10}$	7758-29-4	20 - 30
Sodium nitrate	$NaNO_3$	7631-99-4	5 - 10
Diethylene glycol monobutyl ether	$C_8H_{18}O_3$	112-34-5	1 - 5
Disodium hexafluorosilicate	Na_2SiF_6	16893-85-9	1 - 5

Table 3. 2: Information on chemical composition of alkaline cleaner.

BONDERITE C-AK ALUM ETCH 2 AERO

Hazardous component	Formula	CAS	wt%
Sodium hydroxide	NaOH	1310-73-2	60 - 100
Trisodium orthophosphate	Na_3PO_4	7601-54-9	10 - 30
Surfactant(s)	-	Proprietary	1 - 5

Table 3. 3: Information on chemical composition of etching agent.

BONDERITE C-IC SMUTGO NC AERO

Hazardous component	Formula	CAS	wt%
Ferric sulphate	$Fe_2(SO_4)_3$	10028-22-5	30 - 60
Nitric acid	HNO_3	7697-37-2	5 - 10
Sodium hydrogendifluoride	$NaHF_2$	1333-83-1	1 - 5
Sulfuric acid	H_2SO_4	7664-93-9	0.1 - 1

Table 3. 4: Information on chemical composition of desmutting agent.

3.2.1. Cleaning step 1: alkaline cleaning

All samples were attached to a polypropylene holder before immersion to make sure the sample did not interfere with the magnetic stir bar on the bottom of the beaker containing the cleaning

solution since agitation during dipping was prescribed. The first step of the cleaning procedure was used to remove dust, dirt and residual grease from manufacturing and transportation of the alloy to assure all subsequent steps work evenly across the substrate surface. [56] This step is called the alkaline cleaning, since cleaning took place in a beaker containing a slightly alkaline solution (pH 8.8). The cleaning recipe of this cleaning step is shown below.

Recipe
Bath chemistry: 50 g/L BONDERITE C-AK 4215 NC-LT AERO
Bath volume: 1 L
Measured pH: 8.8 at 58.1 °C
Temperature: 60 °C
Agitation: 180 min^{-1}
Dipping time: 10 min

3.2.2. Cleaning step 2: etching

Chemical etching was applied in the second step of the cleaning procedure using an alkaline solution (pH 12.6). Etching removes the native oxide from the sample as well as a thin layer of underlaying material creating a relatively smooth surface fit for anodising. [57–61] The upper near-surface layer of as-received aluminium alloys is often deformed due to the heavy shear deformations occurring during the manufacturing process. It has been reported that these deformations promote the formation of secondary IMs in the near-surface region during subsequent heat treatments. This results in a near-surface region containing a higher density of fine IMs and lower solid solution levels compared to the underlaying bulk material, which results in preferential attack during corrosion. Etching removes this layer and smoothens the surface. The recipe of this cleaning step is shown below. [57–61]

Recipe
Bath chemistry: 38 g/L BONDERITE C-AK ALUM ETCH 2 AERO
Bath volume: 1 L
Measured pH: 12.6 at 39.0 °C
Temperature: 40 °C
Agitation: 180 min^{-1} (no agitation during dipping, only in between samples)
Dipping time: 2 min

3.2.3. Cleaning step 3: desmutting

Desmutting, also called deoxidizing, was the last step in the cleaning process. It removed the so called smut layer which typically forms on aluminium alloys during alkaline etching. [62,63] The layer typically consists of a powdery dark-coloured substance which consists of insoluble oxides and IMs. For AA2024-T3 this means that the smut layer mainly consists of insoluble copper oxides. [62,63] The smut layer is typically removed by dipping the sample into an acidic cleaning solution. [59] The recipe and the used equipment of this cleaning step is shown below.

Recipe

Bath chemistry:	19 vol% BONDERITE C-IC SMUTGO NC AERO
Bath volume:	1 L
Measured pH:	0.55 at 20.7 °C
Temperature:	room temperature
Agitation:	180 min^{-1} (no agitation during dipping, only in between samples)
Dipping time:	5 min
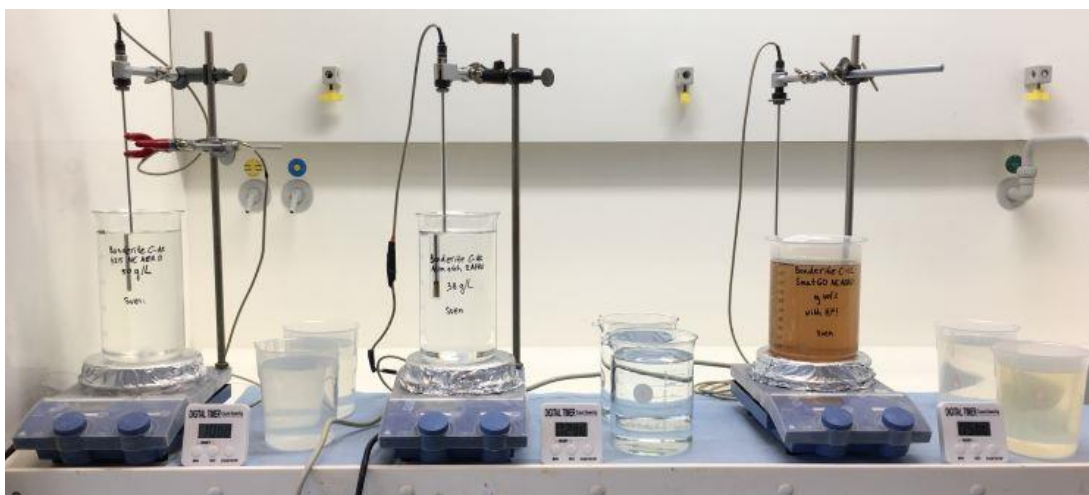
Figure 3. 2: All cleaning solutions. Step 1 left, step 2 middle, step 3 right. Rinsing baths after each step.

3.3 Anodising procedures

As already discussed in section 3.1 this work focussed on three main anodising procedures, namely: chromic acid anodising (CAA), sulfuric acid anodising (SAA) and tartaric sulfuric acid anodising (TSA). All procedures were applied as potentiostatic anodising procedures using a two-electrode cell. CAA was used as the baseline surface treatment in order to make a comparison, while SAA and TSA procedures were studied as the Cr^{6+} free alternatives by changing their anodising chemistry and interelectrode distance in a systematic manner. The chemistry of the electrolyte of the SAA and TAA procedures was altered systematically, by adding different fractions of ethylene glycol (Merck reagent grade ethylene glycol ≥99 wt%). Besides $Ce(SO_4)_2$ (Sigma-Aldrich Cerium(IV)sulfate) was added to some electrolytes to see the effect of the addition of this inorganic corrosion inhibitor. Acid concentrations were kept constant in each of the three main procedures. Sulfuric acid was supplied by Honeywell (Honeywell Fluka Puriss p.g.a. sulfuric acid 95 - 97 wt%) and tartaric acid was supplied by Sigma-Aldrich (Sigma-Aldrich L-(+)-tartaric acid ≥99.7 wt%). Two anodising geometries were tested, consisting of a large and a small interelectrode distance (55 mm and 5 mm). Apart from changing the anodising electrolyte chemistry (SAA and TSA) and interelectrode distance (CAA, SAA and TSA), other anodising parameters like, voltage, temperature, anodising time and agitation speed, were kept constant. Figure 3.3 shows a flow chart depicting all tested anodising electrolyte chemistries and interelectrode distances.
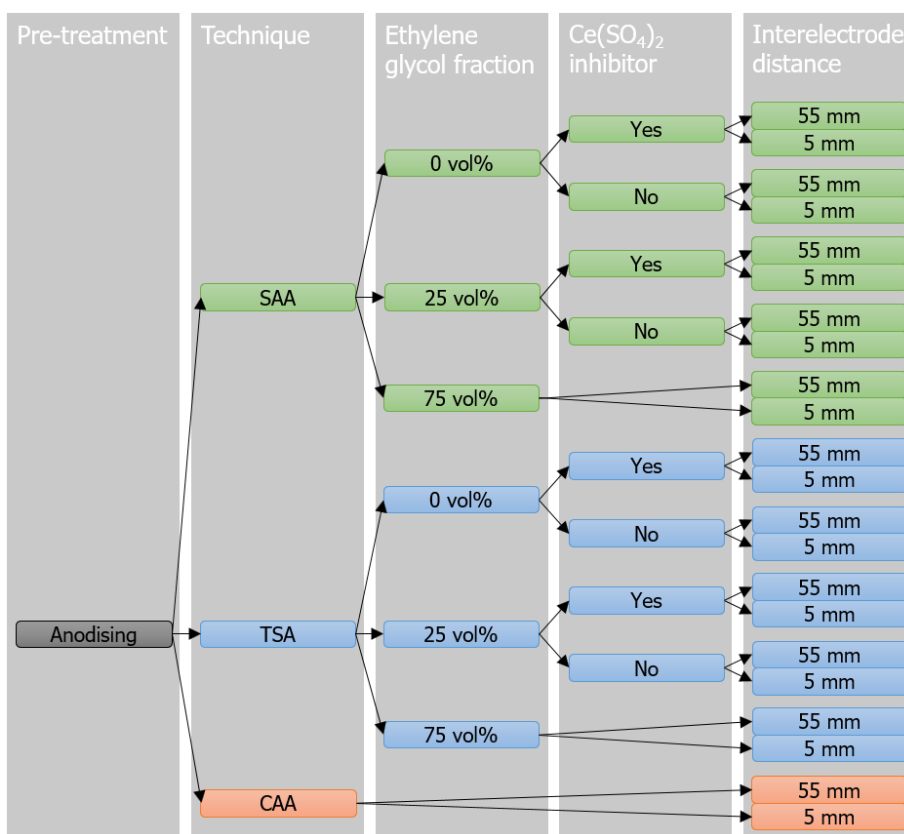
Figure 3. 3: Flow chart depicting all tested anodising electrolyte chemistries and geometries.

All samples were anodised in a 800 mL double walled glass tempering beaker, connected to a Huber MPC-E-K6 thermoregulation system pumping around coolant for temperature control. The anodising voltage was applied by a Delta Elektronika SM 120-25 D power supply and controlled by Delta Elektronika Power Supply Control I - 0.0 software. A custom designed electrode holder with alligator clips was used to make sure the interelectrode distance at either the large (55 mm) or the small (5 mm) distance, besides the and immersion depth was fixed too. Figure 3.4 shows the anodising set-up for both interelectrode distances. A platinum mesh was used as the cathode and agitation during anodising was established by a magnetic stir bar regulated by a IKA RET control-visc C8 magnetic stirring plate. pH of each electrolyte was measured with a Schott CG 842 Laboratory pH meter with WTW SenTix 81 pH electrode.
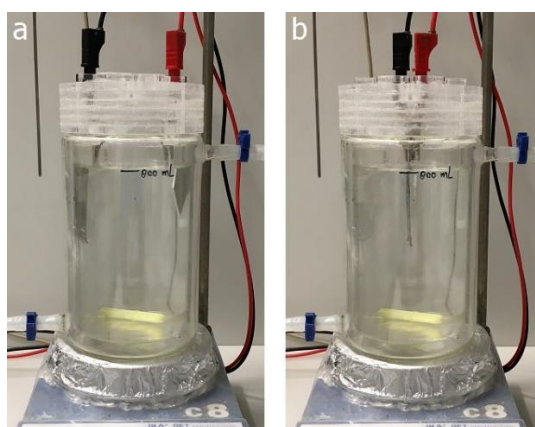
Figure 3. 4: Large - (3.3a) and small (3.3b) interelectrode distance anodising set-ups.

3.3.1. Sulfuric acid anodising (SAA)

For the SAA procedures a 15 wt% sulfuric acid based electrolyte was used, converted into 1.69 M based on aqueous electrolyte conditions. This molarity was used for both aqueous and partially non-aqueous electrolytes. Furthermore an anodising voltage of 18 V (potentiostatic anodising without ramp), an anodising time 25 minutes and an electrolyte temperature 25 °C were used. These parameters were constant in this present work.

Recipes

Acid concentration:	1.69 M sulfuric acid
Solvent:	0 vol% ethylene glycol (= 100 vol% purified water)
	25 vol% ethylene glycol
	75 vol% ethylene glycol
Inhibitor:	0.003 M $Ce(SO_4)_2$ or no inhibitor
Volume:	800 mL
Measured pH:	-0.25 at 25.3 °C (for 0 vol% ethylene glycol electrolyte)
	-0.32 at 25.3 °C (for 25 vol% ethylene glycol electrolyte)
	-0.53 at 25.4 °C (for 75 vol% ethylene glycol electrolyte)
Temperature:	25 °C
Agitation:	180 min^{-1}
Anodising time:	25 min
Anodising voltage:	18 V

3.3.2. Tartaric sulfuric acid anodising (TSA)

For the TSA procedure a mixed acid electrolyte containing 40 g/L of sulfuric acid and 75 g/L of tartaric acid was used and converted into 0.41 M and 0.50 M solutions respectively. These molarities were used for all TSA electrolytes. Furthermore, an anodising voltage of 14 V (potentiostatic anodising without ramp), an anodising time of 25 minutes and an electrolyte temperature of 37 °C were used. These parameters were kept constant in this present work.

Recipes

Acid concentration:	0.41 M sulfuric acid + 0.50 M tartaric acid
Solvent:	0 vol% ethylene glycol (= 100 vol% purified water)
	25 vol% ethylene glycol
	75 vol% ethylene glycol
Inhibitor:	0.003 M $Ce(SO_4)_2$ or no inhibitor
Volume:	800 mL
Measured pH:	0.39 at 36.2 °C (for 0 vol% ethylene glycol electrolyte)
	0.36 at 36.6 °C (for 25 vol% ethylene glycol electrolyte)
	0.20 at 36.2 °C (for 75 vol% ethylene glycol electrolyte)
Temperature:	25 °C
Agitation:	180 min^{-1}
Anodising time:	25 min
Anodising voltage:	14 V

3.3.3. Chromic acid anodising (CAA)

For the CAA procedure a common 0.3 M chromic acid electrolyte was used based on the literature. [64,65] For comparative reasons it was decided to take an anodising voltage in the same

range as the SAA and TSA procedures. Since those procedures operated at 18 V and 14 V respectively, a voltage of 16 V was chosen. The electrolyte temperature was set at 25 °C and the anodising time at 25 minutes. The chromic acid solution was prepared by mixing chromium trioxide powder (Sigma-Aldrich ACS reagent chromium(VI)oxide ≥98.0 wt%) with purified water.

Recipes

Acid concentration:	0.3 M chromic acid
Solvent:	100 vol% purified water
Inhibitor:	No inhibitor
Volume:	800 mL
Measured pH:	0.66 at 25.3 °C
Temperature:	25 °C
Agitation:	180 min^{-1}
Anodising time:	25 min
Anodising voltage:	16 V

3.4 Characterisation methods

Four different characterisation methods were used in this work to characterise the samples: LSV, EIS, SEM with EDS and Immersion tests. All samples were characterised with LSV, EIS and SEM/EDS but only selected were tested with an immersion test.

3.4.1. Linear Sweep Voltammetry

LSV was used to measure the polarisation curves of each sample using a Biologic VSP-300 potentiostat along with EC-lab V11.20 software. Samples were mounted inside a custom 80 mL three-electrode cell, consisting of a stainless steel counter electrode and silver/silver chloride reference electrode filled with a saturated potassium chloride solution (Hydromet RL-100 Ag/AgCl/Sat. KCl), see Figure 3.5. The exposed area of the sample, acting as the working electrode, was 2.71 cm^2. For each full polarisation curve two identical samples were prepared. One for measuring the anodic branch and one for measuring the cathodic branch, in order to make sure no alterations of the anodised layer took place due to polarisation. Each polarisation curve was measured three times to check for repeatability of the results. All measurements were conducted in 0.1 M sodium chloride solution (Merck EMSURE sodium chloride).

The collected data was analysed with EC-lab V11.20 software, in order to determine the corrosion current density (i_{corr}) via the extrapolation method and the polarisation resistance (R_p) via the linear polarisation resistance method. Tafel slopes were determined over a range between +50 and +150 mV versus the equilibrium potential for the anodic branch and between -50 and -150 mV versus the equilibrium potential for the cathodic branch, after which they were extrapolated to find i_{corr} at the intersection of the two lines. This however was not feasible for all polarisation curves due to very high activity in the anodic branch. The Tafel slopes in these plots were determined over a much narrower range much closer to the equilibrium potential to avoid fitting mass transfer related polarisation. The range for these plots was chosen between approximately +20 and +60 mV versus the equilibrium potential. R_p was determined over a linear section of the polarisation curves between -10 and +10 mV versus the equilibrium potential using the measured anodic branches.

Recipe

Electrolyte:	0.1 M sodium chloride
Cell volume:	80 mL
Temperature:	Room temperature
OCP stabilisation time:	4 h
Scan range anodic:	-0.030 V vs OCP to 0.500 V vs OCP
Scan range cathodic:	+0.030 V vs OCP to -0.500 V vs OCP
Scan rate:	0.1 mV/s
Exposed area:	2.71 cm^2

3.4.2. Electrochemical Impedance Spectroscopy

In order to check the corrosion behaviour over time, EIS measurements were carried out, over the course of 48 hours, using a Biologic VSP-300 potentiostat with EC-lab V11.20 software. Samples were mounted inside a custom 80 mL three electrode cell consisting of a stainless steel counter electrode and silver/silver chloride reference electrode filled with a saturated potassium chloride solution (Hydromet RL-100 Ag/AgCl/Sat. KCl). The first EIS measurement was conducted after 4 hours of immersion time, the second one after 8 hours, the third one after 12 hours, the fourth one after 24 hours, the fifth one after 36 hours and the sixth one after 48 hours. A sinusoidal perturbation signal with an amplitude of 10 mV was used to excite the electrochemical cell in the frequency range from 100 kHz to 10 mHz. Each decade was split up into 10 data points per decade and each data point was determined as the average over two consecutive measurements. A resting time of 0.1 period was used after each measured frequency. Each EIS measurement took 17:09 minutes to complete, as determined by dummy cell (EC-lab software indicated approximately 17:30 minutes). All measurements were conducted in 0.1 M sodium chloride solution (Merck EMSURE sodium chloride). The absolute value of the impedance (|Z|) at 0.01 Hz was used to as a benchmark and plotted versus the immersion time to evaluate the corrosion behaviour over time.

Recipe

Electrolyte:	0.1 M sodium chloride
Cell volume:	80 mL
Temperature:	Room temperature
OCP stabilisation times:	4 h; 8 h; 12 h; 24 h; 36 h; 48 h
Amplitude of signal:	10 mV
Frequency range:	100 kHz to 10 mHz
Resting time:	0.1 period
Measurements per datapoint:	2
Points per decade:	10
EIS measurement time:	17:09 min
Exposed area:	2.71 cm^2

3.4.3. Scanning Electron Microscopy with Energy Dispersive X-Ray Spectroscopy

A Jeol JSM-IT100 Scanning Electron Microscope (SEM) was used to make some overview images and measure the chemical composition of the sample surfaces using the Energy Dispersive X-Ray Spectroscopy (EDS) functionality. Due to the electrical insulating properties of aluminium oxide, the samples required a low vacuum in order to get rid of the charging phenomena which would occur in high vacuum conditions. [62,66] Since the Jeol system could only detect

backscattered electrons in low vacuum mode, only backscatter images were taken and the EDS spectra were measured.

Recipe

Acceleration voltage:	15 kV
Working distance:	10 mm
Probe current:	50
Pressure:	30 Pa
Imaging mode:	Backscatter electron imaging in compositional mode (BEC)
Chemical analysis:	Energy Dispersive X-Ray Spectroscopy (EDS)

3.4.4. Immersion testing

As a complementary technique to the electrochemical test a simple visual corrosion tests in the form of an immersion test was added. Samples were mounted in the same custom 80 mL three electrode cell consisting of a stainless steel counter electrode and silver/silver chloride reference electrode filled with a saturated potassium chloride solution (Hydromet RL-100 Ag/AgCl/Sat. KCl). After 48 hours the samples were removed from the cells, rinsed with purified water and dried with compressed air. Micrographs of the samples were taken before and after 48 hours of exposure to the saline solution at 100x magnification using a Keyence VHX-5000 Digital Microscope. The open circuit potential was recorded during immersion using a Biologic VSP-300 potentiostat along with EC-lab V11.20 software. A 0.1 M sodium chloride solution was used as an electrolyte (Merck EMSURE sodium chloride)

Recipe

Solution:	0.1 M sodium chloride
Immersion time:	48 hours

Figure 3. 5: Custom three-electrode electrochemical cell.

4. Results and discussion

This chapter dives into the results of this work. Before commencing into any further discussion about the results of the characterisation methods used, some important preliminary observations are reviewed. Right after the preliminary observations the results of the anodising process are examined, in the form of current density versus time curves. The remainder of this section discusses the results of all experimental methods used in the following order: LSV, EIS, SEM with EDS and last but not least the immersion tests.

4.1. Preliminary observations

The preliminary observations are divided into preliminary OCP measurements, observed inhibitor electrolyte interactions and SEM/EDS observations of all cleaning steps.

4.1.1. Preliminary open circuit potential measurements

Before starting any further electrochemical tests the OCP of the AA2024-T3 alloy before and after anodising were recorded over the course of 24 hours to check the stationarity of the system. Both the unaltered SAA and TSA procedures were tested. In this context the non-anodised alloy is referred to as bare. All bare specimens were cleaned using the three-step commercial cleaning procedure described in chapter 3 before any further measurements were conducted. Stationarity of the OCP is very important when doing electrochemical measurements, especially when measuring the EIS spectrum since small amplitude (10 mV) sinusoidal perturbation signals are used to excite the electrochemical system. Changes in OCP during such a measurement may create a lot of noise and alter the actual measurement. [67,68]

Figure 4.1 shows the preliminary open circuit potentials recorded, 4.1a gives an overview of the evolution of OCP over the course of 24 hours, while 4.1b shows a more detailed view around the chosen initial OCP time of 4 hours. The first thing to notice is the fact that stationarity is hard to find for all curves. During the first 2 hours a large drop in the potential occurs due to initial breakdown of the oxide layer created during the anodising process (blue and green curves). After this period either a slow or a fast oxide recovery takes place after which the potential becomes metastable. Oscillations in the potential are typically found in pitting sensitive materials like aluminium alloys and stainless steels exposed to sodium chloride solutions and are related to the initiation, repassivation and growth of corrosion pits. [69–71] One could argue an OCP stabilisation time of 3 hours should be sufficient when looking at the graphs in Figure 4.1 however due to the relatively large oscillations between 3 and 3,5 hours of immersion time seen on the SAA anodised sample an initial OCP stabilisation time of 4 hours was chosen for all consecutive electrochemical measurements.
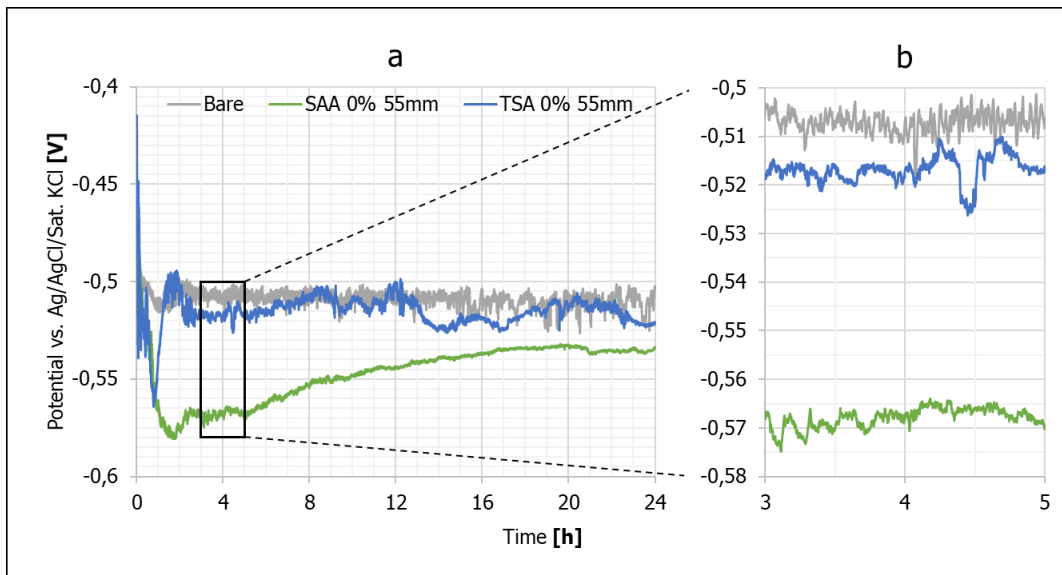
Figure 4. 1: Open circuit potential of bare AA2024-T3 (cleaned), SAA anodised and TSA anodised.

4.1.2. Observed inhibitor electrolyte interactions

Interesting observations were made concerning interactions between $Ce(SO_4)_2$ and the anodising electrolytes. Adding $Ce(SO_4)_2$ to a sulfuric acid electrolyte resulted in a transparent yellow solution, since solvated Ce^{4+} ions are known for their yellow colour in aqueous solutions. [72] On the other hand, mixing tartaric acid with a dilute sulfuric acid solution (containing $Ce(SO_4)_2$) first intensified its yellow colour towards orange after which the colour slowly disappeared in a matter of minutes. Similarly the yellow colour of a sulfuric acid electrolyte containing both ethylene glycol and $Ce(SO_4)_2$ disappeared. For this particular electrolyte no colour intensification was observed and it took a number of hours for the colour to vanish.

The same interaction between tartaric acid and $Ce(SO_4)_2$ was observed by Datt et al. [73] in a nitric acid environment. The mechanism shown in Figure 4.2 was proposed for a generalized α-hydroxy acid (HA). Before the addition of the HA to nitric acid, containing Ce^{4+} species, several cerium-nitrate complexes may form, represented by $Ce(NO_3)_n^{(4-n)}$. [73] Upon addition of the HA new complexes are formed between the Ce^{4+} species and the HA, by releasing some nitrate ions, see Figure 4.2a. This step is held responsible for the fast deepening of the colour of the solution from yellow to orange. After complexation with the HA, Ce^{4+} is reduced to Ce^{3+} and the HA acid is converted into an intermediate radical and carbon dioxide (4.2b and 4.2d). The radical molecule further oxidises with left over Ce^{4+} to form a stable molecule. The stoichiometric Equation for the overall reaction between Ce^{4+} and tartaric acid is shown in Figure 4.2d. Tartaric acid is converted into formic acid and carbon dioxide when added to an acidic solution containing Ce^{4+} species. Since the nitrate ions are not participating in the overall reaction, similar behaviour between Ce^{4+} species and tartaric acid is expected for the used TSA electrolyte with added $Ce(SO_4)_2$ in this present work. The reduction of Ce^{4+} species is responsible for the colour change from orange to colourless.

38

$$a \quad Ce(NO_3)_n{}^{(4-n)} + HA \underset{K}{\rightleftharpoons} \left[\begin{array}{c} \text{(structure)} \end{array} \right]^{(5-n)} + NO_3{}^-$$

$$b \quad \left[\begin{array}{c} \text{(structure)} \end{array} \right]^{(5-n)} + H^+ \xrightarrow{k} R^1R^2\dot{C}OH + Ce(III) + 2H^+$$

$$c \quad (m-1)Ce^{IV} + R^1R^2\dot{C}OH \xrightarrow{fast} \begin{array}{c} R^1 \\ \diagdown \\ C=O \\ \diagup \\ R^2 \end{array} + (m-1)Ce^{III} + (m-1)H^+$$

$$d \quad HO_2C.CHOHCHOH.CO_2H + 2H_2O + 8Ce^{IV} \\ \rightarrow HCO_2H + 3CO_2 + 8Ce^{III} + 8H^+$$

Figure 4. 2: Mechanism of oxidation of α-hydroxy acids by Ce^{4+} in nitric acid. [73]

Adding $Ce(SO_4)_2$ to an SAA electrolyte, containing a fraction of ethylene glycol, at first seemed to have a similar effect as adding it to the 100% aqueous SAA electrolyte. However, it was observed that after a few hours the yellow colour faded. In fact, 12 hours after preparation the previously yellow electrolyte changed into a colourless one (Figure 4.3). The explanation for the observed phenomena was found in the field of organic synthesis in which Ce^{4+} compounds are used in conjunction with an organic reductant to form a redox pair which creates the free radicals needed to initiate a free radical polymerisation reaction. All kinds of ketones, amines, carboxylic acids or alcohols may act as the organic reductant. This includes vicinal- and polyhydric alcohols like ethylene glycol. [74,75]

Figure 4. 3: SAA electrolyte having 0 vol% and 25 vol% ethylene glycol right after preparation and after 12 hours. All electrolytes contain 0.003 M $Ce(SO_4)_2$.

Figure 4.4 shows the reaction mechanism of Ce^{4+} with ethylene glycol. It involves the formation of a monodentate complex between Ce^{4+} and ethylene glycol which is succeeded by a one-electron cleavage step. This step transforms Ce^{4+} into Ce^{3+} and creates an intermediate hydroxymethyl radical and a formaldehyde molecule. Left over Ce^{4+} may oxidize the radicals which gives another formaldehyde molecule, releases a proton and again reduces Ce^{4+} into Ce^{3+}. The reduction of cerium from its 4+ to its 3+ state explains the change in colour, since solvated Ce^{3+} ions are known to be colourless. [72]
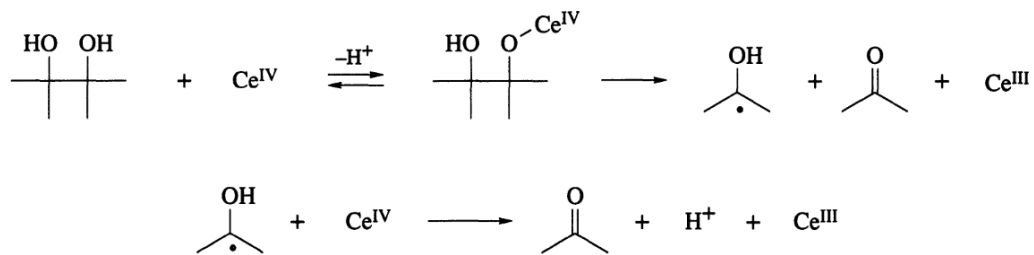
Figure 4. 4: Reaction mechanism of Ce^{4+} with ethylene glycol. [74]

4.1.3. SEM/EDS observations of all cleaning steps

The cleaning procedure used, as described in chapter 3, consisted of three steps: alkaline cleaning, chemical etching and desmutting. After each of these steps micrographs were taken in compositional backscatter mode using SEM. The EDS spectra were measured as well to compare the compositional differences of the samples after each cleaning step. Figure 4.5 shows all images of the sample surface before and after each cleaning step. No serious changes are observed between Figure 4.5a (as-received condition) and Figure 4.5b (condition after cleaning step 1), since this step should only remove dirt and grease remnants from the as-received alloy. The surface conditions after cleaning step 2, which etches the surface, are shown in Figure 4.5c. Loosely adherent smut flakes are clearly visible. The removal of the smut layer was achieved by the last cleaning step, confirmed by Figure 4.5d. The etching process did not uniformly attack the surface as is evident from the clearly visible larger and smaller pits in Figure 4.5d. This is typically observed on aluminium alloys after etching in alkaline conditions. [59,62] Last but not least, it is important to note that in chapter 3 it was explained that aluminium alloy samples are typically etched in order to remove the native oxide layer and to remove the near-surface region. This region contains a higher density of fine IMs due to heavy shear deformations occurring during the manufacturing process prior to further heat treatments. [57–61] When comparing Figure 4.5b to 4.5d it is clearly visible that before etching the sample surface contains a lot of small IMs, which could be identified as bright white spots. After etching and desmutting the vast majority of the small IMs are gone.
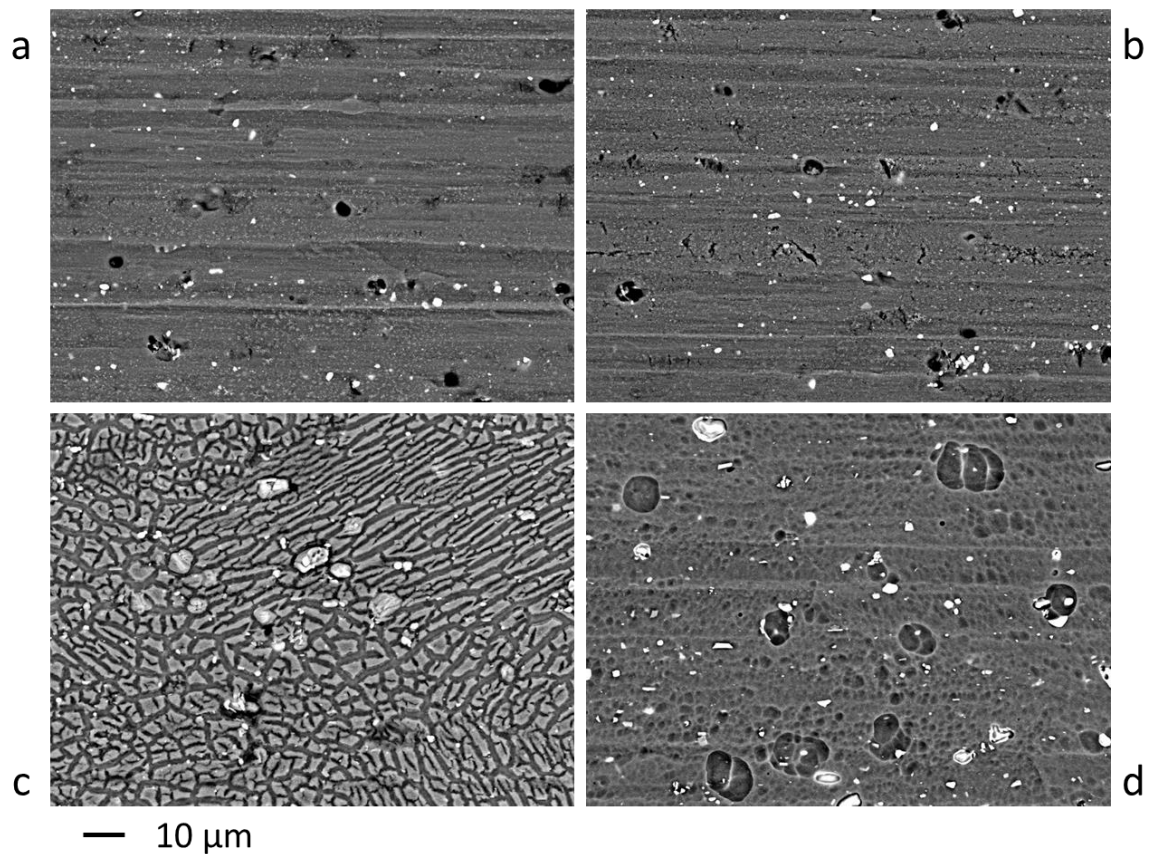
Figure 4. 5: Backscatter images (BEC) of AA2024-T3 substrates at 1000x after each cleaning step. a: as-received condition, b: after alkaline cleaning, c: after etching, d: after desmutting.

The EDS spectra in Figure 4.6 show five elements where detected in general, namely: aluminium, copper, magnesium, oxygen and carbon. The first three elements are related to the alloying elements of AA2024-T3. Oxygen is related to the presence of oxides, while carbon is related to the presence of contamination from the manufacturing process and transport. When looking at the EDS spectrum of the as-received (As-rec.) alloy it is evident there is carbon present because of the contaminants still present. Comparing this to the spectrum after the first cleaning step (S1) the carbon peak has disappeared, implying the sample has been decontaminated. Both spectra before and after cleaning step 1 show the presence of oxygen which is related to the native oxide still being present. Right after cleaning step 2 (S1+2) a large mass fraction of oxygen was detected caused by the smut layer, since it consists of insoluble oxides of alloying elements. For AA2024-T3 the smut layer mainly consists out of copper oxides. [62,63] Remarkably a significant fraction of carbon was detected again. Due to the composition of the etching agent, see Table 3.3, this might be caused by left over surfactants trapped in the smut layer. Last but not least the spectrum after cleaning step 3 (S1+2+3) shows the removal of the large oxygen and carbon peak, implying the removal of the smut layer.
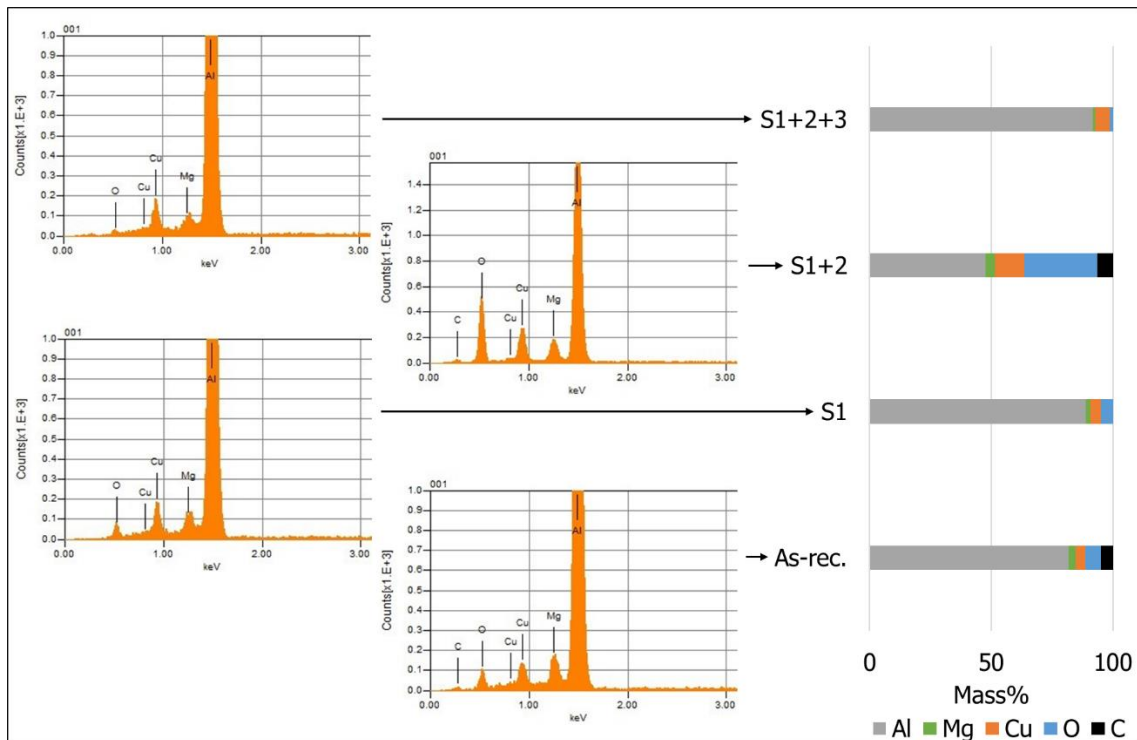
Figure 4. 6: EDS spectra + mass fractions of detected elements of samples after each cleaning step. As-rec. = as-received AA2024-T3. S1 = AA2024-T3 after cleaning step 1. S1+S2 = AA2024-T3 after cleaning step 2. S1+S2+S3 = AA2024-T3 after cleaning step 3.

4.2. Anodising

Figure 4.7 shows the as recorded current density response of each anodising cycle. Figures 4.7a and 4.7b show the full graph, while 4.7c and 4.7d show the first 100 seconds of the anodising procedures to highlight the transient phenomena observed. Each similarly coloured group of curves is provided with a label indicating the a group of similar anodising procedures. For example the label "SAA 0% (all)", in Figure 4.7a, indicates that all reddish coloured curves belong to the anodising cycles according to the sulfuric acid anodising procedure containing 0 vol% of ethylene glycol. The affix "(all)" refers to all variants of this procedure, so with and without $Ce(SO_4)_2$ and both anodising geometries. See Figure 3.3 for all anodising procedures used in this work.

The first thing to notice is the relation between the ethylene glycol volume fraction and the current density. The higher the ethylene glycol fraction, the lower the current density. This applies to both SAA and TSA procedures and is in correspondence with previous findings by Chen et al. [12] and by Stępniowski et al. [14], in which a similar trend was found between the volume fraction of an organic electrolyte modulator (polyethylene glycol and glycerol respectively) and the current density. Essentially the addition of organic compounds, like ethylene glycol, raises both the viscosity of the electrolyte and the hydrodynamic radius of the ions involved in the anodising process. [76,77] Both of these parameters have an effect on the ionic mobility according to Equation 2.21 in chapter 2. From this Equation it is evident that an increase in viscosity and/or hydrodynamic radius of the ions involved lead to a decrease in ionic mobility which is directly proportional to the current density of an electrochemical process according to Equation 2.22 also in chapter 2. [14] The recorded drop in current density with increasing ethylene glycol fractions is therefore justified. The difference in current density between SAA and TSA anodising procedures is the result of a difference in

42

hydrodynamic radius, viscosity and anodising voltage (14 V compared to 18 V). These differences have a direct effect on the electric field intensity. Apart from that the used concentration of sulfuric acid (0.41 M) + tartaric acid (0.50 M) in the TSA electrolyte together added up to a combined acid concentration of 0.91 M, which is lower than the sulfuric acid concentration of 1.69 M in the SAA electrolyte. On top of that tartaric acid typically does not fully dissociate in contrast to sulfuric acid (pK$_{a1}$ of 2.89 vs pK$_{a1}$ of -3.00 respectively [78]).   Therefore, the concentration of H$^+$ ions will be lower in the TSA electrolyte. The low current density of the CAA procedure is mainly caused by the low acid concentration (0.3 M) and the anodising voltage (16 V).
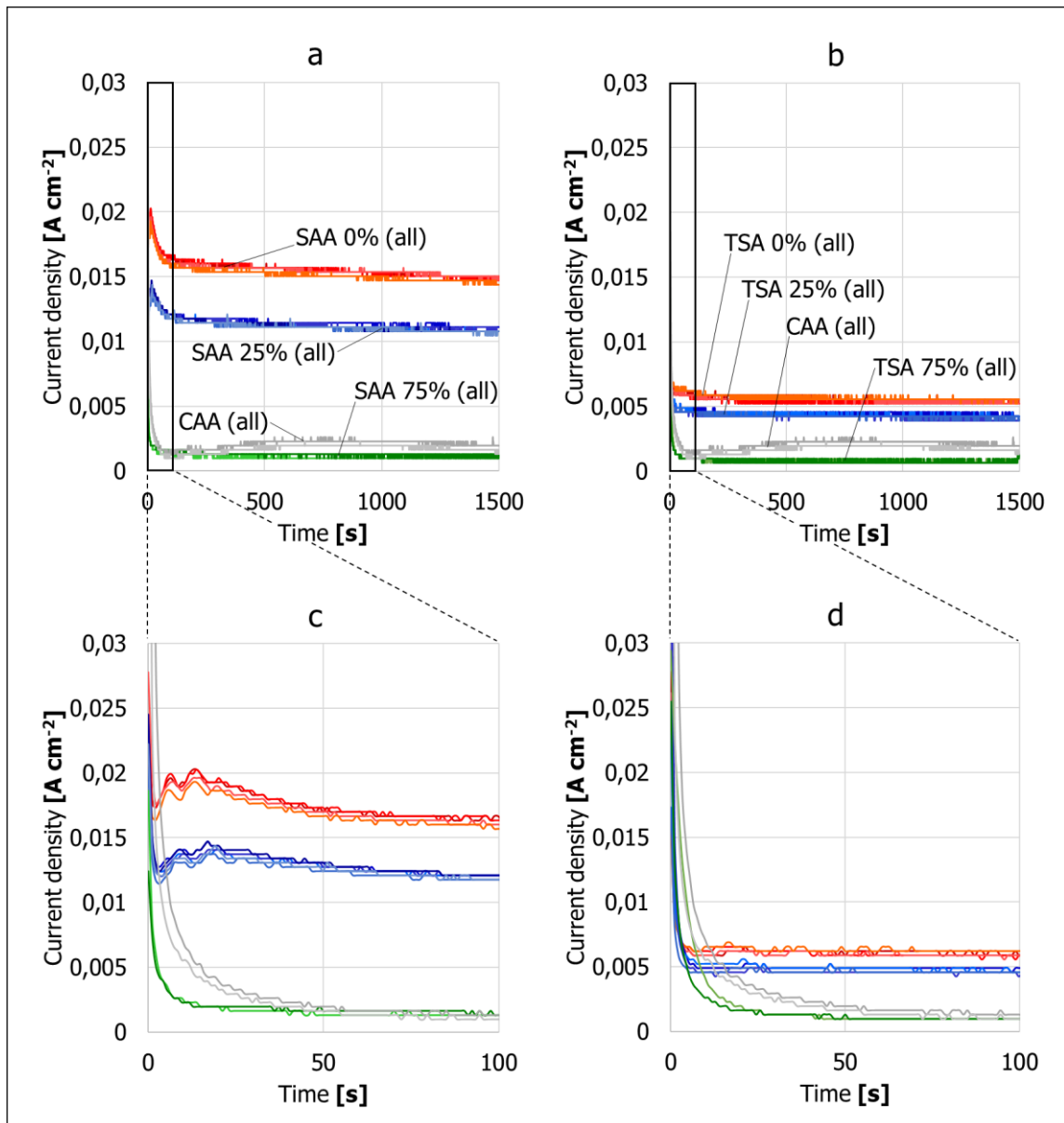
Figure 4. 7: Current density - time curves. All red curved are anodised (either SAA or TSA) with 0 vol% ethylene glycol. The blue curves with 25 vol% ethylene glycol and the green curves with 75 vol% ethylene glycol. The grey curves represent the CAA treatments.

Typically anodising current density curves have a distinct shape which could be divided into four regions, see section 2.3.2 and Figure 2.13. This well-known shape was only observed clearly for all anodising cycles using either the 0 vol% or 25 vol% ethylene glycol containing SAA electrolyte. As described in chapter 2, the typical initial current density transient is caused by the interplay between current originating from the formation of a barrier oxide type and a porous oxide type. During the anodising process the oxide layer is becoming thicker and due to the extremely high electrical resistivity of aluminium oxide (approximately 10^{14} $\Omega \cdot$cm) the current density is dropping. Within a matter of seconds some penetration paths form in the oxide layer due to attack of the aggressive electrolyte which causes the dropping current density to reach a minimum value. The penetration paths act as nucleation sites for pore formation which causes the current to rise again towards a maximum value. As soon as the maximum value is reached the formation of new pores stops and some pore rearrangement will cause some pores to terminate and others to continue growing. This causes a decrease of the current density until a steady-state current density is achieved. At this point the formed pores grow taller at a continuous rate. The observed reduction of this typical transient behaviour and subsequent drop of the steady-state current density with increasing ethylene glycol fraction suggests that the barrier oxide formation current density is becoming more prominent compared to the porous oxide formation current density. In other words, adding ethylene glycol moves the oxide type from being predominantly of the porous type to a more barrier like type. [10,14,79,80] This was confirmed by the work of Stępniowski et al. [14] in which they observed the same transition by adding increasing amounts of glycerol. In fact, a total absence of a porous structure was found after a 1 hour anodising cycle at 50 V in a 100 vol% glycerol 0.3 M oxalic acid electrolyte.

The faradaic nature of the anodising process [20,44–46] allows to make an comparison of the relative thickness of the oxide layers formed with different anodising procedures. As with all faradaic processes current flow is directly related to the electrochemical reaction involved. In the case of anodising of aluminium this means that the electrochemical conversion of aluminium to aluminium oxide is directly related to the recorded current density. In this work the anodising conditions were kept constant except for the electrolyte chemistry and interelectrode distance. This implies that the decrease in current density as a function of increasing ethylene glycol fraction, see Figure 4.7, results in less aluminium being converted into aluminium oxide in the same amount of time. Assuming the faradaic efficiency remains unchanged with a changing electrolyte composition this means the final oxide layer thickness will decrease with increasing ethylene glycol content. Creating an oxide layer of similar thickness in both SAA without and with ethylene glycol would require a longer anodising time for the procedure with added ethylene glycol. [20]

Last but not least it was observed that both the interelectrode distance and the addition of $Ce(SO_4)_2$ did not result in significant changes in current density. In order to clarify Figure 4.8 is showing the steady-state current density at an anodising time of 750 seconds. In this Figure each bar is indicated with an abbreviation of the anodising method used (e.g. SAA), the volume fraction of ethylene glycol used during the anodising procedure (e.g. 25% is short for 25 vol% ethylene glycol), the interelectrode distance used (e.g. 55mm) and whether or not $Ce(SO_4)_2$ was used as an addition to the anodising bath. The latter is indicated by the suffix '+ Ce'. The suffixes [-Y-] and [-C-] indicate the colour of the electrolyte (yellow and colourless respectively) at the start of the anodising procedure, see paragraph 4.1 for more details on the electrolyte colour. It should be stated that the current density was recorded with the power supply used for the anodising process (Delta Elektronika SM 120-25 D) which unfortunately shows the measured current values with a

precision of 10 mA. This means that differences smaller than 10 mA could not be recorded accurately. In the case of the addition of Ce(SO$_4$)$_2$ the concentration of 0.003 M is probably too low to have any significant influence on the electrolyte conductivity and therefore the current density. In literature a significant increase of the reaction rate was measured upon addition of 0.1 M of Ce(SO$_4$)$_2$. This however is much higher concentration of inhibitor (approximately 33 times higher). [18] Research by Sun et al. [81] on anodising of titanium in an ethylene glycol electrolyte containing 0.3 wt% ammonium fluoride and 2 vol% deionised water has reported an increase of the steady-state current density (at 2000 seconds) from approximately 3 mA/cm^2 to approximately 6 mA/cm^2 when decreasing the interelectrode distance from 40 mm to 13 mm. With a substrate of a similar size as the ones used in this current work (anodising area of 30,6 cm^2) this would have resulted in an increase of the recorded anodising current from 91.8 mA to 183.6 mA. Such an increase would have definitely been recorded by the relatively insensitive power supply used here. In the current work the interelectrode distance was changed from 55 mm to 5 mmm, see chapter 3. A change in distance even greater than the one reported in the work of Sun et al. [81]. No significant changes in anodising current were measured however in any of the tested electrolytes. A probable explanation for this is the big differences between the electrolytes tested in this work and the one used by Sun et al. [81], which only contained 0.3 wt% of ammonium fluoride. The small differences in current density in Figure 4.8 between for example CAA 55mm and CAA 5mm are most likely caused by instrument deviations. Only the additions of ethylene glycol clearly result in a different anodising current density. Therefore no error bars are shown.
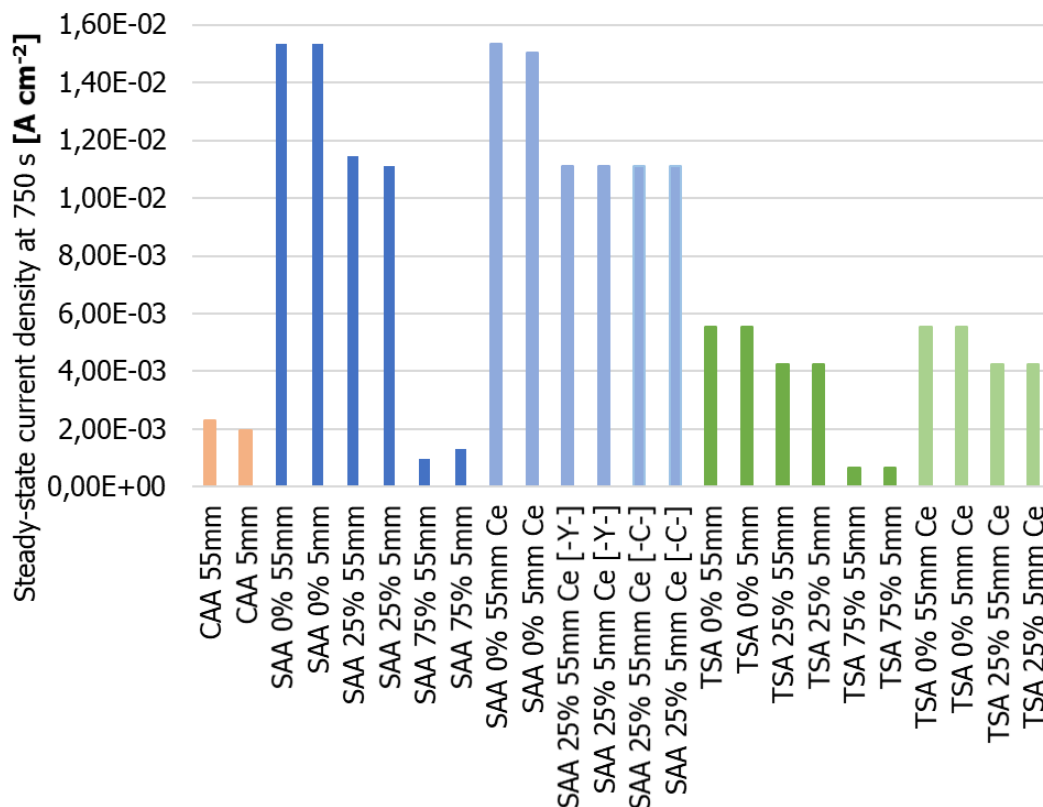
Figure 4. 8: Steady-state anodising current density at after 750 seconds. Each bar refers to one of the anodising processes used. For example: SAA 25% 55mm Ce [-Y-] is the SAA procedure containing 25 vol% of ethylene glycol at an interelectrode distance of 55 mm containing Ce(SO4)2. [-Y-] indicated the electrolyte was in yellow condition during anodising. [-C-] indicated colourless condition.

4.3. Linear Sweep Voltammetry

The corrosion behaviour of all anodised samples was assessed right after anodising in an accelerated manner by means of LSV in a 0.1 M NaCl aqueous electrolyte. The results of the measurements are depicted in Figures 4.9 till 4.14 in the form of polarisation curves. In these figures current density values are absolute values. The curves shown on the Figures in this section however (Figures 4.9 - 4.14) do not show the first 30 mV of the separate scanning regimes in order to increase their readability. Each curve is indicated with an abbreviation of the anodising method (e.g. SAA), the volume fraction of ethylene glycol used during the anodising procedure (e.g. 25% is short for 25 vol% ethylene glycol), the interelectrode distance used (e.g. 55mm) and whether or not $Ce(SO_4)_2$ was used as an addition to the anodising bath. The latter is indicated by the suffix '+ Ce'. The suffixes [-Y-] and [-C-] indicate the colour of the electrolyte (yellow and colourless respectively) at the start of the anodising procedure, see paragraph 4.1 for more details on the electrolyte colour.

Figure 4.9 and 4.10 together show all LSV results obtained subdivided into the two tested anodising geometries. Due to the number of curves depicted in both Figures only a few are highlighted. The non-highlighted curves are shown in more detail in the subsequent Figures. The first thing to notice in both Figure 4.9 and 4.10 is the overall shift of the curves towards lower current densities when comparing the anodised samples with the non-anodised sample. An expected result since the anodising process is intrinsically increasing the thickness of the native oxide layer and therefore improving its corrosion performance. It should be noticed that some of the grey coloured curves show higher current densities in the cathodic branch than the bare sample. This is most likely a result of the relatively long OCP resting time of 4 hours before starting the LSV measurements. The bare alloy is presumably developing some of corrosion products during the OCP resting time which is slowing down the corrosion kinetics, mostly by impeding the ingress oxygen needed for the cathodic reaction. This is reflected by the shift of the cathodic branch to lower current density values. In retrospective view it might have been better to use a shorter OCP resting time of 3 or even 2 hours. The phenomena did not show on preliminary trial measurements using an OCP time of just 1 hour.

The known sensitivity to localised forms of corrosion of AA2024-T3 is reflected by the almost horizontal slope of the anodic branch of the bare alloy. Every small positive change in potential results in a very large increase in current density, which results in a fast transition from activation controlled behaviour into concentration controlled behaviour. This phenomena is less pronounced for the anodised samples and is reflected by their less extreme response to changes of the potential in the positive direction. The reason for this is the anodic oxide layer which is responsible for the more passive behaviour of the alloy. The CAA anodising pre-treatment is clearly outperforming all other treatments tried in this work, which is reflected by the overall lower current density values at basically all potentials in both the anodic and cathodic branches. The main reason for this is the known anodic and cathodic inhibition of the chromates present as residuals at the pore bases. [8,17]
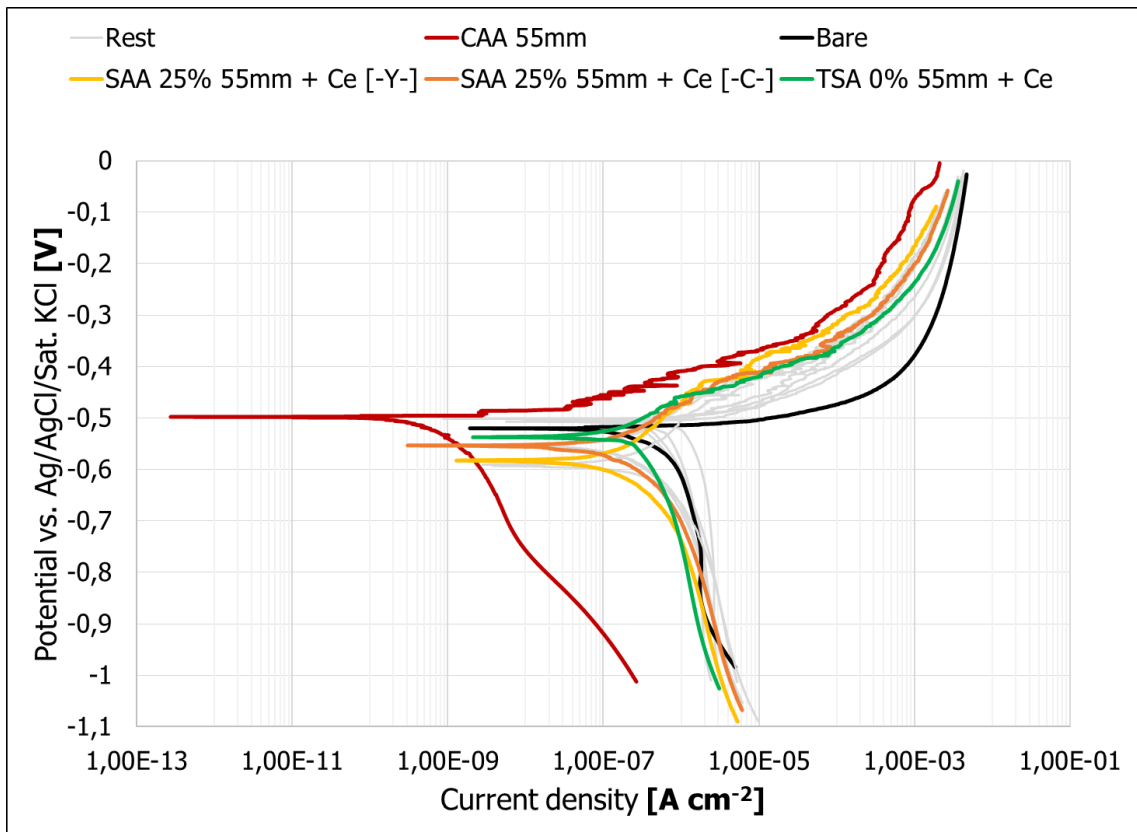
Figure 4. 9: Polarisation curves of all samples anodised in the same interelectrode distance (55 mm).
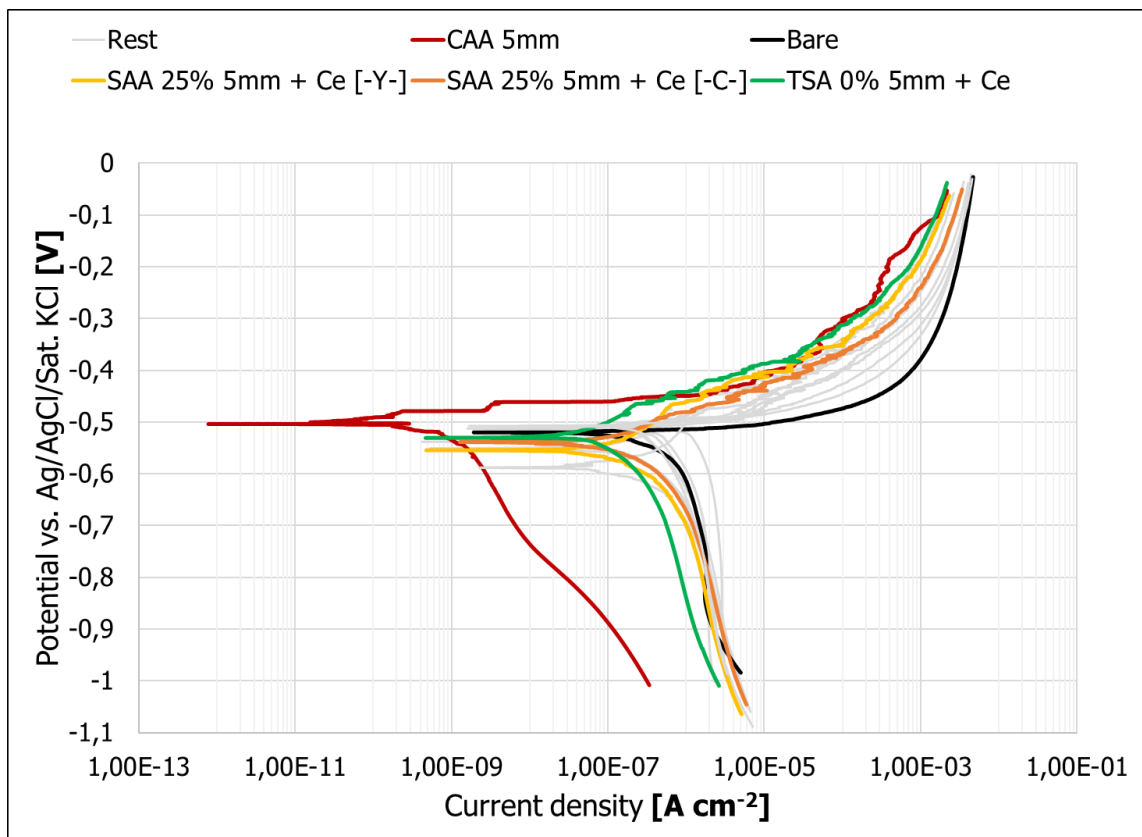
Figure 4. 10: Polarisation curves of all samples anodised in the same interelectrode distance (5 mm).

In order to compare the effects of the ethylene glycol fraction, the interelectrode distance and the addition of Ce(SO$_4$)$_2$ some more detailed Figures are shown below. Figure 4.11 is showing the polarisation curves of both the SAA (4.11a) and TSA (4.11b) anodised samples prepared in different fractions of ethylene glycol. Comparing the curves of the samples anodised in 0 vol% ethylene glycol with the samples anodised in 75 vol% ethylene glycol it is quite clear that the latter is performing worse since the current densities are shifted towards higher values. Besides the rise of the anodic branch of the 75 vol% glycol samples is less steep meaning that small changes of the potential in the positive direction result in larger changes in current density. The sample is therefore more active and prone to localised corrosion. This is best reflected by the SAA anodised samples. Both the SAA 0% 55mm and the SAA 25% 55mm samples show a much steeper slope between the corrosion potential (E$_{corr}$) of approximately -0,55 V vs. Ag/AgCl/Sat. KCl and the anodically polarised potential of approximately -0,42 V vs. Ag/AgCl/Sat. KCl. Further increase of the potential in the anodic direct results again in much larger changes of the current density indicating localised corrosion phenomena have started. For this reason this potential is referred to as the pitting potential, E$_{pit}$. The SAA 75% 55mm sample does not show such a transition in current density behaviour in the anodic branch, it is already very active close to E$_{corr}$. Which basically means that the corrosion potential for this sample is approximately equal to E$_{pit}$. Neither of the TSA anodised samples show the same sort of tendency towards passive behaviour with a distinct pitting potential, so all TSA anodised samples are more active than the SAA anodised samples. Differences between the 0 vol% and 25 vol% ethylene glycol anodised samples (both SAA and TSA) are not evident from the graphs shown in Figure 4.11. The interelectrode distance did not seem to have any significant effect on the corrosion behaviour when comparing the curves without of the samples anodised without cerium. Figure 4.12 shows the polarisation curves of the SAA and TSA samples anodised in 25 vol% ethylene glycol at different anodising geometries, however similar trends were found for all other ethylene glycol fractions.
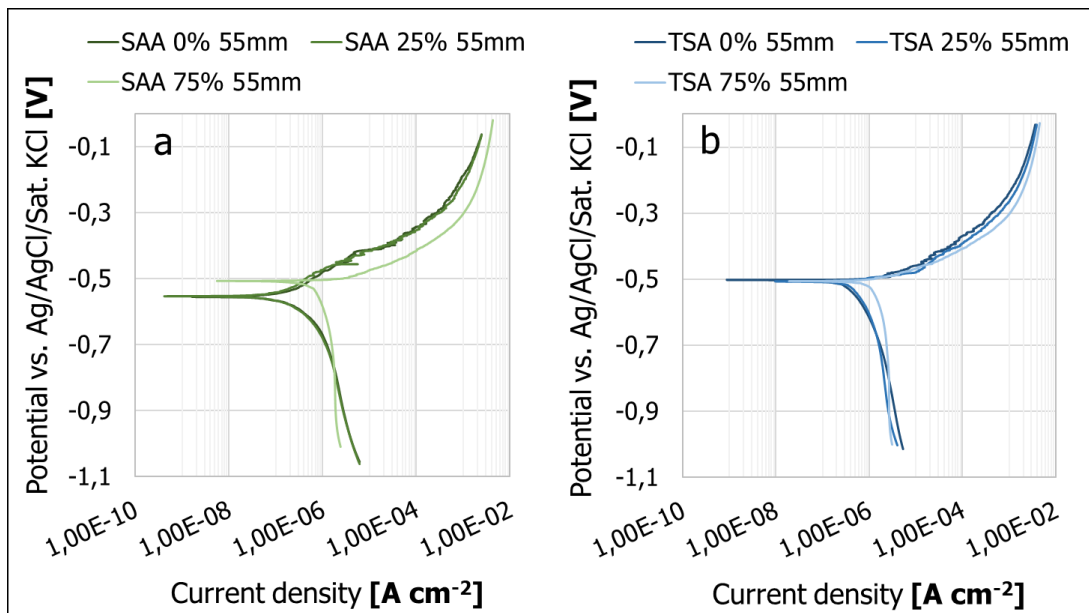
Figure 4. 11: Polarisation curves of both SAA (a) and TSA (b) anodised samples comparing different ethylene glycol fractions.
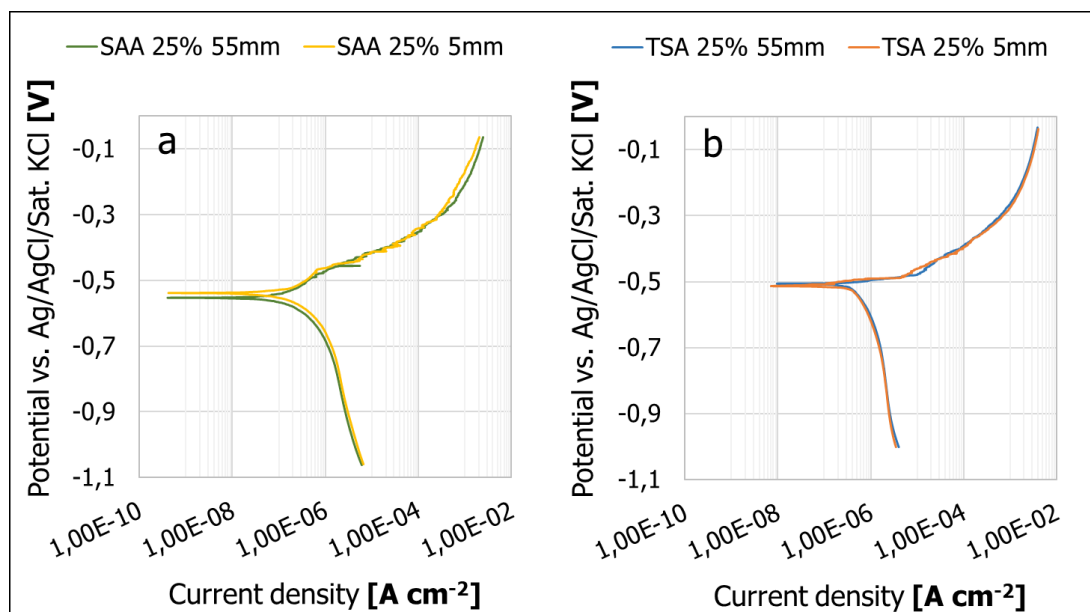
Figure 4. 12: Polarisation curves of both SAA (a) and TSA (b) anodised samples comparing anodising geometries.

The addition of $Ce(SO_4)_2$ to the anodising baths did have different effects on the SAA (Figure 4.13a) and TSA (Figure 4.13b) as was expected from literature. Addition to the sulfuric acid bath did not seem to have any significant effect other than shifting the equilibrium potential slightly towards less noble values, which may indicate a small change in chemical composition of the sample surface. This might have been caused by an accelerated dissolution of copper rich areas by interaction with the cerium species. The absence of copper richer areas in the finished substrate could explain the lowering of the potential, since copper is a more noble material than aluminium and would naturally raise the overall equilibrium potential towards more noble values. In the case of the SAA procedures the interelectrode distance does not seem to have any effect upon the addition of Ce^{4+} species. The addition of $Ce(SO_4)_2$ to the TSA electrolyte on the other hand does seem to have quite a significant effect. Although cerium is added to the electrolyte in a 4+ state it is most likely to be converted to the 3+ state by interaction with tartaric acid, see section 4.1.2. During this interaction some of the tartaric acid is converted to formic acid. The left over is tartaric acid is probably forming negatively charged complexes with the freshly formed Ce^{3+} ions. These complexes are attracted to the positively charged substrate which makes it very plausible that the complexes and therefore both the Ce^{3+} and tartaric acid species are either incorporated in the oxide layer or remain at the pore bases as residuals after the anodising process. Just as already was speculated in literature by Curioni et al. [17,20] and Li et al. [53]. The known cathodic inhibition of Ce^{3+} species and the anodic inhibition of tartaric acid species give rise to observed combination of cathodic and anodic inhibition (shifts of both branches towards lower current density values). The interelectrode distance does also seem to have a significant positive effect on the corrosion performance of the samples anodised with the cerium species containing TSA procedure, see Figure 4.13b. Although no increase in the current density was recorded during the anodising process by changing the interelectrode distance (mainly due to the limited accuracy of the system used), decreasing the interelectrode distance should intrinsically increase the electric field over the anodic oxide being formed. This means that the attractive force acting on the negatively charged complexes will be higher, hence the probability of these species ending up in the oxide or the pores after the anodising process is higher.
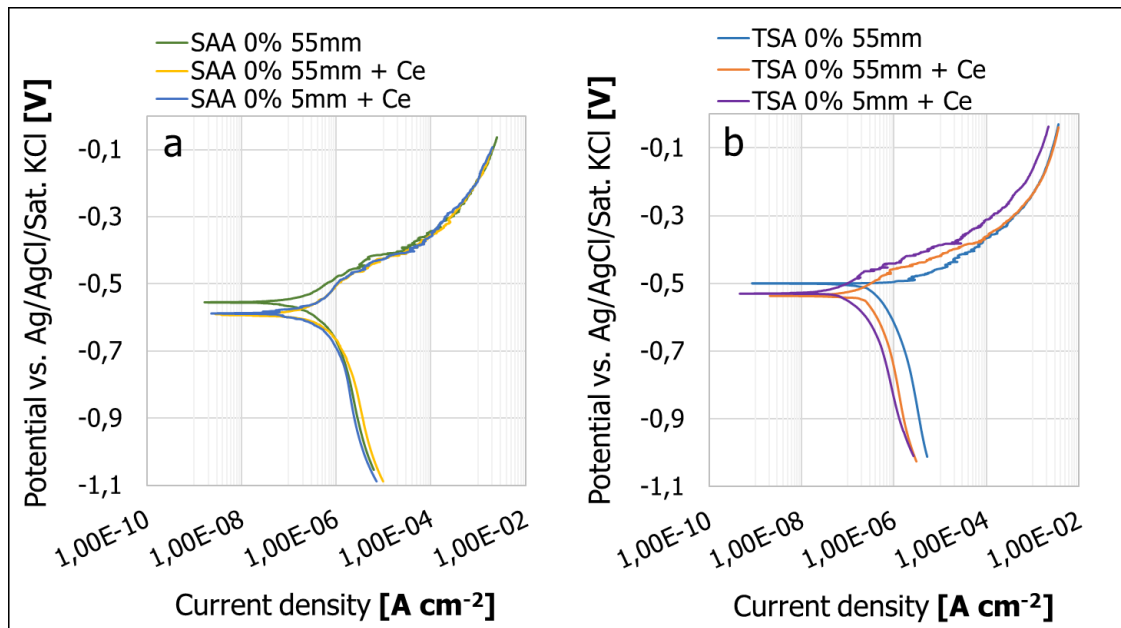
Figure 4. 13: Polarisation curves of both SAA (a) and TSA (b) anodised samples with and without the addition of $Ce(SO_4)_2$ in both anodising geometries.

Last but not least the combined effect of ethylene glycol and cerium should be discussed in a qualitative manner. Figure 4.14 is depicting both the SAA and TSA curved created in a cerium containing electrolyte with and without ethylene glycol addition. As already explained in section 4.1.2. both tartaric acid and ethylene glycol tend to reduce Ce^{4+} to Ce^{3+}. In contrast to Ce^{4+}, Ce^{3+} does not have the high oxidising power (standard electrode potential of +1.72 V vs SHE against -2.34 V vs SHE [54]). This means that it is not likely for Ce^{3+} to have any effect on the anodising process other than slightly changing the electrolyte conductivity. No changes in the anodising current density changes were recorded upon the addition of the low amount of cerium. The positive charge of Ce^{3+} makes that it will be repelled from the positively charged substrate, so it is not likely to end up in the oxide. In other words in the colourless electrolyte condition (SAA 25% 55mm + Ce [-C-]) should not have any effect on the SAA anodising process in 25 vol% ethylene glycol, which indeed is observed in Figure 4.14a. The 'SAA 0% 55mm' curve (without cerium or glycol) is added to this same Figure in order to compare. It is clear from this Figure that both these curve show the same behaviour. Even the equilibrium potential of the 'SAA 0% 55mm' and the 'SAA 25% 55mm + Ce [-C-]' is the same, suggesting no changes in the chemical composition of the surface. The 'SAA 25% 55mm + Ce [-Y-]' curve seems similar to the 'SAA 0% 55mm + Ce' curve, which makes sense since the ethylene glycol containing electrolyte was used for anodising while still being in a yellow condition indicating the presence of Ce^{4+} species. A slight difference in equilibrium potential did occur however. This could either be caused by reference electrode differences or the fact that by the time the anodising process started some of the Ce^{4+} was already converted to Ce^{3+}. The concentration of available Ce^{4+} species therefore would have been lower than the concentration in the electrolyte without ethylene glycol ('SAA 0% 55mm + Ce') reducing the amount of copper rich areas being oxidised.

The combination of ethylene glycol and cerium in the TSA electrolyte also had a negative effect on the corrosion performance of the anodised samples, see Figure 4.14b. Both tartaric acid and ethylene glycol tend to reduce Ce^{4+} into Ce^{3+}, which in itself is not an issue. However it is expected

50

that the main problem arises in the expected complexation process creating the negatively charged complexes, which are drawn towards the substrate. It seems plausible that the ethylene glycol is either competing with the tartaric acid in order to form a complex or prohibiting the tartaric acid to form a complex at all. If competition would be the case than the complexes formed from ethylene glycol and Ce^{3+} are not expected to be negatively charged but instead neutral or even positively charged. This would explain the observed decline in corrosion performance.
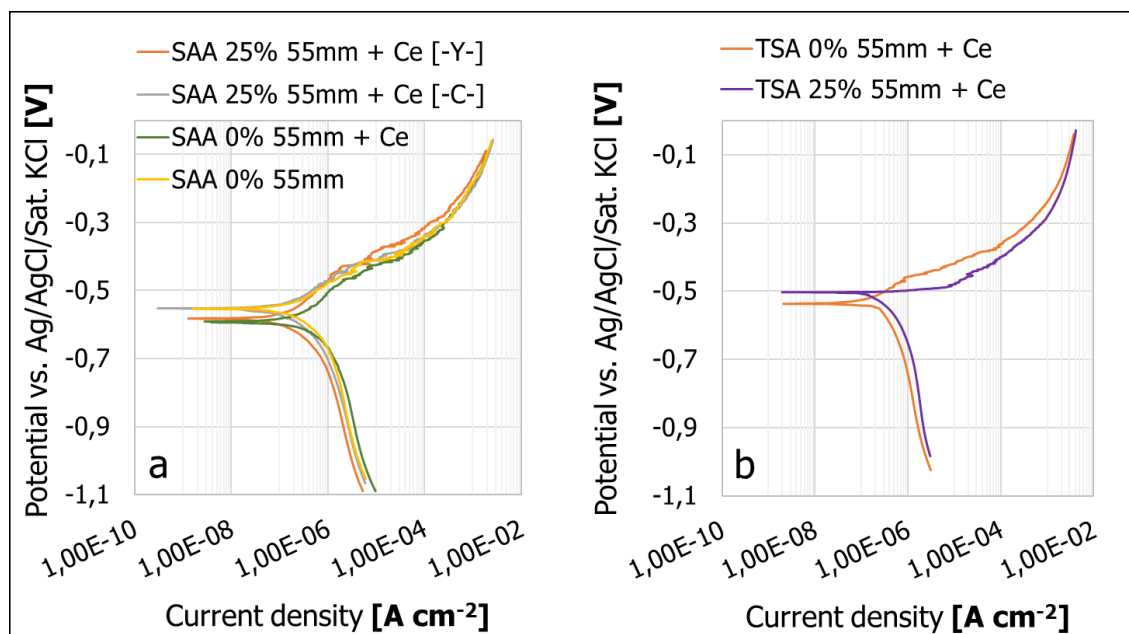
Figure 4. 14: Polarisation curves of both SAA (a) and TSA (b) anodised samples with the addition of $Ce(SO_4)_2$. Comparing the ethylene glycol fractions.

Besides a qualitative analysis the LSV results were analysed in a quantitative manner as well by mean of the polarisation resistance (R_p) and the corrosion current density (i_{corr}). The polarisation resistance was determined using the linear polarisation resistance method and the corrosion current was determined by the Tafel extrapolation method. See chapter 2 and 3 for more information about these methods. Figure 4.15 and 4.16 are showing the polarisation resistances and corrosion currents respectively. The corrosion current density is depicted as its inverse, i.e. 1 divided by the corrosion current, for an easier comparison between R_p and i_{corr}. It should be noted that the inverse corrosion current densities in Figure 4.16 do not have any error bars. This is because of the fact that the anodic and cathodic branches were measured separately and instead of trying to fit all possible combinations of the anodic an cathodic branches the most representative anodic and cathodic branches were selected (positioned somewhere in the middle of the dataset) and used for further fitting. The general trends in both graphs are similar. Taking into account the error bars of the polarisation resistance chromic acid is outperforming all tested alternatives, adding 25 vol% of ethylene glycol does not really affect the corrosion performance, adding 75 vol% of ethylene glycol does have a significant negative effect and adding $Ce(SO_4)_2$ does not really show any difference for SAA but it does for TSA. When ignoring the error bars one could argue a slight improvement of the corrosion performance when adding 25 vol% of ethylene glycol, which could be caused by a densification of the barrier layer and the narrowing of the pores. The error bars however make this quite a bold statement. The interelectrode distance does not have any significant influence on the

corrosion performance of any of the anodic oxides except for the ones prepared in a TSA electrolyte with Ce(SO$_4$)$_2$ but without ethylene glycol. The combination of ethylene glycol and Ce(SO$_4$)$_2$ does not really show any effect in the SAA procedure but does show a severe effect on the TSA procedure. One odd difference for the bare alloy was observed between Figure 4.15 and 4.16. The polarisation resistance of the bare alloy was measured to be among the lowest values of them all, however the determined corrosion current seemed to be lower than some of the anodised substrates (or higher when looking at the inverse corrosion current density). As already explained this is probably caused by built up corrosion products originating from the relatively long OCP resting time of 4 hours. This is probably impeding the ingress oxygen needed for the cathodic reaction. The same phenomenon is not observed during linear polarisation resistance determination since this is only focussing on the first 10 mV around the equilibrium potential.
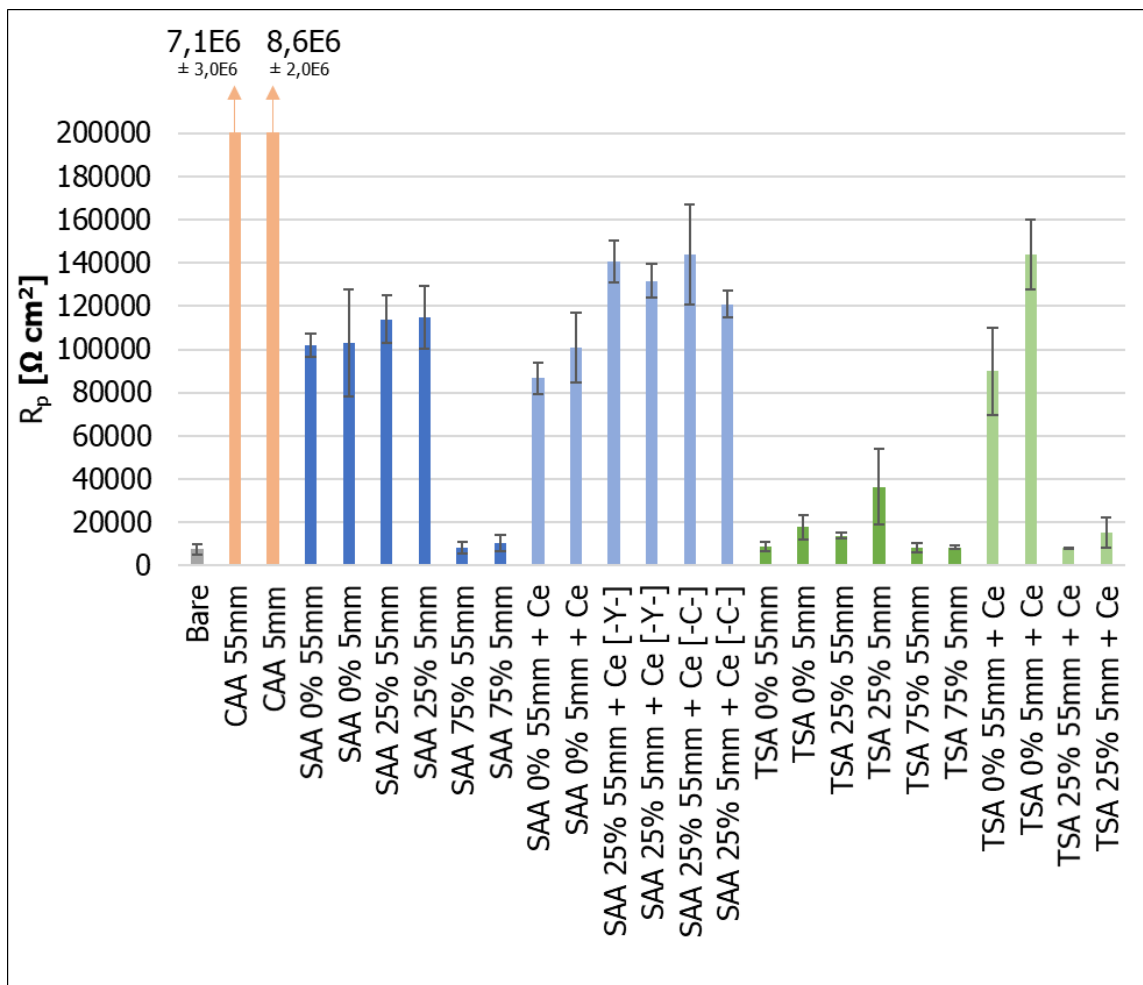
Figure 4. 15: Linear polarization resistances of all anodised samples.
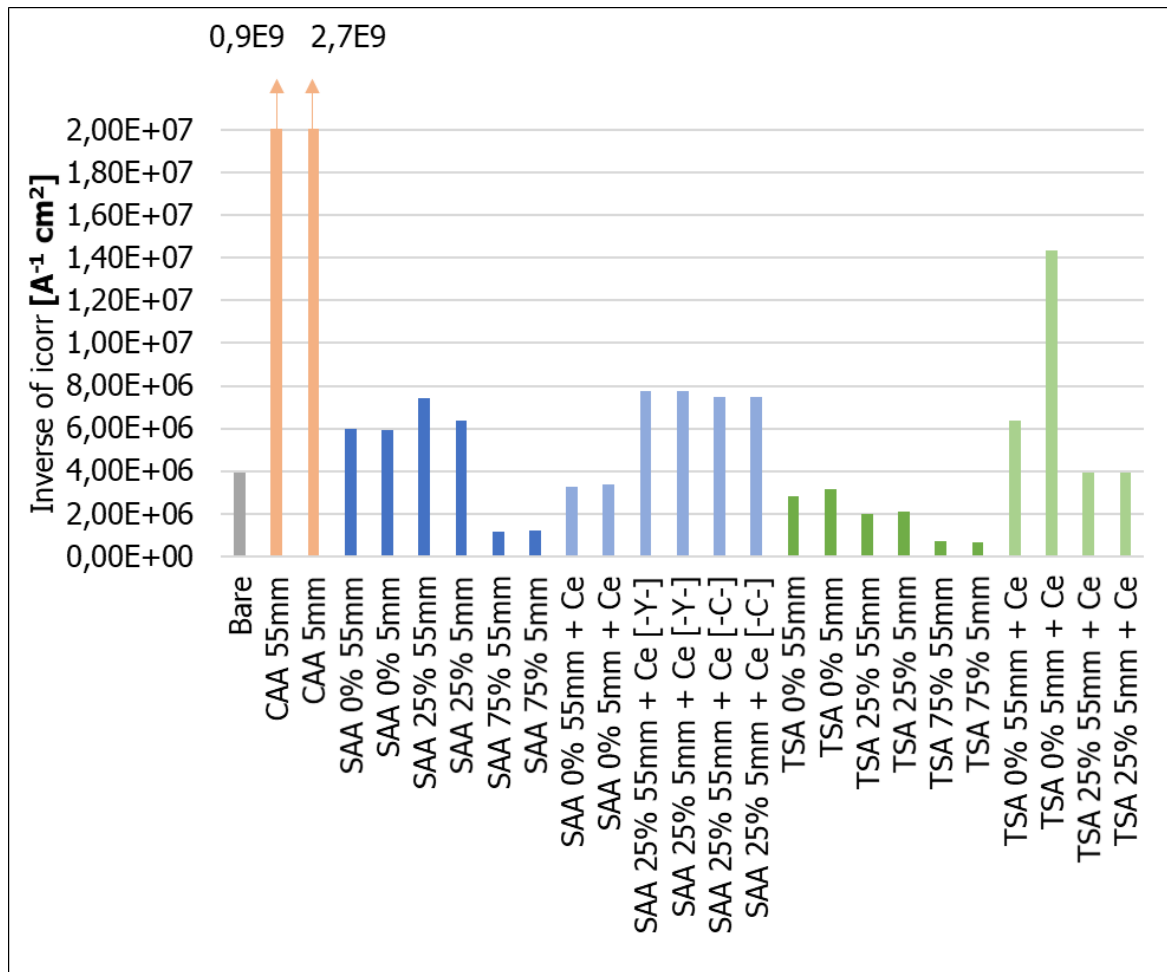
Figure 4. 16: Inverse of corrosion current of all anodised samples.

4.4. Electrochemical Impedance Spectroscopy

In order to monitor the corrosion behaviour over time, electrochemical impedance spectroscopy (EIS) was deployed. As already explained in chapter 3, the EIS data was not fitting to an equivalent circuit. Instead the initial idea was to use the absolute impedance values at 0.01 Hz to access the corrosion performance after 4, 8, 12, 24, 36 and 48 hours. However due to a lot of instabilities occurring below 0.1 Hz the impedance values at 0.1 Hz were used instead. As an example figure 4.17 is showing the bode plots (both magnitude and phase angle) of AA2024-T3 prepared in a 0 vol%, 25 vol% and 75 vol% ethylene glycol containing SAA electrolyte 4 hours after immersion. It is clear that the data below 0.1 Hz is not really usable due to the amount of instability. Probably the relatively non-stationary character of this alloy, discussed in section 4.1.1, is the cause of this unreliable behaviour.
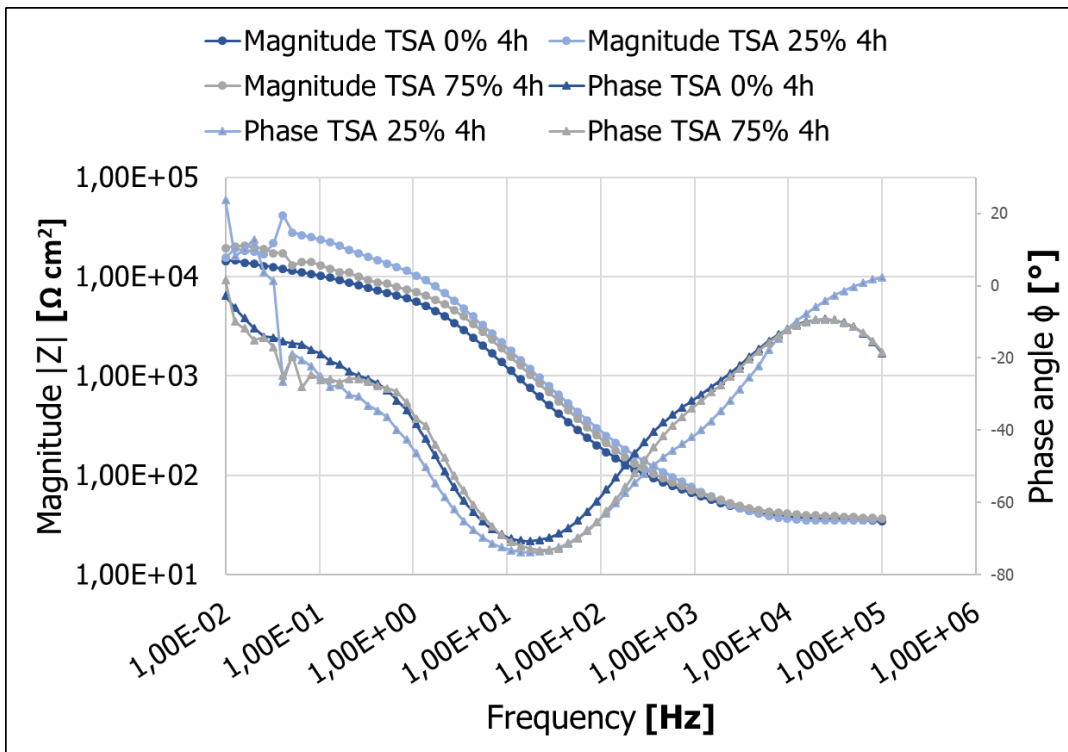
Figure 4. 17: Bode plots of TSA 0 vol%, 25 vol% and 75 vol% anodised samples after 4 hours of immersion (all anodised at 55 mm interelectrode distance without Ce(SO₄)₂).

Figures 4.18 - 4.20 are showing the magnitude of the complex impedances at 0.1 Hz as a function of immersion time for all tested substrates. Figure 4.18 is giving an overview of all techniques used in this work. This includes both the CAA treated and bare substrates (cleaned but non-anodised). The figure is subdivided in two subfigures each representing one of the two used anodising geometries. Between the two subfigures there are no significant observable differences. For both figure 4.18a and 4.18b all anodised substrates show higher absolute impedances values compared to the bare alloy, which resides in the range of 1.00E4 - 2.00E4 Ω cm². This is a result of the increased thickness of the oxide layer present on the material after the anodising process. The SAA and TSA treated substrates are all located in the 2.00E4 - 2.00E5 Ω cm² range. Both the 55mm and 5mm CAA treated substates are located in 1.00E6 - 2.00E6 Ω cm² range, which is significantly higher than all the Cr^{6+}-free alternatives. The observed increase of the impedances values of the bare alloy are most likely caused by the build-up of corrosion products on the surface.

Figures 4.19 and 4.20 show the same results already shown in figure 4.18 however the CAA results are left out in these graphs. Besides the SAA and TSA treated substrates were separated for increased readability. Figure 4.19 is showing the absolute impedances of all SAA treatments and figure 4.20 the same for all the TSA treatments. The impedance values of the bare alloy is included in all figures. Just as in figure 4.18 the subfigures (4.19a, 4.19b, 4.20a and 4.20b) are representing the anodising geometries used, either 55 mm or 5 mm interelectrode distance. Looking at the figures a first observation is the size of the error bars involved. Relatively bad repeatability of the results are causing the large amount of overlap between the error bars of the different techniques used. This makes it quite hard to distinguish the differences between different treatments, especially between the treatments not using 75 vol% of ethylene glycol. As was already stated for figure 4.18 the bare alloy is clearly showing lower impedance values, even when taking into account

54

its error bars. At little higher impedance values the 75 vol% ethylene glycol treated samples reside. This is the case for both the SAA and TSA treatments, clearly reflecting the lower amount of anodic oxides formed during these treatments. The error bars of all other treatments show significant overlap which makes comparison between those treatments quite hard. Looking at the average values in both figure 4.19 and 4.20 it should be noted that no significant differences were found between the two anodising geometries. Only one substrate is clearly deviating from this statement. The substrate anodised at 5 mm with the TSA treatment containing $Ce(SO_4)_2$ but no glycol (TSA 0% + $Ce(SO_4)_2$) is showing a significant difference during the first 24 hours with the same treatment at 55 mm. This trend is in agreement with the findings discussed in section 4.3. The difference is probably caused by an slight increase of the electric field intensity over the anodic oxide layer due to the decreased interelectrode distance. [48] The higher electric field intensity is causing an intensified attraction on the negatively charged Ce^{3+} complexes which are expected to be in solution. Depletion of available Ce^{3+} species is most likely the cause of the steep drop in the first 24 hours of immersion.
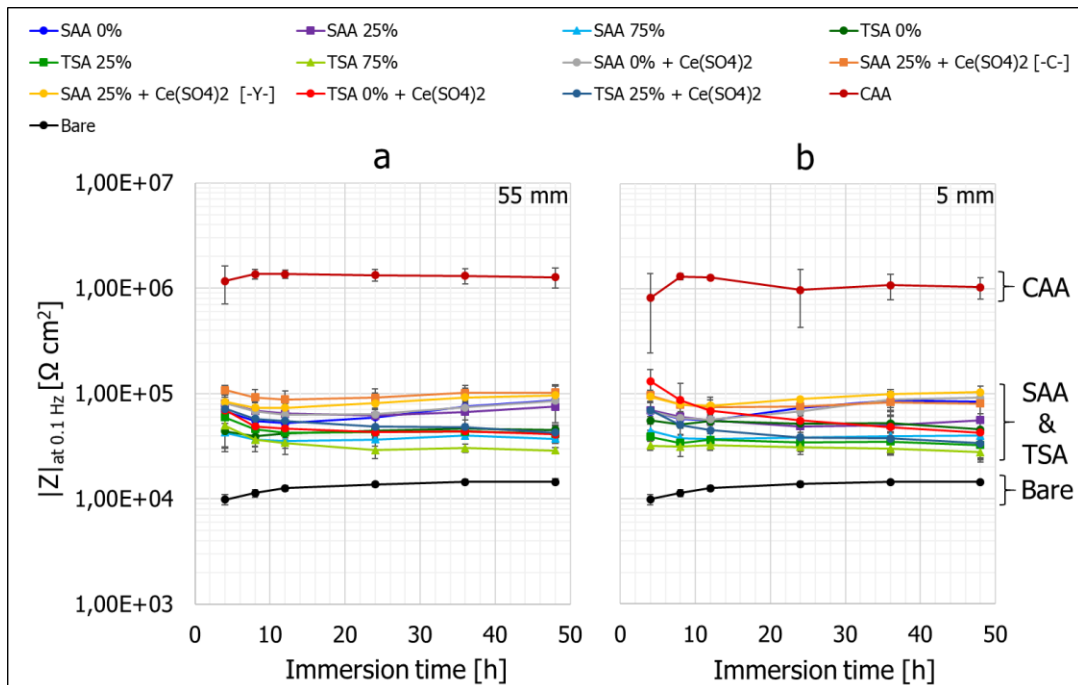
Figure 4. 18: Modulus of impedance at 0.1 Hz versus immersion time plots. Overview of all anodising treatments.

Again looking at the average values the first 12 hours of all treatment show a relatively steep decrease in impedance values. After this initial period the impedances of the SAA treatments tend to go up again and the TSA treatments either stay at the value reached after 12 hours or decrease slightly during the remaining 36 hours of the measurement. The impedance values of the SAA treated substrates tend to go up after the initial period of 12 hours. Similar behaviour was observed by Zhao et al. [82] and was related to a self-sealing process of the porous layer which may happen in NaCl or Na_2SO_4 solutions after some time. During this process anhydrous alumina is converted to the much more voluminous hydrated alumina which is responsible for the sealing effect. Upon immersion in NaCl or Na_2SO_4 solutions two competing reactions are acting on the anodic oxides, self-sealing and deterioration. The latter is caused by the attack by aggressive species, like chloride ions. Depending on the environmental the anodic oxide conditions and one reaction may prevail

over the other. In contrast to the SAA treated substrates (except for the ones prepared in 75 vol% ethylene glycol) neither of the TSA treated substrates show this self-sealing behaviour. A possible difference in pore geometry and a lesser availability of anodic oxide may be responsible for this difference.
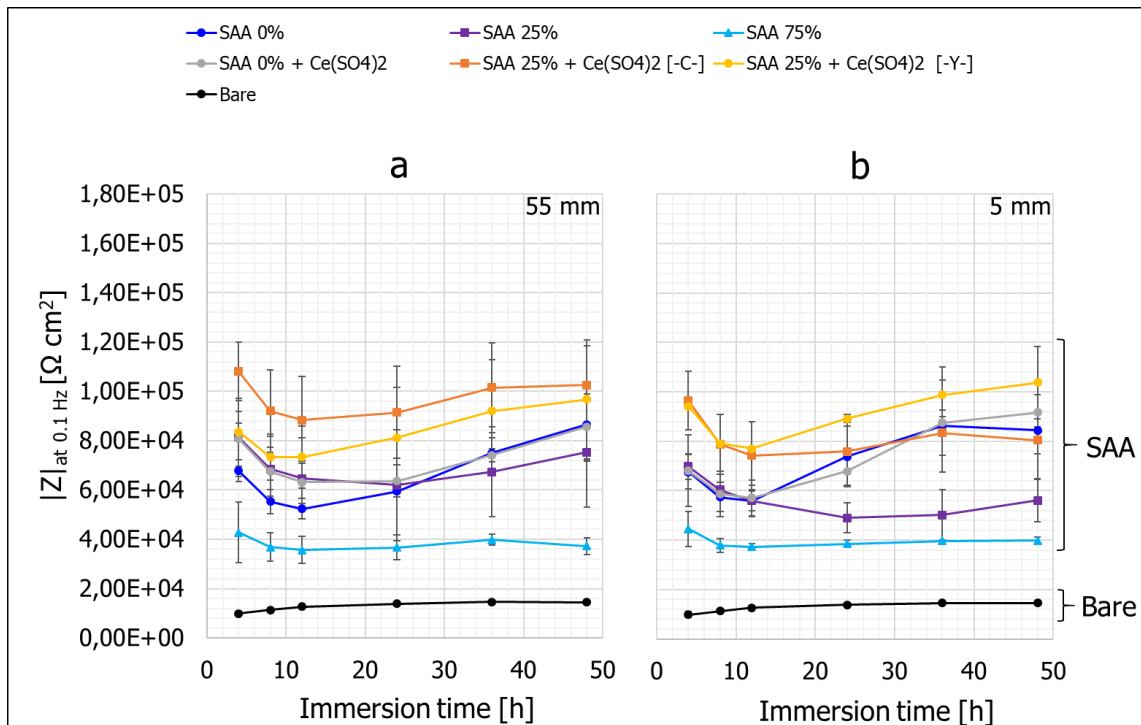
Figure 4. 19: Modulus of impedance at 0.1 Hz versus immersion time plots. Overview of all SAA treatments.
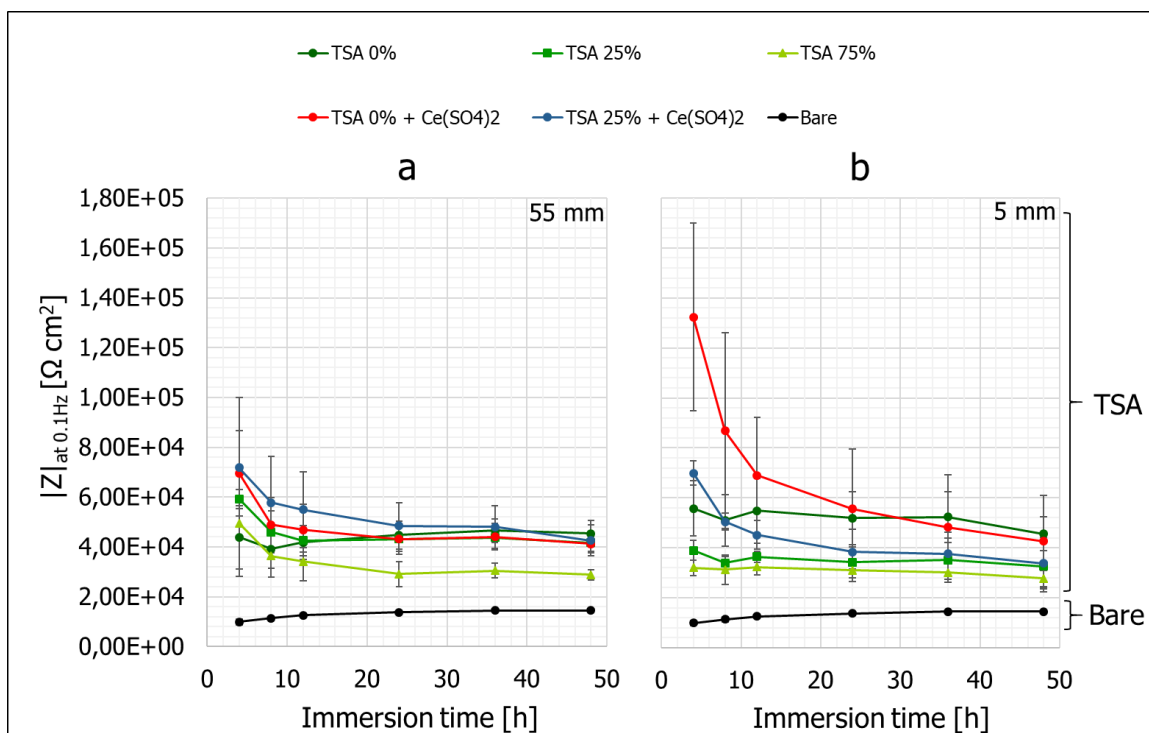
Figure 4. 20: Modulus of impedance at 0.1 Hz versus immersion time plots. Overview of all TSA treatments.

4.5. SEM with EDS

SEM with EDS was deployed to get information about the chemical composition of the near surface region before and after anodising along with a general overview of the substrate surfaces. Figure 4.21 shows four backscatter images (BEC) at 250 times magnification of the substrate surface right after the cleaning procedure (4.21a), after the CAA 55mm procedure (4.21b), after the TSA 0% 55mm procedure (4.21c) and after the SAA 0% 55mm procedure. The first thing to notice is the disappearance of the precipitates observed in 4.21a as the bright white spots, indicating the coverage of the precipitates by the anodic oxide layer. Upon closer inspection of 4.21b still a few precipitates could be observed, some of which are indicated by the black arrows. Figures 4.21c and 4.21d do not show any of these white spots. A thinner oxide layer explains this phenomena, something also confirmed by inspection of the current density response curves in paragraph 4.2. A similar trend was found when comparing images of samples anodised in 100% aqueous electrolytes and samples anodised in partially non-aqueous electrolytes. Both SAA and TSA procedures containing a volume fraction of 75% ethylene glycol showed left over precipitates showing on the SEM images. No differences between interelectrode distance or the addition of $Ce(SO_4)_2$ was observed.
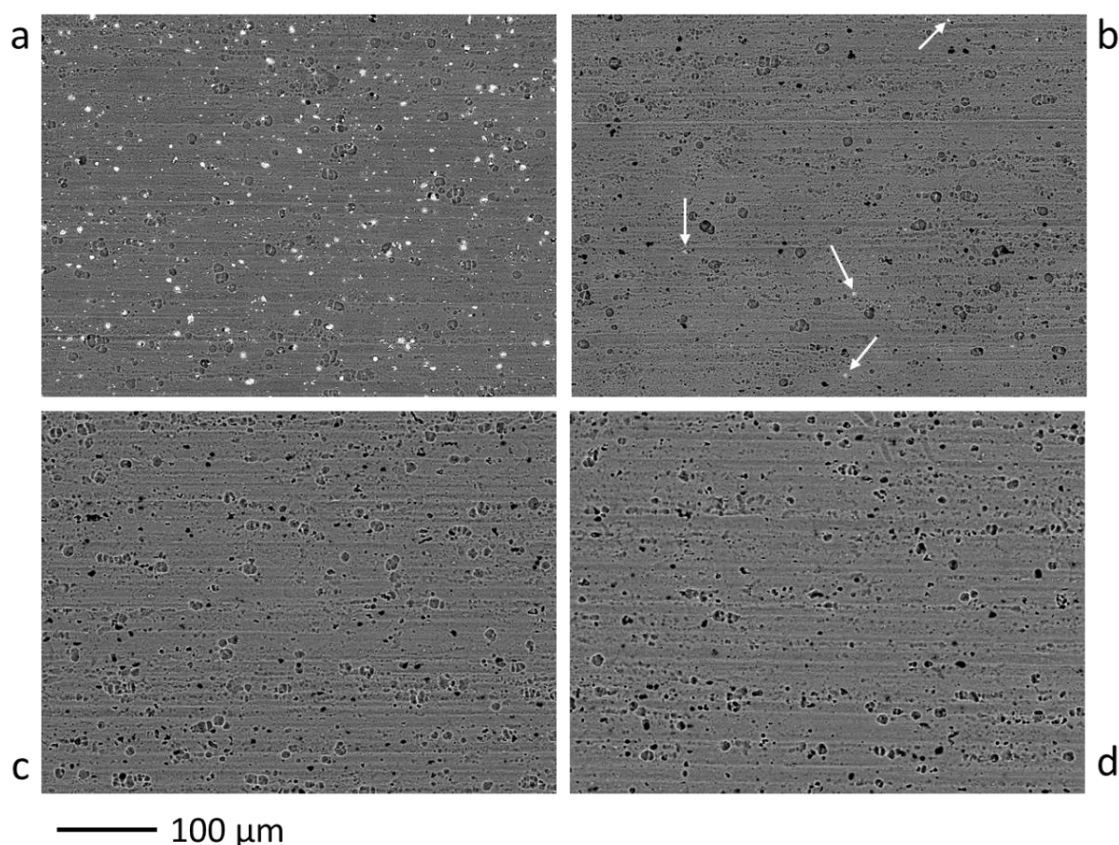
Figure 4. 21: Backscatter images (BEC) at 250x. a: after cleaning step 3, b: CAA 55mm anodised, c: TSA 0% 55m anodised, d: SAA 0% 55mm anodised

In Figure 4.22 the EDS spectra of the substrates prepared by the three main anodising procedures without ethylene glycol are shown. For the sake of comparison the EDS spectrum of the substrate surface right after the full cleaning procedure (S1+2+3) is shown in this Figure again.

From the spectra and the corresponding mass fraction diagram it is evident that compared to the cleaned sample a large oxygen fraction is detected after each of the anodising procedures because of the formation of the relatively thick anodic oxide layer. Besides the growth of the oxygen peak, a decrease of the copper and magnesium peaks was observed for CAA and a total absence for TSA and SAA procedures, which is in correspondence with the few precipitates still showing on the backscatter images in Figure 4.21b. The CAA spectrum clearly shows a smaller mass fraction of oxygen, confirming that less base material was converted into anodic oxides due to the lower current density, see Figure 4.7. Both TSA and SAA procedures showed a distinct sulphur peak, which is caused by the incorporation of sulphate anions into the anodic oxide layer. [10,83,84] The higher concentration of sulfuric acid of the SAA electrolyte (1.69 M) compared to the TSA electrolyte (0.41 M) explains the smaller mass fraction of sulphur detected for TSA anodised substrates.
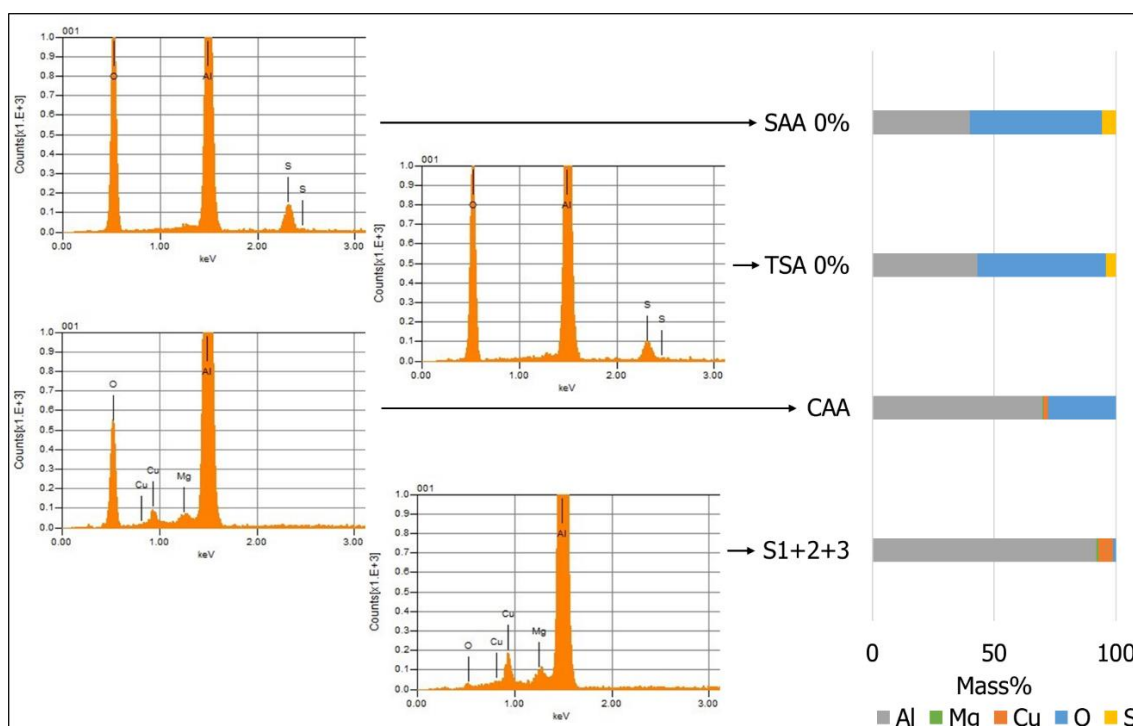
Figure 4. 22: EDS spectra + mass fractions of a cleaned sample, a CAA 55mm anodised sample, a TSA 0% 55mm anodised sample and an SAA 0% 55mm anodised sample.

Comparing the EDS spectra of substrates anodised in electrolytes containing different volume fraction of ethylene glycol showed a similar trend as the one described above. Figure 4.23 shows the mass% of the detected elements as a function of ethylene glycol fraction for both TSA (4.23a) and SAA (4.23b) procedures. Increasing the volume fraction of ethylene glycol decreases the mass fraction of both oxygen and sulphur. As a result the fraction of aluminium is growing since less material is being converted into anodic oxides due to the lower current density, see Figure 4.7. The detected amount of copper and magnesium is increasing with an increasing volume fraction of ethylene glycol. Again this is caused by the inverse relationship between ethylene glycol fraction and current density, which is responsible for the reaction rate of oxide formation and therefore for the final thickness of the oxide layer. Neither the addition of $Ce(SO_4)_2$ nor the interelectrode distance (55 mm vs 5 mm) had any significant effect on the backscatter images and EDS spectra.

This is in agreement with the fact that the anodising current density of all electrolytes with the same volume fraction of ethylene glycol showed approximately the same behaviour, see Figure 4.7. For this reason these results are not shown.
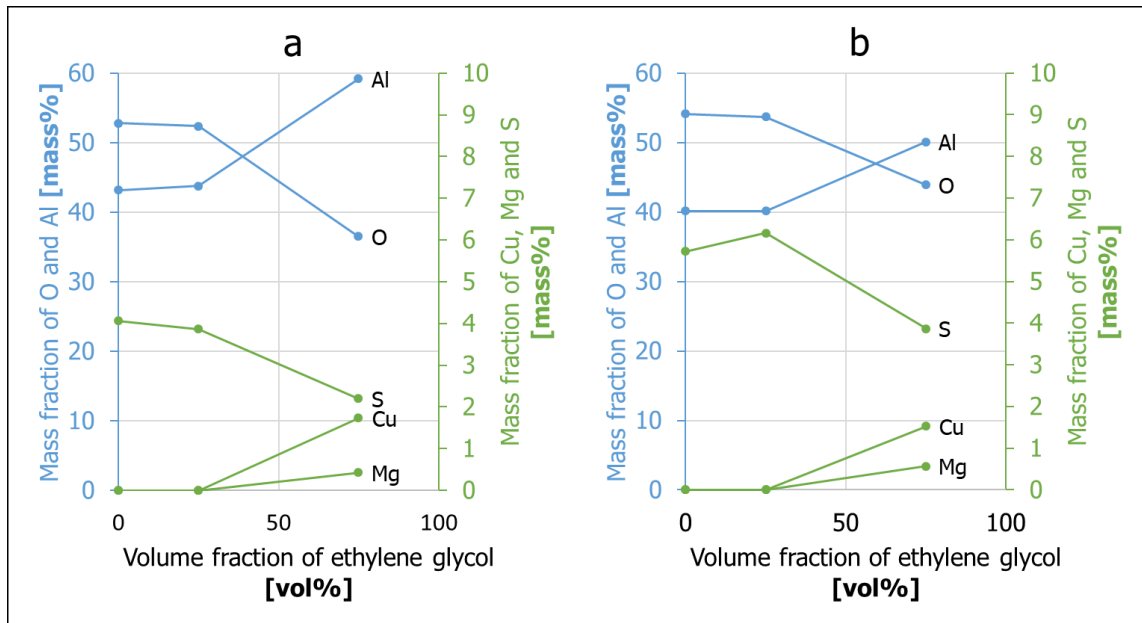
Figure 4. 23: Evolution of constituents as a function of ethylene glycol fraction. a: TSA anodising and b: SAA anodising.

4.6. Immersion tests

Complementary to the electrochemical tests a simple immersion test was conducted to visually assess the corrosion behaviour of a few anodised samples. The micrographs in Figure 4.24 show the sample surfaces before and after 48 hours of immersion in a 0.1 M NaCl electrolyte. The orientation of all samples is the same as indicated in the bottom left corner of the Figure with RD (rolling direction) and TD (transverse direction).

From the micrographs (all at 100x magnification) in Figure 4.24 it is evident that the bare material is performing the worst based on the amount of corrosion product visible and the CAA anodised sample is performing best since no corrosion product was found after the immersion test. Comparing SAA anodised samples, two things should be noted. First of all the typical horizontal lines observed on the bare materials which originate from the rolling process are clearly visible on the sample anodised in a 75 vol% ethylene glycol containing SAA electrolyte (indicated as SAA 75%) while they are nearly absent on the sample anodised in a fully aqueous SAA electrolyte (indicated as SAA 0%), reflecting the difference in anodic oxide layer thickness. Secondly the amount of corrosion pits found on both SAA anodised samples differs significantly. Only a few pits are visible on the samples anodised in the 0 vol% ethylene glycol containing SAA electrolyte while a lot of pits were found on the sample anodised in the 75 vol% ethylene glycol containing SAA electrolyte. A similar trend was found for the TSA electrolytes, indicated in a similar way as TSA 0% and TSA 75%. When comparing the SAA and TSA samples it seems that in both the 0 vol% and 75 vol% ethylene glycol situation the SAA treatments outperform the TSA treatments based on the amount of corrosion product visible. The Ce(SO$_4$)$_2$ inhibitor tested does not seem to have any significant effect on the corrosion performance of the SAA anodised sample based on a visual

inspection of both exposed surfaces, while it has a tremendous effect when added to the TSA electrolyte. It should be noted that corrosion may take place on many different length scales. So it does not necessarily mean the material did not corrode that if corrosion products are not visible with a 100x magnification. Other more sensitive characterisation techniques, like electrochemical noise or high resolution in-situ microscopy, should confirm or refute these statements.
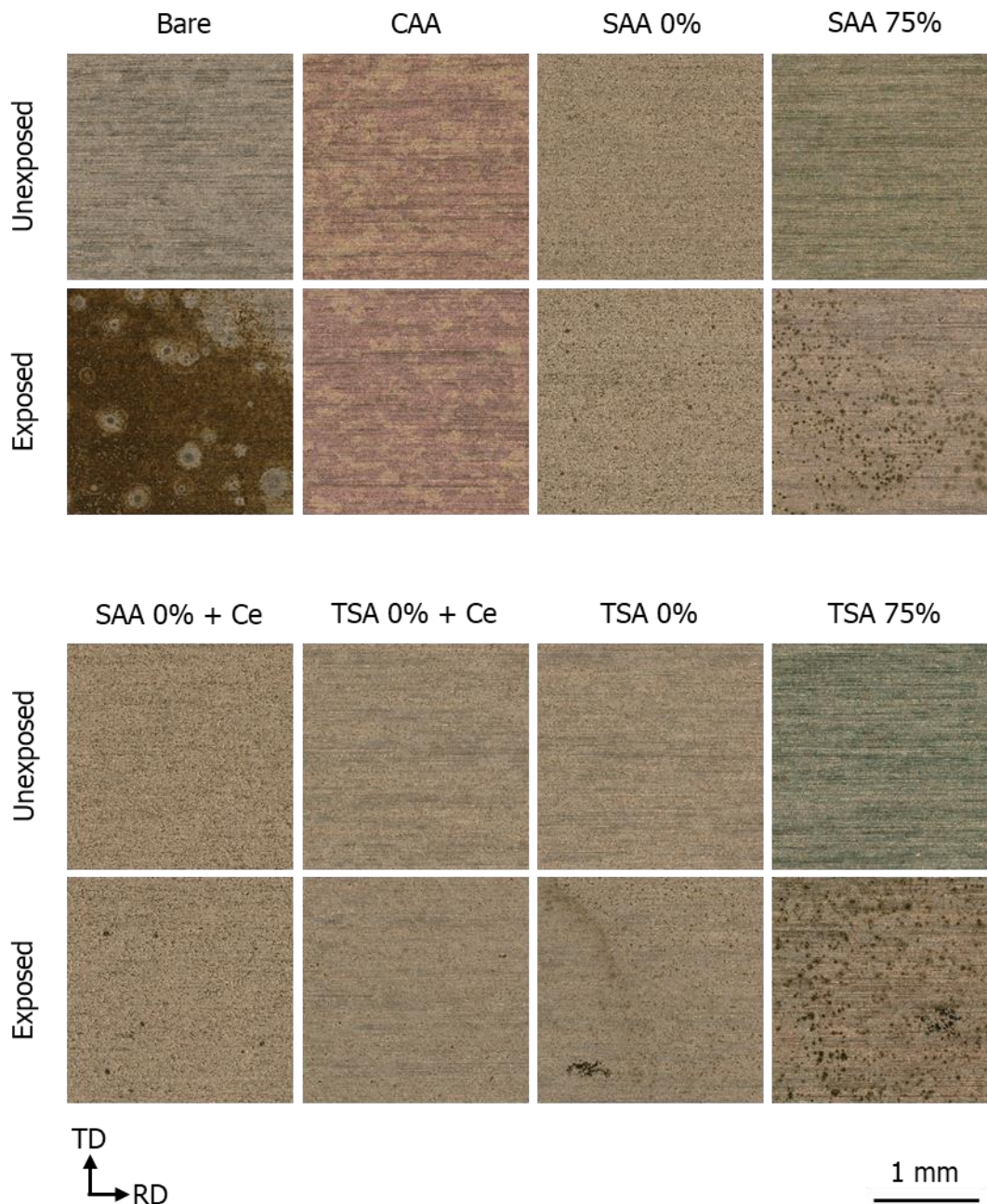
Figure 4. 24: Sample surfaces before and after 48h of immersion in a 0.1 M NaCl solution.

During the immersion test the open circuit potential of each sample was recorded, see Figure 4.25. The bare material shows just like the anodised samples a fairly quick drop of the OCP during the first few minutes caused by the initial breakdown of either the native oxide layer (bare sample) or the anodic oxide layer (anodised samples). This initial period for the bare material is followed by a period of approximately 18 hours of a relatively steady potential value. After this period the

60

potential starts dropping at an almost linear rate indicating the general corrosion process has started and continues over time. All other curves (the anodised samples) do not show this kind of behaviour. They do however all show sudden drops followed by a steep rise in the potential caused by the initiation, growth and repassivation of corrosion pits. [69–71] This phenomenon is most pronounced for the CAA anodised sample due to the fact that the oxide layer is relatively thin and therefore more prone to corrosion, on the other hand do the chromate ions act as corrosion inhibitors by forming chromium oxide deposits on active sites which quickly restores the corrosion protection. [8,44,80]
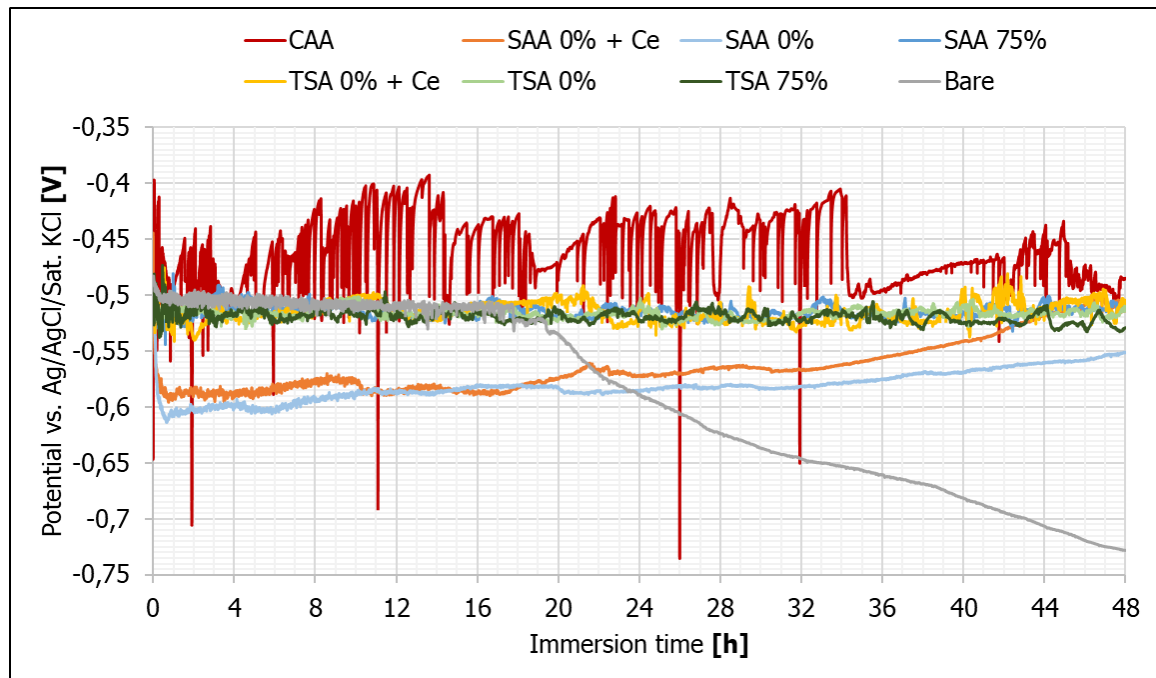
Figure 4. 25: Open circuit potential of immersion test samples.

4.7. Overall discussion and interpretation

In this work four different characterisation techniques, with a strong focus on characterising corrosion performance, were used to characterise anodic oxides formed on AA2024-T3. The techniques consisted of LSV, EIS, SEM with EDS and Immersion tests. Apart from that the fcurrent density responses of the anodising processes were also recorded and analysed. This section summarises the findings and gives an overall discussion aiming to relate all the separate findings and to propose a responsible mechanism.

The preliminary observation made on the OCP, the interaction between $Ce(SO_4)_2$ and the electrolytes and SEM images of the cleaning procedures described in section 4.1 resulted in four findings. The first finding was the high level of instability or non-stationarity of AA2024-T3 when immersed in a 0.1 M NaCl solution, which are caused by initiation, repassivation and growth of corrosion pits. [69–71] This was found for both anodised and non-anodised substrates, even after an extended period of immersion time. The second finding was the observed interaction between $Ce(SO_4)_2$ and tartaric acid, which was related to the reduction of the Ce^{4+} species into Ce^{3+} species and the transformation of tartaric acid to formic acid and carbon dioxide. [73] The third finding was

very similar to the second one, however the reduction of Ce^{4+} was found to be triggered by ethylene glycol. It was found in the literature that ethylene glycol is converted into formaldehyde. [74] In other words, the addition of Ce^{4+} species to either a solution containing tartaric acid or ethylene glycol eventually results in a solution only containing Ce^{3+} species. The observed slow reaction kinetics of the reaction between Ce^{4+} and ethylene glycol, due to the slow change in electrolyte colour, allowed anodising in both a yellow coloured and colourless situation. The fourth and last preliminary finding confirmed that the as-received alloys were cleaned properly by the commercial cleaning procedure used and the near-surface region containing very fine IMs was actively removed.

Analysis of the current density response of the used potentiostatic anodising processes in section 4.2 confirmed a significant decrease in overall current density with increasing volume fraction of ethylene glycol. This was found to be related to the increase of the hydrodynamic radius of the ions involved and viscosity of the electrolyte which both negatively affect the ionic mobility and therefore lower the current density. [14] The faradaic nature of the anodising process allowed to state that the decrease in current density resulted in a thinner overall thickness of the oxide layer. [14] The transient phenomenon observed at the beginning of a current density response curve diminishing with increasing volume fraction of ethylene glycol indicating a transition from a typical porous type anodic oxide to a barrier type anodic oxide, which was also observed by Stępniowski et al. [14]. Both the interelectrode distance and the addition of 0.003 M $Ce(SO_4)_2$ did not show any significant measurable differences in the current density response. In the case of the addition of $Ce(SO_4)_2$ the low concentration and the relatively low sensitivity of the power supply are most likely the reason for the insignificant differences in current density. In the case of the interelectrode distance the main reason is most likely the instrument insensitivity and the fact that the amount of available charge carriers in the electrolyte was much higher than the one used in research by Sun et al. [81] in which a more significant change was recorded.

Qualitative analysis of the LSV measurements showed a superior corrosion performance of the CAA prepared anodic oxides, which is most likely caused by anodic and cathodic inhibition of the chromates residing at the pore bases. [8,17] Furthermore the anodic oxides prepared in 75 vol% of ethylene glycol (both SAA and TSA) are clearly underperforming with higher current densities and more active behaviour in the anodic region. No significant differences were found between substrates prepared in 0 vol% and 25 vol% ethylene glycol respectively. The addition of $Ce(SO_4)_2$ did not have any significant influence on the corrosion performance of the SAA treated substrates. The most probable reason for this is a too low concentration of $Ce(SO_4)_2$. In literature concentrations of approximately 33 times higher let to improvements in the corrosion performance of anodic oxides. [18] The combination of $Ce(SO_4)_2$ and the TSA electrolyte however did result in improvements of the corrosion performance. Probably caused by the formation of negatively charged complexes with Ce^{3+} in a TSA electrolyte [17,20,53] which are attracted to the substrate during the anodising process. No effect of the interelectrode distance on the corrosion behaviour of the substrates was found with one exception. The substrates anodised with a TSA electrolyte containing cerium but no ethylene glycol showed a significant improvement for the 5 mm interelectrode distance. The expected negatively charged cerium complexes in the TSA electrolyte [17,20,53] are drawn more strongly towards the substrate during the anodising process due to the fact that a smaller interelectrode distance will intrinsically increase the electric field intensity over the anodic oxide. Quantitative analysis of the LSV results in the form of the polarisation resistances and the corrosion current densities showed similar trends as found for the qualitative analysis.

Comparing the polarisation resistances and the corrosion currents of both the 0 vol% and the 25 vol% ethylene glycol give indications of a slight improvement of the corrosion performance in favour of the latter. This may be caused by a densification by the barrier layer and shrinkage of the pores as described by Chen et al [12]. The error bars however are overlapping in such a way it should not be called a significant difference.

An assessment of the corrosion behaviour over the course of 48 hours using EIS showed similar trends as the ones found with LSV. The substrates prepared in a 75 vol% ethylene glycol electrolyte were clearly found to be underperforming from the rest of the anodised substrates. No major differences were found between all of the other anodised substrates. Just as already observed with the LSV measurements the addition of $Ce(SO_4)_2$ to a 0 vol% ethylene glycol containing TSA electrolyte showed significant improvements, especially for the substrates anodised at 5 mm interelectrode distance. Looking at the average impedance values at 0.1 Hz an initial drop in impedance was observed during the first 12 hours for all samples which was related to the initial breakdown of the anodic oxide layer. After the this initial period the SAA treated substrates were in contrast to the TSA substrates showing an increase of impedance which was related (based on literature [82]) to the possibility of a self-sealing mechanism caused by the hydration of anhydrous alumina in the pore walls. [82]

Chemical analysis of the near-surface region of the anodised substrates using SEM and EDS did only show the elements aluminium, oxygen, sulphur, copper and magnesium. Increasing the fraction of ethylene glycol resulted in a decrease in of detected oxygen and sulphur and an increase of aluminium, copper and magnesium. This is in accordance with the measured decrease in anodising current density with increasing ethylene glycol content, which intrinsically results in a thinner oxide layer. Exact thicknesses of the anodic oxides (including the barrier layer) should be evaluated with high resolution SEM to prove this however. No compositional differences were found between different interelectrode distances. No cerium was detected on the substrates anodised in a cerium containing electrolyte. For the SAA electrolytes this seems reasonable since the cerium species reside as a positively charged species which are not attracted to the substrate, however for the substrates prepared in a TSA electrolyte this seems hard to believe due to the dramatic increase in corrosion performance. The lack of sensitivity of the used equipment could be a possible reason for this. Measurements with more surface sensitive techniques like Auger electron spectroscopy or X-ray photoelectron spectroscopy should prove or disprove this.

Last but not least the immersion test were used to strengthen the other findings. The immersion test confirmed the deterioration of the corrosion performance with the addition of 75 vol% ethylene glycol. Besides the CAA treatment did not show any visible corrosion products after the full immersion test of 48 hours reflecting its superior corrosion performance. Furthermore no difference was observed between SAA without cerium and SAA with cerium. A dramatic improvement between TSA without cerium and TSA with cerium was observed however confirming the electrochemical findings.

Although high resolution SEM observations and a more surface sensitive analysis like Auger or XPS are missing an attempt was made to graphically explain the main findings, which are the observed effects of the addition of ethylene glycol and the addition of cerium to the TSA treatment. Figure 4.26 is visualising the expected effect of ethylene glycol on the anodic oxide formed by either an SAA or TSA procedure. The decrease of the anodising current density should be reflected by a decrease in overall thickness of the anodic oxide due to the faradaic nature of the anodising process. [20,44–46] According to Chen et al. [12] the thickness of the barrier layer should remain

constant but becomes more dense, which could indeed be the case for the 25 vol% ethylene glycol situation but seems questionable for the 75 vol% situation. The anodic oxides formed by a 75 vol% ethylene glycol electrolyte (either SAA or TSA) lead to such a decline in corrosion performance that the anodic oxides created should be very thin. The absence of the distinct transient phenomenon in current density response at the beginning of the anodising process does imply the absence of a porous layer or at the formation of a very insignificant one.

Figure 4.27 is showing the effect of interelectrode distance on the anodic oxides created with a TSA procedure with the addition of $Ce(SO_4)_2$ but without ethylene glycol. The green areas at the pore bases indicate the inclusion of the cerium complexes. The decrease of the interelectrode distance which leads to a slight increase of the electric field strength attracts more cerium complexes. For this reason the green area is depicted as a thicker layer. In other situation neither the interelectrode distance or the addition of $Ce(SO_4)_2$ did show any significant effect. For this reason no visualisations are represented for these tested variables.
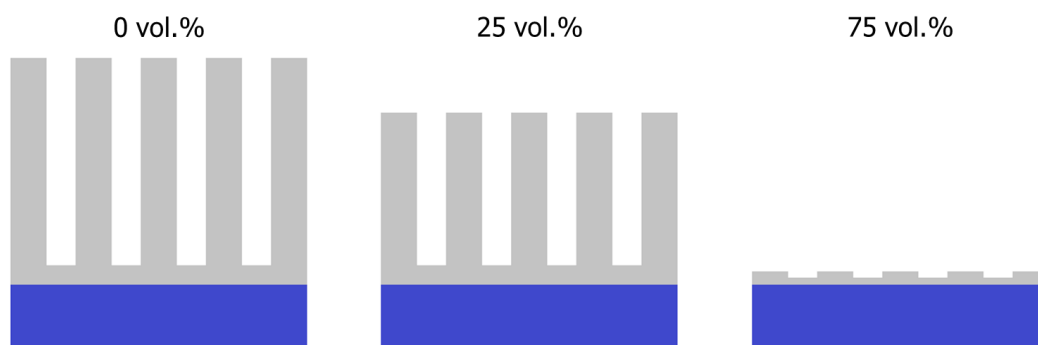
Figure 4. 26: Visualisation of the effect of ethylene glycol on the anodic oxide formed by either SAA and TSA.
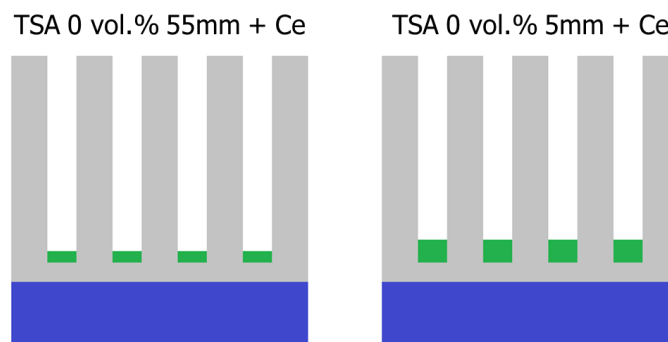
Figure 4. 27: Visualisation of the effect of cerium on the anodic oxide formed by TSA. The green areas indicate cerium residuals at the pore bases.

5. Conclusion and recommendations

The aim of this work was to provide new insights into the effects of the anodising electrolyte viscosity (modulated with ethylene glycol), the anodising interelectrode distance and the addition of $Ce(SO_4)_2$ on the corrosion performance of AA2024-T3 anodised with an SAA and a TSA anodising procedure. In order to formalise this a research question and a hypothesis were formulated.

Research question:
What is the effect of the anodising electrolyte viscosity, the interelectrode distance and the addition of $Ce(SO_4)_2$ to the anodising electrolyte on the corrosion performance of AA2024-T3?

Hypothesis:
Due to the decreased pore diameter [12,14], the increased interpore distance [12,14] and the tighter barrier layer [12], it is expected that an increased viscosity of the anodising electrolyte has a positive influence on the corrosion behaviour of anodised AA2024-T3. The observed improvement of the corrosion performance of titanium in similar circumstances is strengthening the expectation. [16] The expected effect of the interelectrode distance remains unclear because according to literature only the regularity ratio is affected, however depending on the anodising voltage and temperature it could either improve or deteriorate. [15] Last but not least the addition of $Ce(SO_4)_2$ to the anodising bath is expected to have a positive influence on the corrosion performance of AA2024-T3 due to its proven positive effect upon addition to different anodising electrolytes. This includes sulfuric, tartaric and mixed acid electrolytes. [17–20]

Based on the finding in this work the following could be concluded about the three investigated variables: electrolyte viscosity, interelectrode distance and $Ce(SO_4)_2$.

5.1. Electrolyte viscosity

Increasing the anodising electrolyte viscosity by adding ethylene glycol as an electrolyte modulator showed the following effects.

1. The average anodising current density was lowered for both the SAA and TSA anodising procedures by increasing the amount of ethylene glycol, reflecting slower reaction kinetics. In turn this translates into a thinner anodic oxide, however this should be confirmed by high resolution SEM observations in future work.

2. The typical transient phenomenon in the current density response of the anodising process was found to be diminishing with an increase of ethylene glycol content reflecting the transition from a porous type anodic oxide to a barrier type anodic oxide. This should however be confirmed by high resolution SEM observations in future work.

3. No significant differences in corrosion performance between the substrates prepared in a 0 vol% and a 25 vol% ethylene glycol electrolyte were found. Although the overall thickness of both anodic oxides should differ, as reflected by the difference in anodising

current density, the barrier layer thickness and density should be similar. The pore diameters and interpore distances should also be similar for the 25 vol% substrates. The actual morphologies should be studies by high resolution SEM in future work to confirm this. Ignoring the error bars a slightly better corrosion performance of the 25 vol% substrates could be argued. Therefore it seems interesting to check the corrosion performance of substrates anodised in SAA or TSA electrolytes containing more than 25 vol% ethylene glycol but less than 75 vol%.

4. A tremendous drop in corrosion performance was found for the 75 vol% substrates. Clearly the anodic oxide does not form very well in these electrolytes in combination with the anodising procedures tested. As reflected by the much lower anodising current density the anodic oxide should be much thinner than the one obtained at 0 vol% and the 25 vol%. Besides the lack of the typical transient phenomenon does suggest the transition to a more barrier type anodic oxide. The oxide forming and oxide dissolving reactions are most likely more leaning towards the latter which results in poor build-up of anodic oxides. The actual morphology should be studies with high resolution SEM in future work.

5. EDS spectra show a decrease in oxygen and sulphur mass fractions with increasing ethylene glycol content confirming slower reaction kinetics and a thinner anodic oxide layer.

5.2. Interelectrode distance

The difference in interelectrode distance (55 mm versus 5 mm) of the anodising process showed the following effects.

1. No significant differences in corrosion performance found between the substrates anodised at 55 mm and 5 mm interelectrode distances using electrolytes without $Ce(SO_4)_2$.

2. With the exception of one substrate no differences were found for the substrates anodised at 55 and 5 mm interelectrode distances using electrolyte with $Ce(SO_4)_2$. Only the TSA electrolyte with $Ce(SO_4)_2$ and without ethylene glycol showed a significant difference. This is most likely caused by the attraction and incorporation of negatively charged cerium complexes, which are thought to be present in the TSA electrolyte. This however should be further investigated in future research.

5.3. Ceric sulphate

The addition of 0.003 M $Ce(SO_4)_2$ to the anodising bath showed the following effects on the anodised substrates.

1. No effect was found on the SAA anodised substrates. This was most likely caused by the low concentration of $Ce(SO_4)_2$. This should be verified in future work by increasing the concentration of $Ce(SO_4)_2$ to for example 0.1 M.

2. A significant effect on the corrosion performance was found on the substrates anodised with the TSA procedure. The plausible formation of negatively charged Ce^{3+} complexes in the TSA electrolyte make that they are attracted towards the substrate. This makes it more likely for the cerium species to end up at the pore bases as residues. No cerium species were detected by EDS. In future work more surface sensitive techniques like Auger or XPS should be used in order to verify this.

3. The combination of ethylene glycol and $Ce(SO_4)_2$ did not show any difference on the SAA substrate but did show a tremendous drop in corrosion performance on the TSA substrates. The presence of the relatively large ethylene glycol molecules probably prohibits the formation of the negatively charged complexes between cerium and tartaric acid compounds. This results in less cerium species being attracted to the substrate and therefore less cerium ending up in the pores, which causes the drop in corrosion performance. The presence and absence of these negatively charged complexes in solution should be investigated in the future.

References

[1]   WorldAtlas, The most abundant elements in the earth's crust, (2018). https://www.worldatlas.com/articles/the-most-abundant-elements-in-the-earth-s-crust.html (accessed October 15, 2019).

[2]   I. Polmear, D. StJohn, J.F. Nie, M. Qian, Light Alloys: Metallurgy of the Light Metals, 5th ed., Butterworth-Heinemann, Oxford, 2017. doi:10.1016/B978-0-08-099431-4.00001-4.

[3]   N.L. Sukiman, X. Zhou, N. Birbilis, J.M.C. Mol, S.J. Garcia, G.E. Thompson, Durability and Corrosion of Aluminium and Its Alloys: Overview, Property Space, Techniques and Developments, in: Z. Ahmad (Ed.), Alum. Alloy. - New Trends Fabr. Appl., IntechOpen, London, 2013: pp. 47–98. doi:10.5772/53752.

[4]   A.P. Mouritz, Introduction to Aerospace Materials, 1st ed., Woodhead Publishing, Sawston, 2012.

[5]   E. Bardal, Corrosion and Protection, 1st ed., Springer-Verlag, London, 2004.

[6]   A.E. Hughes, J.M.C. Mol, M.L. Zheludkevich, R.G. Buchheit, Introduction, in: A.E. Hughes, J.M.C. Mol, M.L. Zheludkevich, R.G. Buchheit (Eds.), Act. Prot. Coatings New-Generation Coatings Met., 1st ed., Springer Science+Business Media, Dordrecht, 2016: pp. 1–13. doi:10.1007/978-94-017-7540-3.

[7]   P. Visser, H. Terryn, J.M.C. Mol, Aerospace Coatings, in: A.E. Hughes, J.M.C. Mol, M.L. Zheludkevich, R.G. Buchheit (Eds.), Act. Prot. Coatings New-Generation Coatings Met., 1st ed., Springer Science+Business Media, Dordrecht, 2016: pp. 315–372. doi:10.1007/978-94-017-7540-3.

[8]   O. Gharbi, S. Thomas, C. Smith, N. Birbilis, Chromate replacement: what does the future hold?, Npj Mater. Degrad. 2 (2018) 23–25. doi:10.1038/s41529-018-0034-5.

[9]   ECHA, Registration, Evaluation, Authorisation and Restriction of Chemicals (REACH), (2019). https://echa.europa.eu/regulations/reach/understanding-reach (accessed October 17, 2019).

[10]   S.T. Abrahami, Cr(VI)-free pre-treatments for adhesive bonding of aerospace aluminium alloys, PhD diss., Delft University of Technology, 2016.

[11]   B. Wielage, G. Alisch, T. Lampke, D. Nickel, Anodizing – A Key for Surface Treatment of Aluminium, Key Eng. Mater. 384 (2008) 263–281. doi:10.4028/www.scientific.net/kem.384.263.

[12]   W. Chen, J.S. Wu, X.H. Xia, Porous anodic alumina with continuously manipulated pore/cell size, ACS Nano. 2 (2008) 959–965. doi:10.1021/nn700389j.

[13]   C.S. Mali, S.D. Chavan, K.S. Kanse, A.C. Kumbharkhane, S.C. Mehrotra, Dielectric relaxation of poly ethylene glycol-water mixtures using time domain technique, Indian J. Pure Appl. Phys. 45 (2007) 476–481.

[14]   W.J. Stępniowski, D. Forbot, M. Norek, M. Michalska-Domańska, A. Król, The impact of viscosity of the electrolyte on the formation of nanoporous anodic aluminum oxide, Electrochim. Acta. 133 (2014) 57–64. doi:10.1016/j.electacta.2014.04.039.

[15]   M. Michalska-Domańska, W.J. Stępniowski, M. Salerno, Effect of inter-electrode separation in the fabrication of nanoporous alumina by anodization, J. Electroanal. Chem. 823 (2018) 47–53. doi:10.1016/j.jelechem.2018.05.038.

[16]   C. Dumitriu, C. Pirvu, I. Demetrescu, The electrochemical formation and shielding mechanism of TiO2 nanotubes in organic electrolytes with different viscosity, J. Electrochem. Soc. 160 (2013) 55–60. doi:10.1149/2.035302jes.

[17]   M. Curioni, P. Skeldon, G.E. Thompson, Anodized anti-corrosion coatings for aluminium using rare earth metals, in: M. Forsyth, B. Hinton (Eds.), Rare Earth-Based Corros. Inhib., 1st ed., Elsevier, Amsterdam, 2015: pp. 143–162. doi:10.1533/9780857093585.143.

[18]   V. Moutarlier, M.P. Gigandet, J. Pagetti, B. Normand, An electrochemical approach to the anodic oxidation of Al 2024 alloy in sulfuric acid containing inhibitors, Surf. Coatings Technol. 161 (2002) 267–274. doi:10.1016/S0257-8972(02)00414-0.

[19]   M. Saeedikhani, M. Javidi, S. Vafakhah, Anodising of 2024-T3 aluminium alloy in electrolyte of sulphuric– boric–phosphoric mixed acid containing cerium salt as corrosion inhibitor, Trans. Nonferrous Met. Soc. China (English Ed. 27 (2017) 711–721. doi:10.1016/S1003-

6326(17)60079-7.

[20]   M. Curioni, A.A. Zuleta, E. Correa, X. Pan, A. Baron-Wiechec, P. Skeldon, J.G. Castaño, F. Echeverría, G.E. Thompson, Formation of protective anodic oxides on aluminium by low voltage anodising in sulphuric acid with cerium nitrate and tartaric acid additions, Trans. IMF. 90 (2012) 290–297. doi:10.1179/0020296712Z.00000000059.

[21]   J.G. Kaufman, Introduction to Aluminum Alloys and Tempers, 1st ed., ASM International, Materials Park, Ohio, 2000.

[22]   The-Aluminum-Association, International Alloy Designations and Chemical Composition Limits for Wrought Aluminum and Wrought Aluminum Alloys, 2015.

[23]   J. Li, N. Birbilis, R.G. Buchheit, Electrochemical assessment of interfacial characteristics of intermetallic phases present in aluminium alloy 2024-T3, Corros. Sci. 101 (2015) 155–164. doi:10.1016/j.corsci.2015.09.012.

[24]   A.E. Hughes, R. Parvizi, M. Forsyth, Microstructure and corrosion of AA2024, Corros. Rev. 33 (2015) 1–30. doi:10.1515/corrrev-2014-0039.

[25]   T. Hashimoto, X. Zhang, X. Zhou, P. Skeldon, S.J. Haigh, G.E. Thompson, Investigation of dealloying of S phase (Al2CuMg) in AA 2024-T3 aluminium alloy using high resolution 2D and 3D electron imaging, Corros. Sci. 103 (2016) 157–164. doi:10.1016/j.corsci.2015.11.013.

[26]   X. Zhang, T. Hashimoto, J. Lindsay, X. Zhou, Investigation of the de-alloying behaviour of θ-phase (Al2Cu) in AA2024-T351 aluminium alloy, Corros. Sci. 108 (2016) 85–93. doi:10.1016/j.corsci.2016.03.003.

[27]   J. Evertsson, F. Bertram, F. Zhang, L. Rullik, L.R. Merte, M. Shipilin, M. Soldemo, S. Ahmadi, N. Vinogradov, F. Carlà, J. Weissenrieder, M. Göthelid, J. Pan, A. Mikkelsen, J.O. Nilsson, E. Lundgren, The thickness of native oxides on aluminum alloys and single crystals, Appl. Surf. Sci. 349 (2015) 826–832. doi:10.1016/j.apsusc.2015.05.043.

[28]   E. McCafferty, Introduction to Corrosion Science, 1st ed., Springer Science+Business Media, New York, 2010.

[29]   R.G. Compton, C.E. Banks, Understanding Voltammetry, 3rd ed., World Scientific, Singapore, 2018. doi:10.1142/q0155.

[30]   M. Cerit, Corrosion pit-induced stress concentration in spherical pressure vessel, Thin-Walled Struct. 136 (2019) 106–112. doi:10.1016/j.tws.2018.12.014.

[31]   J.M.C. Mol, Filiform Corrosion of Aluminium Alloys, PhD diss., Delft University of Technology, 2000.

[32]   L. Yang, Introduction, in: L. Yang (Ed.), Tech. Corros. Monit., 1st ed., Woodhead Publishing, Sawston, 2008: pp. 1–5. doi:10.1533/9781845694050.1.

[33]   A.J. Bard, L.R. Faulkner, Electrochemical Methods Fundamentals and Applications, 2nd ed., John Wiley & Sons, New York, 2001.

[34]   S. Papavinasam, Electrochemical polarization techniques for corrosion monitoring, in: L. Yang (Ed.), Tech. Corros. Monit., 1st ed., Woodhead Publishing, Sawston, 2008: pp. 49–85. doi:10.1533/9781845694050.1.49.

[35]   R.K. Franklin, In vivo Electrochemical Sensors, PhD diss., University of Michigan, 2010.

[36]   R. Kelly, J.R. Scully, D. Shoesmith, R.G. Buchheit, Electrochemical Techniques in Corrosion Science and Engineering, 1st ed., CRC Press, Boca Raton, 2002. doi:10.1201/9780203909133.

[37]   G.S. Frankel, Fundamentals of Corrosion Kinetics, in: A.E. Hughes, J.M.C. Mol, M.L. Zheludkevich, R.G. Buchheit (Eds.), Act. Prot. Coatings New-Generation Coatings Met., 1st ed., Springer Science+Business Media, Dordrecht, 2016: pp. 17–32. doi:10.1007/978-94-017-7540-3.

[38]   Y. Tan, Heterogeneous Electrode Processes and Localized Corrosion, 1st ed., John Wiley & Sons, Hoboken, New Jersey, 2013. doi:10.1002/9781118466360.

[39]   A. Lasia, Electrochemical Impedance Spectroscopy and its Applications, 1st ed., Springer Science+Business Media, New York, 2014. doi:10.1007/978-1-4614-8933-7.

[40]   BYU, Physics 145: Lab 6 AC-Circuit Theory and Complex Numbers, (2011). https://www.physics.byu.edu/faculty/peatross/homework/complex145.pdf (accessed November 26, 2019).

[41]   M.L. Zheludkevich, K.A. Yasakau, A.C. Bastos, O. V. Karavai, M.G.S. Ferreira, On the application of electrochemical impedance spectroscopy to study the self-healing properties

of protective coatings, Electrochem. Commun. 9 (2007) 2622–2628. doi:10.1016/j.elecom.2007.08.012.

[42]   Y. Wu, W. Zhao, W. Wang, L. Wang, Q. Xue, Novel anodic oxide film with self-sealing layer showing excellent corrosion resistance, Sci. Rep. 7 (2017) 1–9. doi:10.1038/s41598-017-01549-y.

[43]   V.P. Parkhutik, V.I. Shershulsky, Theoretical modelling of porous oxide growth on aluminium, J. Phys. D. Appl. Phys. 25 (1992) 1258–1263. doi:10.1088/0022-3727/25/8/017.

[44]   W.J. Stępniowski, M. Norek, M. Michalska-Domańska, A. Bombalska, A. Nowak-Stępniowska, M. Kwaśny, Z. Bojar, Fabrication of anodic aluminum oxide with incorporated chromate ions, Appl. Surf. Sci. 259 (2012) 324–330. doi:10.1016/j.apsusc.2012.07.043.

[45]   W.J. Stępniowski, W. Florkiewicz, M. Norek, M. Michalska-Domańska, E. Kościuczyk, T. Czujko, Various Modifications of Electrochemical Barrier Layer Thinning of Anodic Aluminum Oxide, Int. J. Mater. Metall. Eng. 8 (2014) 1488–1491.

[46]   F. Li, L. Zhang, R.M. Metzger, On the Growth of Highly Ordered Pores in Anodized Aluminum Oxide, Chem. Mater. 10 (1998) 2470–2480. doi:10.1021/cm980163a.

[47]   L. Zaraska, G.D. Sulka, M. Jaskua, Properties of nanostructures obtained by anodization of aluminum in phosphoric acid at moderate potentials, J. Phys. Conf. Ser. 146 (2009). doi:10.1088/1742-6596/146/1/012020.

[48]   S. Yoriya, Effect of Inter-Electrode Spacing on Electrolyte Properties and Morphologies of Anodic TiO2 Nanotube Array Films, Int. J. Electrochem. Sci. 7 (2012) 9454–9464.

[49]   C.G. Dariva, A.F. Galio, Corrosion Inhibitors – Principles, Mechanisms and Applications, in: M. Aliofkhazraei (Ed.), Dev. Corros. Prot., 1st ed., IntechOpen, London, 2014: pp. 365–380. doi:10.5772/57255.

[50]   M. Kendig, S. Jeanjaquet, R. Addison, J. Waldrop, Role of hexavalent chromium in the inhibition of corrosion of aluminum alloys, Surf. Coatings Technol. 140 (2001) 58–66. doi:10.1016/S0257-8972(01)01099-4.

[51]   F. Brito, J. Ascanio, S. Mateo, C. Hernández, L. Araujo, P. Gili, P. Martín-Zarza, S. Domínguez, A. Mederos, Equilibria of chromate(VI) species in acid medium and ab initio studies of these species, Polyhedron. 16 (1997) 3835–3846. doi:10.1016/S0277-5387(97)00128-9.

[52]   V. Moutarlier, M.P. Gigandet, B. Normand, J. Pagetti, EIS characterisation of anodic films formed on 2024 aluminium alloy, in sulphuric acid containing molybdate or permanganate species, Corros. Sci. 47 (2005) 937–951. doi:10.1016/j.corsci.2004.06.019.

[53]   D. Li, Y.P. Deng, B.L. Guo, G.Q. Li, Investigation of Cerium Salt/Sulfuric Acid Anodizing Technology for 1420 Aluminum Alloy, Mater. Sci. Forum. 331–337 (2000) 1695–1700. doi:10.4028/www.scientific.net/msf.331-337.1695.

[54]   D.C. Harris, Quantitative Chemical Analysis, 8th ed., W. H. Freeman and Company, New York, 2010.

[55]   A.J.J. Aldykewicz, H.S. Isaacs, A.J. Davenport, The Investigation of Cerium as a Cathodic Inhibitor for Aluminum-Copper Alloys, J. Electrochem. Soc. 142 (1995) 3342–3350. doi:10.1149/1.2049985.

[56]   S.T. Abrahami, J.M.M. de Kok, H. Terryn, J.M.C. Mol, Towards Cr (VI) -free anodization of aluminum alloys for aerospace adhesive bonding applications : A review, Front. Chem. Sci. Eng. 11 (2017) 465–482. doi:10.1007/s11705-017-1641-3.

[57]   S. Wang, F. Yang, G.S. Frankel, Effect of Altered Surface Layer on Localized Corrosion of Aluminum Alloy 2024, J. Electrochem. Soc. 164 (2017) C317–C323. doi:10.1149/2.1541706jes.

[58]   G.M. Scamans, M.F. Frolish, W.M. Rainforth, Z. Zhou, Y. Liu, X. Zhou, G.E. Thompson, The ubiquitous Beilby layer on aluminium surfaces, Surf. Interface Anal. 42 (2010) 175–179. doi:10.1002/sia.3204.

[59]   U. Tiringer, J. Kovač, I. Milošev, Effects of mechanical and chemical pre-treatments on the morphology and composition of surfaces of aluminium alloys 7075-T6 and 2024-T3, Corros. Sci. 119 (2017) 46–59. doi:10.1016/j.corsci.2017.02.018.

[60]   A. Afseth, J.H. Nordlien, G.M. Scamans, K. Nisancioglu, Effect of heat treatment on filiform corrosion of aluminium alloy AA3005, Corros. Sci. 43 (2001) 2093–2109.

[61]   A. Afseth, J.H. Nordlien, G.M. Scamans, K. Nisancioglu, Influence of heat treatment and surface conditioning on filiform corrosion of aluminium alloys AA3005 and AA5754, Corros.

Sci. 43 (2001) 2359–2377.

[62] Y. Ma, X. Zhou, G.E. Thompson, P. Skeldon, Surface texture formed on AA2099 Al – Li – Cu alloy during alkaline etching, Corros. Sci. 66 (2013) 292–299. doi:10.1016/j.corsci.2012.09.032.

[63] I.M. Stewart, Surface Characterization by Ion Microprobe Analyzer, in: L. Lee (Ed.), Charact. Met. Polym. Surfaces, Vol. 1 Met. Surfaces, 1st ed., Academic Press, Cambridge, Massachusetts, 1977: pp. 541–559. doi:10.1016/B978-0-12-442101-1.X5001-8.

[64] D. Elabar, A. Němcová, T. Hashimoto, P. Skeldon, G.E. Thompson, Effect of sulphate impurity in chromic acid anodizing of aluminium, Corros. Sci. 100 (2015) 377–385. doi:10.1016/j.corsci.2015.08.019.

[65] W.J. Stępniowski, M. Michalska-Domańska, M. Norek, T. Czujko, Fast Fourier transform based arrangement analysis of poorly organized alumina nanopores formed via self-organized anodization in chromic acid, Mater. Lett. 117 (2014) 69–73. doi:10.1016/j.matlet.2013.11.099.

[66] H. Miyazaki, H. Uozaki, A. Tojo, S. Hirashima, S. Inaga, K. Sakuma, Y. Morishita, M. Fukayama, Application of low-vacuum scanning electron microscopy for renal biopsy specimens, Pathol. Res. Pract. 208 (2012) 503–509. doi:10.1016/j.prp.2012.05.006.

[67] M. Meeusen, P. Visser, L. Fernández Macía, A. Hubin, H. Terryn, J.M.C. Mol, The use of odd random phase electrochemical impedance spectroscopy to study lithium-based corrosion inhibition by active protective coatings, Electrochim. Acta. 278 (2018) 363–373. doi:10.1016/j.electacta.2018.05.036.

[68] T. Breugelmans, J. Lataire, T. Muselle, E. Tourwé, R. Pintelon, A. Hubin, Odd random phase multisine electrochemical impedance spectroscopy to quantify a non-stationary behaviour: Theory and validation by calculating an instantaneous impedance value, Electrochim. Acta. 76 (2012) 375–382. doi:10.1016/j.electacta.2012.05.051.

[69] H.S. Isaacs, C. Scheffey, R. Huang, The location of events producing potential transients during pitting of freely corroding Al and its alloys, ECS Trans. 11 (2008) 1–12. doi:10.1149/1.2925257.

[70] A. Kumar Singh, S. Ghosh, S. Mula, Simultaneous improvement of strength, ductility and corrosion resistance of Al2024 alloy processed by cryoforging followed by ageing, Mater. Sci. Eng. A. 651 (2016) 774–785. doi:10.1016/j.msea.2015.11.032.

[71] G.O. Ilevbare, O. Schneider, R.G. Kelly, J.R. Scully, In situ confocal laser scanning microscopy of AA 2024-T3 corrosion metrology I. Localized corrosion of particles, J. Electrochem. Soc. 151 (2004) 453–464. doi:10.1149/1.1764780.

[72] F.M.A. Sroor, F.T. Edelmann, Tetravalent Chemistry : Inorganic, in: R.A. Scott (Ed.), Encycl. Inorg. Bioinorg. Chem., 1st ed., John Wiley & Sons, Hoboken, New Jersey, 2012: pp. 1–8. doi:10.1002/9781119951438.eibc2033.

[73] N. Datt, R.R. Nagori, R.N. Mehrotra, Kinetics and mechanisms of oxidations by metal ions. Part VI. Oxidation of a-hydroxy acids by cerium(IV) in aqueous nitric acid, Can. J. Chem. 64 (1986) 19–23.

[74] T.K.M. Shing, Glycol Cleavage Reactions, in: B.M. Trost, I. Fleming (Eds.), Compr. Org. Synth., 1st ed., Pergamon Press, Oxford, 1991: pp. 703–715. doi:10.1016/b978-0-08-052349-1.00209-2.

[75] J.K. Szymański, F. Temprano-Coleto, J. Pérez-Mercader, Unusual kinetics of poly(ethylene glycol) oxidation with cerium(IV) ions in sulfuric acid medium and implications for copolymer synthesis, Phys. Chem. Chem. Phys. 17 (2015) 6713–6717. doi:10.1039/c4cp05693k.

[76] P. Chilimoniuk, M. Michalska-Domańska, W.J. Stępniowski, T. Czujko, Formation of nanoporous oxide by self-organized anodizing of FeAl intermetallic alloy in oxalic acid solution containing glycol, Mater. Lett. 224 (2018) 9–12. doi:10.1016/j.matlet.2018.04.035.

[77] M. Michalska-Domańska, W.J. Stępniowski, L.R. Jaroszewicz, Characterization of nanopores arrangement of anodic alumina layers synthesized on low-(AA1050) and high-purity aluminum by two-step anodizing in sulfuric acid with addition of ethylene glycol at low temperature, J. Porous Mater. 24 (2017) 779–786. doi:10.1007/s10934-016-0316-7.

[78] R.M.C. Dawson, D.C. Elliott, W.H. Elliott, K.M. Jones, Data for Biochemical Research, 1st ed., Oxford University Press, Oxford, 1959.

[79] T.P. Hoar, J. Yahalom, The Initiation of Pores in Anodic Oxide Films Formed on Aluminum in Acid Solutions, J. Electrochem. Soc. 110 (1963) 614–621. doi:10.1149/1.2425839.

72

[80] G.D. Sulka, Highly Ordered Anodic Porous Alumina Formation by Self-Organized Anodizing, in: A. Eftekhari (Ed.), Nanostructured Mater. Electrochem., 1st ed., Wiley-VCH, Weinheim, 2008: pp. 1–116. doi:10.1002/9783527621507.ch1.

[81] L. Sun, S. Zhang, X.W. Sun, X. He, Effect of electric field strength on the length of anodized titania nanotube arrays, J. Electroanal. Chem. 637 (2009) 6–12. doi:10.1016/j.jelechem.2009.09.023.

[82] X. Zhao, Y. Zuo, J. Zhao, J. Xiong, Y. Tang, A study on the self-sealing process of anodic films on aluminum by EIS, Surf. Coatings Technol. 200 (2006) 6846–6853. doi:10.1016/j.surfcoat.2005.10.031.

[83] M. Michalska-Domańska, M. Norek, W.J. Stępniowski, B. Budner, Fabrication of high quality anodic aluminum oxide (AAO) on low purity aluminum - A comparative study with the AAO produced on high purity aluminum, Electrochim. Acta. 105 (2013) 424–432. doi:10.1016/j.electacta.2013.04.160.

[84] W.J. Stępniowski, M. Norek, M. Michalska-Domańska, A. Nowak-Stępniowska, A. Bombalska, M. Włodarski, Z. Bojar, Incorporation of copper chelate ions into anodic alumina walls, Mater. Lett. 106 (2013) 242–245. doi:10.1016/j.matlet.2013.05.016.